# Episodic crustal extension and contraction characterizing the Late Mesozoic tectonics of East China: Evidence from the Jiaodong Peninsula, East China

**Lingtong Meng[1,2], Wei Lin[1,2*]**

[1]State Key Laboratory of Lithospheric Evolution, Institute of Geology and Geophysics, Innovation Academy of Earth Science, Chinese Academy of Sciences, Beijing 100029, China

[2]College of Earth and Planetary Sciences, University of Chinese Academy of Sciences, Beijing 100049, China

*corresponding author: Wei Lin (linwei@mail.iggcas.ac.cn)

**Key points：**

- Polyphase deformation and multi-stage pluton emplacement were recognized in the Jiaodong Peninsula
- East China experienced a complex tectonic evolution marked by Late Mesozoic episodic intracontinental extension-contraction
- A multidisciplinary study improves our understanding on the intracontinental deformation under multi-plate convergent system

## Abstract

During the Late Mesozoic, East China is characterized by a widespread magmatism, thrusting and folding, extensional doming, strike-slip faulting, and block rotation. The Jiaodong Peninsula provides a key area located in East China to understand the episodic intracontinental extension and contraction, and associated granitoids emplacement. Based on our structural analysis, magnetic fabrics and gravity modeling, polyphase deformation and magma emplacement have been recognized within the

Queshan-Kunyushan-Yuangezhuang-Sanfoshan (QKYS) massif of the central Jiaodong Peninsula. A significant Late Jurassic $D_1$ event, developed in the northern margin of the massif, was expressed by a high-temperature, top-to-the-NE shearing. Late Jurassic plutons display magnetic fabrics corresponding to the $D_1$ structural fabrics and several NW–SE-trending feeder zones at depth. These results link the syn-kinematic emplacement of Late Jurassic plutons with regional NE–SW extensional tectonics. At the south of the massif, a lower-temperature, top-to-the-SW contractional deformation ($D_2$) resulted from NE–SW contraction. The $D_3$ shear zone with a top-to-the-WNW kinematics is a rolling-hinge type detachment fault that exhumed the massif, indicating NW–SE regional extension. Finally, Early Cretaceous plutons emplaced into upper crust with a fast cooling rate and formed an inverted drop shape with concentric magnetic foliations and variably oriented magnetic lineations. At the light of the previous geochronological results, the timing of these tectonic events are discussed. The tectonic evolution of the QKYS massif indicates a process from crustal thickening to lithospheric foundering in response to the Late Mesozoic plate convergences.

**Keywords**

Intracontinental deformation, Granitic pluton structural analyses, Anisotropy of magnetic susceptibility, Gravity modeling, East China geodynamics.

## 1 Introduction

In typical collisional or accretionary orogens, deformation mainly takes place at plate boundaries and adjacent regions, since the continent interior is considered rigid (Coward *et al*., 1987). However, intensive deformation could develop inside the continent, even though it is far away from plate boundaries (*e.g*., Dickinson & Snyder, 1978; Roure *et al*., 1989; Avouac *et al*., 1993; Chu *et al*., 2012, Chu & Lin, 2018). East China was formed by continental collision between North China Craton (NCC) and South China Block (SCB) at the Early Mesozoic (Mattauer *et al*., 1985; Xu *et al*., 1992; Cong *et al*., 1995; Hacker *et al*., 1998; Faure *et al*., 1999). During the Late Mesozoic, East China is surrounded by multi-plate convergent zones, including Mongol-Okhotsk belt to its north, the subduction zone related to Izanagi Plate to its east and the collisional zone between Lhasa and Qiangtang blocks to its west (Figure 1). At this time, East China is characterized by a widespread magmatism, large-scale thrusting and folding, extensional doming, strike-slip faulting, graben and half-graben basins, and rigid blocks rotation (Lin *et al*., 2003; Otofuji *et al*., 2006; Dong *et al*., 2015 and references therein). It offers a key area to understand the mechanism of episodic intracontinental extension and contraction, and associated magmatism under the multi-plate convergences.

Previous studies that focused on the Jurassic–Cretaceous tectonic evolution of East China have suggested (1) two significant episodes of contractional tectonics during Middle or Late Jurassic–Earliest Cretaceous (Wong, 1929; Chen, 1998; Davis *et al*., 2001; Darby & Ritts, 2002; Davis *et al*., 2009; Faure *et al*., 2012); (2) subsequent Early Cretaceous extensional tectonics, characterized by numerous extensional basins, metamorphic core complexes (MCC) and syn-kinematic plutons (Davis *et al*., 2002; Ren *et al*., 2002; Meng, 2003; Wang *et al*., 2012; Liu *et al*., 2013; Lin & Wei, 2018; Chu *et al*., 2019); and (3) long-term magmatism from 170 to 110 Ma with Late Jurassic (170–150 Ma) and Early Cretaceous (135–110 Ma) magmatic flare-ups (Wu *et al*., 2019). These events have been considered differently by various geologists based on regional unconformities, polyphase deformation, and

magmatism, leading to a broad Late Mesozoic tectonic framework of East China. Especially for Late Jurassic–Earliest Cretaceous tectonics, its timing and kinematics remain hotly debated, and the interplay between structure and magmatism is still poorly constrained (Dong *et al*., 2015 and references therein). More importantly, Early Cretaceous crustal extension results from the "craton destruction"; lithospheric foundering/delamination or thermal erosion were suggested to be potential mechanism, in which old and refractory lithospheric mantle is replaced by juvenile and fertile one (Menzies *et al*., 1993; Xu, 2001; Lin & Wang, 2006; Zhu *et al*., 2011; Lin & Wei, 2018; Wu *et al*., 2019; among others). Hence, the Late Mesozoic tectonic evolution helped to understand the mechanism of "craton destruction".

In general, granitoids emplacement is controlled by internal dynamics and external tectonism (Bouchez, 1997; Miller *et al*., 2009; Žák *et al*., 2013, Lehmann *et al*., 2013; Paterson *et al*., 2019, among others), and their subsequent exhumation is commonly related to regional ductile shear zones (Bouchez *et al*., 1990; Archanjo *et al*., 2002; Rabillard *et al*., 2015; Wei *et al*., 2016; Chu *et al*., 2019, among others). Hence, the emplacement-exhumation history of granitoids contains significant information on tectonic evolution (*e.g.*, Lin *et al*., 2013a, Ji *et al*., 2018a). This history also can be revealed by fabric patterns, shapes at depth, and kinematics of major ductile shear zones at the margins of plutons, which are accessible through structural analyses, anisotropy of magnetic susceptibility (AMS) and gravity surveys.

The easternmost part of East China (*i.e.*, Jiaodong Peninsula) is a key area to understand the complex plutonic-tectonic history, because it developed an intensive magmatism, contractional and extensional events, and large-scale gold mineralization during the Late Mesozoic (Li *et al.*, 2019). In this paper, the Queshan-Kunyushan-Yuangezhuang-Sanfoshan (QKYS) massif, located in the central part of the Jiaodong Peninsula (Figure 1), was targeted for the following reasons. Firstly, it comprises Late Jurassic and Early Cretaceous granitic intrusions within their metamorphic country rocks, which experienced a polyphase deformation. Secondly, Late Jurassic and Early Cretaceous plutons were

emplaced into middle crustal and upper crustal levels, respectively (Dou *et al*., 2018). Lastly, the crystallization and cooling ages of this massif are already well-defined. Accordingly, we carried out a multidisciplinary study containing structural analyses, AMS and gravity surveys on it, aiming to depict its multiple emplacement and exhumation, the relationship between magmatism and regional tectonics, and finally the Late Mesozoic tectonic evolution and geodynamics of East China.

## 2 Geological setting of the Jiaodong Peninsula

Jiaodong Peninsula, bounded by the Tan-Lu fault to its west, is situated in the easternmost part of East China (Figure 1). It can be divided into three tectonic units: Jiaobei domain in its northwestern to central part, Northern Sulu domain in its eastern part and Early Cretaceous Jiaolai Basin containing volcanic and clastic rocks to the southwest (Figure 1).

The Jiaobei domain contains three metamorphic units. From bottom to top: (1) Neoarchean to Paleoproterozoic meta-granite, gneissic migmatite, granulite with meta-mafic or amphibolite lenses; (2) Paleoproterozoic meta-sedimentary rocks including micaschist, paragneiss, marble and amphibolite; (3) Neoproterozoic weakly to un-metamorphosed terrigenous rocks (Hacker *et al*., 2006; Wan *et al*., 2006; Li *et al*., 2007). Geochronological works reveal that these rocks have Neoarchean-Paleoproterozoic protolith ages with peaks at 2.9, 2.7 and 2.5 Ga and experienced a 1.8 Ga amphibolite-facies metamorphism, belonging to the NCC (Zhao *et al*., 1998; Zhai *et al*., 2000, 2005; Zhang *et al*., 2014).

The Northern Sulu domain mainly consists of migmatite, gneiss, quartzite, marble, and decimeter-sized mafic to ultramafic blocks (Figure 1). They display a protolith age of 0.75 Ga and Late Triassic metamorphic ages, suggesting a SCB affinity (Liu & Liou, 2011). Eclogites are enclosed as blocks within these rocks. In particular, the discovery of coesite as inclusions within the melanosome of migmatite and orthogneiss implies that they experienced an ultra-high pressure (UHP) metamorphism during the Late Triassic (Wang *et al*., 1993; Wallis *et al*., 1997). It is well accepted that the UHP rocks

formed by the deep subduction of the SCB beneath the NCC; the retrograde metamorphism and migmatization are associated with a Late Triassic extensional tectonics (Faure *et al*., 2001, 2003).

Widespread Mesozoic intrusive rocks are exposed in the Jiaodong Peninsula. These intrusions can be divided into four groups according to their ages: (1) Late Triassic syenite; (2) Late Jurassic monzogranite; (3) Early Cretaceous porphyritic granitoid; and (4) Early to Late Cretaceous mafic-intermediate dykes (Guo *et al*., 2005). The Late Jurassic plutons are derived from partial melting of a thickened lower crust, while the Cretaceous plutons and dykes resulted from lithospheric mantle removal, accompanied by asthenospheric upwelling (Yang *et al*., 2008; Goss *et al*., 2010; Zhang *et al*., 2010). It should be noted that the significant Late Mesozoic deformations are mainly distributed at the margins of these Late Mesozoic plutons (Figure 1; Shen *et al*., 1998; Charles *et al*., 2011a; Xia *et al*., 2016)

## 3 Structural analysis of the QKYS massif

### 3.1 Litho-tectonic units of the QKYS massif

As a part of the Jiaobei domain, the QKYS massif is composed of Late Mesozoic plutons, which mainly trend NNE–SSW, and their country rocks (Figures 2 and 3). Western margin of the QKYS massif is a ductile shear zone that separates the massif from Early Cretaceous volcanic and clastic rocks. Taocun and Mishan faults are considered as its northwestern and eastern boundaries, respectively (Figure 2). To its north and south, the massif is covered by Cenozoic fluvial and lacustrine deposits. The QKYS massif can be divided into four litho-tectonic units: (1) Neoarchean to Paleoproterozoic meta-granite, gneissic migmatite, granulite with meta-mafic or amphibolite lenses; (2) Paleoproterozoic meta-sedimentary rocks including micaschist, paragneiss, marble and amphibolite; (3) Late Jurassic Queshan (Q) and Kunyushan (K) plutons composed of medium- to coarse-grained biotite monzogranite; and (4) Early Cretaceous Sanfoshan (S) and Yuangezhuang (Y) porphyritic granite.

The country rocks of these granites include 2.6–2.5 Ga meta-mafic rocks, 2.7–2.4 Ga meta-granites, and metamorphic sedimentary rocks that are considered as deposited at 2.1–1.9 Ga (Liu *et al*., 2017a). Zircons of K and Q plutons have inherited cores (*e.g.*, Guo *et al*., 2005; Zhao *et al*., 2016) and were affected by later thermal event (*e.g.*, Xia *et al*., 2016), resulting in a broad range of ages (163–141 Ma, Figure 4A) for these two plutons. Therefore, we use statistical peak age (153 Ma) as their crystallization ages (Figure 4B). Most parts of the massif have Early Cretaceous $^{40}Ar/^{39}Ar$ ages (*i.e.*, 135–120 Ma), and the older ones (*i.e.*, 219–146 Ma) are present in its southern part (Figure 4C). For the S and Y plutons, they have indistinguishable zircon U-Pb and biotite $^{40}Ar/^{39}Ar$ ages ranging from 118 to 113 Ma (Figure 4C and D).

### 3.2 Bulk architecture and kinematic analyses of the QKYS massif

In the QKYS massif, K pluton has an elliptical shape with a NNE–SSW long axis, and irregular-shaped Q pluton is separated into two parts due to late sinistral strike-slip movement of Zhuwu fault (Figure 2). Well-foliated to mylonitic gneiss, schists, marble, and amphibolite are exposed as their country rocks. The K pluton is dominated by isotropic monzogranite in its central part, while clear foliation is present on its NE margin, which is composed of recrystallized quartz aggregates and feldspar (Figure 5A and B). In the western part of the Q pluton, conspicuous mylonitic foliations are well developed. The gently dipping post-solidus foliation is defined by recrystallized quartz grains, rotated K-feldspars, and oriented biotite (Figure 5C). A homogeneous monzogranite type composed of K-feldspar, quartz, plagioclase, and biotite is dominant in the eastern part of Q pluton. The S pluton with a NE–SW long axis intruded into the K pluton and the UHP gneiss, while the Y pluton emplaced along the northern margin of Q pluton (Figure 2). Both S and Y plutons are isotropic (Figure 5D).

Based on our structural analysis, the bulk architecture of the QKYS massif is dominated by a Late Mesozoic dome that experienced ductile deformation at its northern, southern, and western

margins (Figures 2, 3 and 6). The foliations of orthogneiss and gneissic migmatite between Q and K plutons mainly dip to SE, NW or NE at variable dip angles and contain NW–SE mineral and stretching lineations (Figure 6A).

Along the northern margin of K pluton, a solid-state foliation develops, up to a few hundred meters inside the pluton, pointing to the existence of a deformation event. Following the contact between the granite and the country rocks, the granite foliation dips to the N, NE, or NNW with moderate to low dip angles, and changes to E(S)E dips in its eastern part, with a locally NE–SW sub-horizontal mineral lineation (Figures 6B and 7A). Close to the northern margin of K pluton, the orthogneiss shows dominantly NW–SE striking foliations that are parallel to the granite/orthogneiss contact (Figure 6C). Isoclinal folds with axes parallel to the NE–SW mineral and stretching lineation developed in the orthogneiss (Figure 7B). Along the NE–SW linear structures, a top-to-the-NE sense of shear is revealed by sigmoidal feldspar porphyroclasts within the orthogneiss and foliated granite, either in the field or thin sections (Figure 7C–F).

At the south of the massif, foliations are well-developed in the Neoarchean to Paleoproterozoic metamorphosed rocks, mainly dipping to the SW, SSE, or SE with moderate to low angles (Figure 6D). The NE-SW linear structures, mostly at 65°/10°, are indicated by semi-penetrative mineral and stretching lineations and the axes of isoclinal folds (Figures 6D, 8A and 8B). The mineral and stretching lineation is defined by preferred orientation of biotite, K-feldspars and quartz aggregates (Figure 8A). Along this NE–SW-trending lineation, a top-to-the-SW sense of shear is documented by asymmetric lensed feldspar in the micaschist (Figure 8C), sigmoidal feldspar porphyroclasts in the mylonites (Figure 8D), and other sigmoidal features as observed under the microscope (feldspar porphyroclasts: Figure 8E, and mica fishes: Figure 8F).

Along the western boundary of the massif, decameter- to hectometer-thick ductile shear zone is displaced by brittle sinistral Zhuwu fault, sealed by Early Cretaceous non-foliated Haiyang pluton to its

south, and covered by late stage of Early Cretaceous clastic rocks to its north (Figure 2). Brittle normal faults overprinting the ductile shear zone represent the eastern boundary of the half-graben basin filled with Early Cretaceous volcanic and clastic rocks (Figure 3). Mylonites in the Q pluton and its country rocks exhibit a pervasive foliation parallel to the western margin of the massif approximately. The mylonitic foliation gently dips to the NW, WNW, or SW at moderate to low angles (5°–40°), and changes to SE or NE dips away from the western margin (Figures 2 and 6E). Whatever the dip direction of the foliation, a conspicuous mineral and stretching lineation with a dominant WNW–ESE trend and low plunges (0°–20°) is observed (Figure 6E). The lineation is marked by the preferred orientation of feldspar and quartz aggregates (Figure 9A). At different scales, a top-to-the-WNW sense of shear is indicated by asymmetric boudins, sigmoidal feldspar porphyroclasts and S-C fabrics (Figure 9B–F).

### 3.3 Microstructural study in the QKYS massif

#### 3.3.1 Microstructural observation

In order to distinguish between solid-state and magmatic microstructures, the microstructural observation is applied by many researchers and proved to be effective (Bouchez *et al*., 1990; Miller & Paterson, 1994; do Nascimento *et al*., 2004; Xue *et al*., 2017, among others). The samples were cut parallel to magnetic/mesoscopic lineation and perpendicular to magnetic/mesoscopic foliation to make XZ thin sections. According to the criteria suggested by Bouchez *et al*. (1990, 1992), Paterson *et al*. (1998), and Vernon (2000), four types of microstructures are discriminated, including (1) magmatic, (2) sub-magmatic, (3) high-temperature solid-state and (4) low-temperature solid-state microstructures. Typical photos of these microstructures are shown in Figure 10, and their spatial distribution shown in Figure 11.

At the northeast of Q, and at the center of K, S and Y plutons, the granites display anhedral, medium- to coarse-grained quartz free of deformation (Figures 10A and 11). Despite slight undulose

extinction in the quartz, the feldspars keep straight twin boundaries and euhedral biotite is no kinks or bent boundaries. These features are typical of magmatic microstructure.

In the northern margin of K pluton, sub-magmatic microstructural features can be observed (Figure 11). Under the microscope, microfractures in plagioclase or K-feldspar are filled by quartz, which is considered as syn-magmatic deformation at the grain-scale in the presence of a residual melt (Figure 10B). Meanwhile, most granites of the northern margin of K are characterized by recrystallized quartz ribbons and K-feldspar core-mantle structure (Figure 10C and D), indicating high-temperature solid-state microstructure.

The foliated to mylonitic gneiss in the northern and southern margins of the massif, and the mylonitic granite with its country rocks in its western margin show low-temperature solid-state microstructure (Figure 11). Plastic deformation in quartz is present in these foliated to mylonitic rocks, marked by undulose extinctions, replacement of primary coarse-grained quartz by smaller and elongated new grains (Figures 7F, 10E and F). Subrounded feldspars behave as rotated porphyroclasts with trans-granular fractures (Figure 10E and F).

3.3.2 Quartz c-axes fabrics

Along the northern, southern, and western margins of the massif, quartz c-axis of the foliated to mylonitic rocks are measured under the microscope by a universal-stage method to estimate deformation temperatures. In the northern margin of the massif, three samples of foliated granite (KY05, KY09 and KY57) and one sample of mylonitic orthogneiss (17JD35) were selected for the analysis of Lattice Preferred Orientation (LPO) of quartz c-axes. Samples KY09 and KY57 are characterized by point maxima around the mineral and stretching lineation (X-axis) and an elongated concentration at the Y-axis (Figure 11), pointing to a combination of prism <c> and prism <a> slip of quartz under medium- to high-temperature condition (500–600 °C; Stipp *et al*., 2002). The sub-maxima surrounding the Z-axis (Figure 11) can be explained by the simultaneous presence of basal <a> in addition to prism <c> and

prism <a> slip. The quartz fabric of KY05 is less clear, with a Z-maximum, a Y-maximum and a subordinate cluster at X-axis, suggesting a combination of basal <a>, prism <a> and a subordinate high-temperature prism <c> slip. Sample 17JD35 is dominated by point maxima around the Z axis, indicating the presence of low-temperature (300–400 °C) basal <a> slip system. In conclusion, a medium- to high-temperature condition for the foliated granite and a low-temperature condition for its country rock, likely with a top-to-the-NE sense of shear, can be derived from these c-axis measurements.

Measurements of quartz c-axes helped to estimate the temperature condition of the top-to-the-SW shearing in the south of the massif. Three samples of mylonitic gneiss (18JD13, 18JD18 and 18JD28) and one mica schist (18JD29) were chosen. They exhibit asymmetric point maxima located close to Z, the foliation pole, pointing to the basal <a> slip as the dominant system. In addition, samples of 18JD28 and 18JD29 contain sub-maxima in-between Z and Y or close to Y, calling to the activity of rhomb <a> slip (Figure 11). According to the natural and experimental data reviewed in Passchier & Trouw (2005), a low-temperature condition (~300–400 °C) is responsible for this LPO pattern of quartz c-axis. Meanwhile, the asymmetrical maxima around Z indicates a top-to-the-SW shearing (Figure 11).

Five mylonite samples (QS27, QS30, QS37, QS43 and 18JD125) were chosen along the western margin of the QKYS massif (Figure 11). Sample QS27, QS30, QS43 and 18JD125 display the asymmetrical point maxima close to the periphery of the great circle and around the Z, implying basal <a> slip (*e.g.*, Bouchez, 1977). Several sub-maxima in-between Z and Y are also presented in these four samples, corresponding to the activity of rhomb <a> slip, attributed to low to medium temperature condition (*e.g.*, Schmid & Casey, 1986, among others). Sample QS37 shows two asymmetrical c-axis concentrations around Y, which is attributed to the rhomb <a> slip. We therefore estimate a low to medium temperature around 350–450 °C for this deformation. Fabric asymmetry reveals a

top-to-the-WNW sense of shear, conformably to field and microscopic observation.

## 4 Anisotropy of magnetic susceptibility (AMS) study

AMS, as applied in many studies relative to granitic massifs, offers an effective way to refine their structural elements, particularly among plutons that appear to be isotropic (*e.g.*, Bouchez, 1997; Archanjo *et al*., 2002; Lehmann *et al*., 2013; Žák *et al*., 2015; Wei *et al*., 2014a, among others).

### 4.1 Sampling and measurement

A total of 111 sampling sites (47 from K pluton, 34 form Q pluton, 18 from S pluton and 12 from Y pluton) were chosen for this study. Except for the southern part of K, where outcrops are limited, granites were evenly sampled with 5 to 8 specimens for each site. They were drilled by a portable gasoline drill, and oriented by a magnetic compass and a solar compass when possible. They were cut into standard specimens with 2.2 cm in length and 2.5 cm in diameter. The AMS measurements were performed using an AGICO Kappabridge magnetic susceptometer (MFK1) that works at a low magnetic field in the Institute of Geology and Geophysics, Chinese Academy of Sciences, Beijing, China. The AMS ellipsoid of a given specimen is characterized by three orthogonal principal axes (in orientation and magnitude). For each site that includes a group of specimens, the AMS data were processed using Anisoft 4.2 software to acquire site-average directions and magnitudes of three principal axes, $K_1 \geq K_2 \geq K_3$ (Jelinek, 1978). The mean magnetic susceptibility ($K_m$) is equal to their average value ($K_m = (K_1+K_2+K_3)/3$). Two magnetic fabric parameters $P_j$ and $T$ represent the degree of anisotropy and the shape of the AMS ellipsoid, respectively. These parameters are defined as following: $P_j=\{2[(\ln K_1-\ln K_m)^2+(\ln K_2-\ln K_m)^2+(\ln K_3-\ln K_m)^2]\}^{1/2}$ and $T=(2\ln K_2-\ln K_1-\ln K_3)/(\ln K_1-\ln K_3)$ (Jelinek, 1981).

Generally, $K_1$ and $K_3$ represent the magnetic lineation and the pole to the magnetic foliation, respectively. To define the magnetic carriers, principally ferromagnetic or paramagnetic, and the

magnetic grain size of the magnetic carriers, principally pseudo-single domain or multidomain in granites, three complementary measurements are necessary: (1) thermomagnetic curves, (2) isothermal remanent magnetization and (3) hysteresis loops. These measurements were performed at the Institute of Geology and Geophysics, Chinese Academy of Sciences, Beijing, China. Thermomagnetic curves were obtained using a heating apparatus attached to the MFK1 susceptometer. Both isothermal remanent magnetization and hysteresis loop measurements were obtained by using a Micro 3900 Vibrating Sample Magnetometer.

### 4.2 Magnetic mineralogy

The mean magnetic susceptibility ($K_m$) of measured sites are presented in Table 1, and the frequency histograms are given in Figure 12. Overall, $K_m$ of S and Y plutons are mostly up to $10^{-2}$ SI in susceptibility, implying that ferromagnetic minerals are the main magnetic susceptibility carriers ($K_m$ > $5\times10^{-3}$ SI, Hrouda & Kahan, 1991; Bouchez, 1997). The K and Q plutons have $K_m$ ranging from $0.09\times10^{-3}$ SI to $57\times10^{-3}$ SI and $0.036\times10^{-3}$ SI to $16\times10^{-3}$ SI, respectively. In these two plutons, both paramagnetic and ferromagnetic minerals are present; the paramagnetic minerals (iron-bearing silicates: biotite and amphibole) become prevailing with a decrease of $K_m$.

All thermomagnetic experiments (Figure 13A, B and C) display a susceptibility drop at the Curie temperature (~ 580 °C), revealing that iron-rich magnetite is the main susceptibility carrier. The low-susceptibility specimens KY29 and QS22 exhibit hyperbolic thermomagnetic curves in their initial parts, up to temperatures about 150°C or 250°C, reflecting a significant contribution (> 50%) of paramagnetic minerals (*e.g.*, Trindade *et al*., 1999). The fact that the cooling curve has a higher magnetic susceptibility than that of the heating curve (for example, KY29 in Figure 13A) indicates that the original magnetic phase has been (partly) transformed into magnetite during heating. At an applied magnetic field less than 200 mT, the isothermal remanent magnetization acquisition diagrams (Figure

13D, E and F) display a positive correlation between the induced magnetization and the applied field. At a higher applied field up to 200 mT, the induced magnetization becomes constant, indicating that our magnetite grains are weakly coercive. The ratios of $M_r/M_s$ and $H_{cr}/H_c$, acquired from the experiments of isothermal remanent magnetization and hysteresis loops, indicate that the magnetic grain-size falls into the pseudo-single domain (Dunlop, 2002; Figure 14). In fact, these characteristics of magnetic minerals are common in the granites (*e.g.*, Trindade *et al*., 1999; do Nascimento *et al*., 2004, among others).

### 4.3 AMS fabric parameters and orientation

In our case, more than 95% of the measured samples of S and Y plutons have low $P_j$, less than 1.2. In K pluton, 70% of the $P_j$ values are less than 1.2 and remaining 30% are mainly distributed along the pluton margin and contact zone with the S pluton (Figure 15A). In Q pluton, 29% of the $P_j$ values exceed 1.2 and are present at its western part where low-temperature solid-state microstructures dominate (Figures 11 and 15A). Majority of susceptibility ellipsoids are oblate, materialized by positive $T$ values: 69% in K pluton; 71% in Q pluton; 92% in S pluton, and 99% in Y pluton (Figure 15B and Table 1), suggesting that planar fabrics are better defined than linear ones. The AMS ellipsoid becomes more oblate along the northern margin of K pluton, western margin of Q pluton, and at the center part of the Y pluton (Figure 15B). There is no positive or negative correlation between $P_j$ and $K_m$, or between $T$ and $K_m$ (Figure 15C and D), implying both the variations of $P_j$ and $T$ are independent with $K_m$ values. Also, there are no obvious correlativity between $P_j$ and $T$ in most parts of these plutons (Figure 15F, G, H and K). However, a rough positive relationship between $P_j$ and $T$ is shown in the region I of K pluton, region II of Q pluton, and in S pluton, implying that the AMS ellipsoids become more anisotropic and more oblate at the same time (Figure 15E, I and J).

The tensorial mean orientation of each axis and confidence ellipses are shown on the lower hemisphere equal-area projection (Figure 16). The orientations are considered as well-defined if their

confidence level ($\alpha_{95max}$+$\alpha_{95min}$) is less than 40° (Table 1). The magnetic foliations (planes normal to $K_3$) and the lineations ($K_1$) are presented in map view of Figure 17, along with the corresponding orientation diagrams giving sectorial summaries. The magnetic foliations of K pluton mainly exhibit concentric patterns, and thereby we grouped them into three regions. In the region I, the granite samples show mainly NE- or NNW- dipping magnetic foliations with small to moderate angles and magnetic lineations in a NNE–SSW trend. They have neutral to oblate AMS ellipsoids and variable values of $P_j$ ranging from 1.038–1.433 (Figure 15E). In the center of K pluton (region II), the poles of magnetic foliations define a broad, NNE–SSW striking girdle in the equal-area plot, and scattered magnetic lineations with gentle plunges are shown. The AMS ellipsoids are dominated by oblateness, and the values of $P_j$ are less than 1.2 (Figure 15F). The samples of region III are marked by inward dipping magnetic foliations with moderate to high angles. In the equal-area plot, the magnetic lineations form a cluster oriented at ENE–WSW and nearly normal to the broad girdle defined by the poles of magnetic foliations. They also show prolate to neutral AMS ellipsoids and variable degrees of anisotropy (Figure 15G). In map view, the magnetic foliations of regions II and III form the "onion-skin" patterns with the margin-parallel magnetic lineations (Figure 17).

In Q pluton, two distinct AMS fabric patterns are present (Figure 17). In region I, the magnetic foliations mainly strike along NW–SE with varying angles (20°–80°) and contain scattered magnetic lineations. Their AMS ellipsoids vary from oblateness to prolateness, with $P_j$ values ranging from 1.038–1.496 (Figure 15H). In region II, the magnetic foliations are mainly sub-horizontal, foliation poles clustering at the center of the equal-area plot. The magnetic lineations display well-defined NW–SE trends and small plunges. Their AMS ellipsoids are mainly oblate, with $P_j$ values ranging from 1.039 to 1.354 (Figure 15I).

In S pluton, the magnetic foliations have gentle outward dips, and the magnetic lineations consistently plunge to the NW or SE with small angles. The AMS ellipsoids display neutral to oblate

shapes with weak anisotropy degrees, $P_j$ ranging from 1.028 to 1.295 (Figure 15J). Concerning Y pluton, the magnetic foliations show the "onion-skin" pattern with nearly margin-parallel magnetic lineations. Hence, the poles of magnetic foliations form a well-defined girdle through the center of the equal-area projection, and the magnetic lineations have variable orientations with predominant outward plunges. The AMS ellipsoids are much more oblate than the other plutons, most *T* values being larger than 0.5 (Figure 15B and K). Their anisotropy degree is weak with $P_j$ values mostly less than 1.2 (Figure 15K).

## 5 Gravity Survey

Gravity survey applied to numerous studies offer a probable way to reveal the geological features at depth (*e.g.*, Guineberteau *et al*., 1987; Vigneresse, 1990; Vigneresse & Bouchez, 1997; Gébelin *et al*., 2006; Turrillot *et al*., 2011, among others). In our study, the gravity map interpretation and gravity modeling were carried out to characterize the unexposed parts shape of the QKYS massif.

### 5.1 Gravity map processing and interpretation

In order to extract the long wavelengths of the Bouguer anomaly, a low-pass Butterworth filter with a cutoff wavelength of 150 km was applied on Bouguer anomaly map of Jiaodong Peninsula. The residual gravity anomaly map, obtained through subtraction of the long wavelengths Bouguer anomaly from the original anomaly map, mainly reflects the density heterogeneities in the upper crust of the Jiaodong Peninsula (Figure 18).

In the residual gravity anomaly map, the iso-gravity trends are nearly parallel to the outcropping plutons' borders at the scale of the Jiaodong Peninsula, and most of the plutons are represented by negative gravity anomalies (Figure 18). In the QKYS massif itself, no substantial contrast appears between the plutons and their country rocks, implying that (1) both the plutons and their country rocks have similar densities; (2) low-density rocks are dominant in addition to plutons; and (3) some plutons

may extend off their outcropping boundaries at depth. A closer examination shows that the residual Bouguer anomaly of the K pluton is elliptical in-shape with a N–S long axis. Its overall decreasing gravity gradient toward the west and south indicates that K pluton becomes thinner and narrower in these directions. Three clearly defined first-order negative anomalies are present in the center of K pluton, in the south of S pluton and close to the contact zone between Q and Y plutons, implying that the deep roots are present in these sectors.

### 5.2 Constraints for 2D gravity modeling

To obtain a realistic geometry of QKYS massif, we measured the density values of plutons and their country rocks by the double-weighing method. We obtained: (1) 2600 kg/m$^3$ and 2580 kg/m$^3$ for Late Jurassic K and Q biotite monzonitic granite and Early Cretaceous S and Y porphyritic granite, respectively; (2) 2670 kg/m$^3$ for Early Cretaceous diorite; (3) 2790 kg/m$^3$ for Paleoproterozoic meta-sedimentary rocks including the paragneiss, schist, amphibolite and marble; (4) 2630 kg/m$^3$ for the gneissic migmatite in the north of the massif, and 2720 kg/m$^3$ for the heavier gneiss to the south of the massif, due to the addition of the meta-mafic lenses; and (5) 2550 kg/m$^3$ for Early Cretaceous volcanic and clastic rocks.

Topographic corrections of the residual anomaly map were performed based on the International Gravimetric Bureau database (Bonvalot *et al*., 2012). Based on our field structural analysis, geological map, residual gravity anomaly map and density measurements, we have built a gravity model in the "Oasis montaj" platform of Geosoft (www.geosoft.com). The density of undifferentiated upper crust was chosen as 2800 kg/m$^3$, according to the Crust 1.0 model of Laske *et al.* (2013). All layers were set to be nearly flat and extend at infinity to avoid edge effects. Finally, each unit in the profiles was considered to have a constant density, appropriate to obtain the best match between measured and calculated gravity values.

### 5.3 Gravity profiles

Five NE–SW-trending and six NW–SE-trending modeled gravity profiles (Figure 19) crosscutting all litho-tectonic units in the study area, allow us to characterize the shape of QKYS massif at depth. According to these gravity profiles, several features can be outlined. The country rocks (gneissic migmatite and meta-sedimentary rocks) of the plutons have a thickness around 5 km. The K and Q plutons are rather batholithic with considerable thickness variations. In the NE–SW profiles, these two plutons count to three roots deeper than ~6 km (Figure 19A–E), and in-between these roots their thickness is 2–3 km. In the NW–SE profiles (Figure 19F–K), the Q pluton has a constant thickness of 2 to 4 km with no obvious deeper root. The K pluton also displays a constant thickness of 2–4 km with no obvious root in profiles F, J and K, and a flat bottom (~5 km) thinning to the northwest and southeast in profiles G, H, and I. When aligning these roots in the gravity map (Figure 18), we argue that the K and Q plutons are made of several NW–SE-trending deeper roots. Concerning the S and Y plutons, both the NE–SW and the NW–SE profiles reveal that they have an inverted drop shape with a single ~5 km deep root (Figure 19). Profiles H to K show that the top of Q pluton is covered by 1 to 2 km-thick Early Cretaceous volcanic and clastic rocks. The contact between Q pluton and Early Cretaceous volcanic and clastic rock is arch-shaped and becomes steep at depth (Figure 19I, J and K).

## 6 Discussion

### 6.1 Origins of the magnetic fabrics

Both the paramagnetic and ferromagnetic minerals (*i.e.*, biotite, amphibole, and magnetite) act as the main AMS carriers, the magnetic fabrics being due to their shape preferred orientation (SPO). The mesoscopic foliation and lineation also result from SPO of the paramagnetic minerals (Figures 2 and 17). In region I of Q pluton and regions I, II and III of K pluton, the granites show concentric magnetic foliations. Predominant NNE–SSW-trending magnetic lineations are present in region I of K

pluton, which are parallel to the linear structures in the northern margin of the K pluton. Away from the northern margin of the K pluton, the magnetic lineations become more scattered (region I of Q pluton and region II of K pluton) or parallel to the magnetic foliation strikes (region III of K pluton). These granite samples are characterized by magmatic, sub-magmatic or high-temperature solid-state microstructures (Figure 11). Combined with the geometric relations of plutons and their country rocks (*c.f.* section 3), we suggest their magnetic fabrics were acquired during the late stages of magma crystallization, recording increments of the regional tectonic strain (*e.g.*, Žák *et al*., 2015; Paterson *et al*., 2019). In region II of Q pluton, the granites have flat magnetic foliations and NW–SE magnetic lineations (Figure 17). They also have low-temperature solid-state microstructures (Figure 11) that correlate well with the higher $P_j$ and $T$ values (Figure 15A and B). Their magnetic fabrics correspond to the mylonitic foliations and lineations observed in the western margin of Q pluton (*e.g.*, Lin *et al*., 2013b).

The S and Y plutons show typical features of isotropic granitoids with magmatic microstructure, low $P_j$, and no post-solidus recrystallization. Together with the extremely fast cooling rate they display (Figure 4D), we argue that their magnetic fabrics are devoid of the influence of regional tectonics (*e.g.*, Paterson et al., 1998; Yoshinobu et al., 1998). In other words, their magnetic fabrics were acquired during magma crystallization without the contribution of syn- or post-emplacement tectonics.

### 6.2 Polyphase deformation and multiple pluton emplacement

Based on field observation and laboratory analyses, a polyphase deformation is recognized in the QKYS massif. The polyphase deformation corresponds to several tectonic events in East China.

#### 6.2.1 $D_1$ deformation and its tectonic significance

Along the northern margin of the massif, mesoscopic foliations of the country rocks

435 (orthogneiss) and the granitic rocks are parallel in orientation, and both contain the NE–SW linear
436 structures with top-to-the-NE kinematics (Figure 20). This event is characterized by high-temperature
437 deformation in the granitic rock and low-temperature deformation conditions in the orthogneiss
438 (Figures 7, 10 and 11), a complete parallelism appearing between the magnetic fabrics and the
439 structural elements of these high- to low-temperature solid-state fabrics (Figure 20). Decrease of $P_j$
440 and $T$ values is interpreted as the strain weakening from the margin to the core of the K pluton (Figure
441 15A and B). The age of first deformation event (*i.e.*, $D_1$ event) is therefore similar to the crystallization
442 age of the syn-kinematic K pluton (*i.e.*, 153 Ma, Figure 4B). The NW–SE trending roots of K and Q
443 plutons are considered as the feeder zones (Figures 18 and 19; *e.g.*, Améglio *et al*., 1997). Location of
444 these feeder zones at the centers of the magnetic foliations concentric patterns naturally implies that the
445 magma upwelled above them (Figures 17, 19 and 20; *e.g.*, Ji *et al*., 2018b).

446 From the view of these structures, a NE–SW extensional tectonics was likely responsible for
447 the $D_1$ event which is characterized by the emplacement of a syn-kinematic pluton (K pluton) and a
448 normal sense of shear. In such a scenario (Figure 21A), the Late Jurassic magma ascent through several
449 feeder zones almost perpendicular to the NE–SW extensional direction (*e.g.*, Vigneresse, 1995), and
450 then expanded laterally along the extensional direction to form a single pluton at the middle crustal level
451 (ca. 15 km). By the end of magma crystallization, due to the progressing extension, a ductile normal
452 shear zone developed on the northern margin of the massif (Figure 21A).

453 6.2.2 Latest Jurassic to Earliest Cretaceous contractional $D_2$ event

454 In the south of the QKYS massif, the ductile shear zone displays a gentle SW dipping foliation,
455 a NE–SW linear structure, and a top-to-the-SW kinematics under low temperature condition (Figures 11
456 and 20). Because this tectonic event was not recognized before, rare geochronological works were
457 documented to constrain its age. Undeformed Early Cretaceous porphyritic granite intruded the
458 mylonitic rocks (Figures 20 and 21), so its crystallization age (118 Ma, Charles *et al.*, 2011b) give a

459 minimum for this event. The amphibole and biotite $^{40}Ar/^{39}Ar$ dating for the gneiss and amphibolite from
460 the lower part of the shear zone yield distinct ages of 219–195 Ma and135–133 Ma, respectively (Figure
461 4C, Chen *et al*., 1992; Wu, 2014; Liu *et al*., 2017a). Considering its low deformation temperature, a little
462 higher than the biotite closure temperature (*ca*. 280–320 °C), and much lower than that of amphibolite
463 (*ca*. 480–550 °C), we interpreted that its timing approaches or slightly earlier than 135 Ma ($D_2$ event).
464 From the viewpoint of the geometry, the SW-dipping foliations with top-to-the-SW shearing
465 could be interpreted as a SW-directed extensional structure. In this case, the north and south shear zones
466 with normal senses of shear could announce the exhumation of a magmatic dome in a NE–SW direction,
467 similarly to the extensional domes in South China (Faure *et al*., 1998; Lin *et al*., 2001) and Montagne
468 Noire in SE France Central Massif (Echtler & Malavieille, 1990). However, two lines of evidence
469 exclude the model of symmetric extension for the QKYS massif. Firstly, no high-temperature plastic
470 flow similar with the $D_1$ shear zone is observed along the southern or southwestern margin of the K
471 pluton. Secondly, to the south of the K pluton, the foliations of the country rocks are oblique with
472 respect to magnetic foliations of pluton, as well as to the granite/orthogneiss contact (Figure 20). From
473 the view of regional geology, similar top-to-the-SW ductile deformations with the ages of 143–138 Ma
474 were recognized in the northern part of NCC and central part of SCB, which are interpreted as NE–SW
475 contractional structures (Davis *et al*., 2001; Lin *et al*., 2013a; Zhu *et al*., 2015; Ji *et al*., 2018a).
476 Considering the Early Cretaceous exhumation and the Late Cretaceous to Cenozoic differential
477 uplifting of the massif, it is reasonable to infer that the dips of the $D_2$ shear zone foliations may vary
478 from NE- to SW-directed (Figure 21B–D). Either its kinematics or timing can be comparable with
479 SW-directed thrusting documented in East China (Davis *et al*., 2001; Lin *et al*., 2013a; Zhu *et al*., 2015;
480 Ji *et al*., 2018a), so we interpret this deformation as an independent event related to the latest Jurassic to
481 earliest Cretaceous NE–SW contractional tectonics.

### 6.2.3 Early Cretaceous extensional $D_3$ event

Along the western margin of the massif, the flat-lying ductile shear zone with a top-to-the-WNW kinematics separates the massif from Early Cretaceous unmetamorphosed volcanic and clastic rocks (Figure 20). The flat magnetic foliations with NW–SE magnetic lineations in region II of the Q pluton is also remarkable of this event (Figure 17). The structural fabrics of the orthogneiss located between Q and K pluton, at odd with the magnetic fabrics of the plutons, suggest a pre-Late Mesozoic deformation (*e.g.*, Faure *et al.*, 2001, 2003). Previous studies considered this shear zone as a detachment fault, therefore pointing to an extensional structure (Shen *et al*., 1998; Xia *et al*., 2016). Meanwhile, the undulated shape of the detachment fault likely results from an extension-parallel corrugation (e.g., Richard et al., 1990). The gravity modeling shows that the flat-lying detachment fault becomes steeper at depth (Figure 19). This geometry likely corresponds to a rolling-hinge structure that was originated from an initial steep fault, favoring the exhumation of the QKYS massif (*e.g.*, Axen *et al*., 1995). Rolled around the hinge of the detachment fault, the footwall rocks were progressively exhumed to reach a shallower crustal level (*e.g.*, Ratschbacher *et al*., 2000; Yin, 2004). Hence, the Q pluton located immediately below the detachment has a younger cooling age than the K pluton which is far from the fault (Figure 4C). When the detachment fault reached the shallower crust, the west-dipping brittle normal fault overprinted the ductile shear zone, hence controlled the development of Early Cretaceous half-graben basin (Figure 21C; e.g., Xia *et al.*, 2016).

The supra-detachment basin is filled by Early Cretaceous volcanic and clastic rocks (Wang et al., 2016), suggesting the same age for the detachment fault. Muscovite and biotite yielded 128–126 Ma and 124–120 Ma $^{40}Ar/^{39}Ar$ ages for the mylonitic Q granite (Figure 4C; Li *et al*., 2006; Zhang *et al*., 2007; Wu, 2014). To the east, $^{40}Ar/^{39}Ar$ ages on biotite samples from K pluton give 130–126 Ma, representing the cooling ages of K pluton. These geochronological data indicate that the 130–120 Ma approaches the true age of the detachment fault, in agreement with a fast cooling rate of the massif

during this period (Figure 4D). Hence, this event took place after $D_2$; it is named $D_3$.

#### 6.2.4 Emplacement of Early Cretaceous plutons

The segregation and ascent of magma is usually commenced by the way of dyking or diapir (*e.g.*, Clemens & Mawer, 1992; Kratinová *et al*., 2006). Thermomechanical models indicate that magma ascent as a diapir is prone to stop at depth, *i.e.*, at the middle to lower crust level (Cao *et al*., 2016). Dou *et al*. (2018) constrained that the S and Y plutons were emplaced at a pressure of 1.8–2.1 kbar by using the experimental Qz-Ab-Or phase diagram, corresponding to depths of 5.4–6.3 km, so the diapir model is inappropriate. Clemens and Mawer (1992) suggested a model of self-propagating dyking in which the magmas should produce the tensile fracturing, and providing the space for magma ascent, while the re-activation of pre-existing weak zones are also expected to facilitate the initiation of dyking (*e.g.*, Baer, 1991). Early Cretaceous S and Y plutons are inverted drop shaped with a single feeder zone as revealed by the gravity profiles (Figure 19), suggesting that they were emplaced through a single sub-vertical weakness zone (*e.g.*, Guineberteau *et al*., 1987; Améglio *et al*., 1997). The magnetotelluric profile of Zhang *et al*. (2018) also supports a highly fractured upper crust in the Jiaodong Peninsula. Hence, the reactivation of pre-existing fractures in the upper crust was probably a preferential mechanism for the emplacement of these plutons (Figure 21D; *e.g.,* Liu *et al*., 2018). At the end of magma ascent, and in absence of regional tectonics, magma convection led to the "onion-skin" magnetic foliations and margin-parallel magnetic lineations of the Y pluton (Figure 17). The gently dipping magnetic foliations recorded in S pluton likely represent the sub-horizontal roof at the top of the pluton (Figure 17).

Two Early Cretaceous plutons, namely Haiyang (118 Ma) and Weideshan pluton (108 Ma) have been documented in the Jiaodong Peninsula (Figure 1). These porphyritic granodiorites share common features with the S and Y plutons (Charles *et al*., 2011b), namely: (1) typical isotropic textures without obvious solid-state fabrics; (2) sub-horizontal and outward dipping magnetic foliations with scattered magnetic lineations; and (3) a fast cooling rate revealed by zircon U-Pb and biotite $^{40}Ar/^{39}Ar$ ages.

Accordingly, isotropic pluton emplacement, devoid of the influence of regional tectonics and whose emplacement was controlled by pre-existing structures, have prevailed during the 118–108 Ma time interval.

### 6.3 Tectonic significance of the polyphase deformation in the QKYS massif

Polyphase deformation and multiple magmatic events recorded in the QKYS massif helped us to understand the Late Mesozoic tectonic evolution of East China (Figure 22). The Late Jurassic volcanic rocks and simultaneous felsic intrusions are widely distributed in the Yanshan-Yinshan belt, Liaodong Peninsula and Jiaodong Peninsula, forming a magmatic flare-up between 170 and 150 Ma in East China (Wu *et al*., 2019). Coeval with this intensive magmatism, extensional basins are well-developed in East China, suggesting a Late Jurassic extensional tectonics (Meng, 2003; Cope et al., 2007; Faure *et al*., 2012; Dong *et al*., 2015). In our case, the $D_1$ event with a top-to-the-NE kinematics, accompanied by syn-kinematic magmatism (referred to $Mag_1$), also supports the view of a significant episode of Late Jurassic extensional tectonics (Figure 22A).

In East China, long-term magmatism lasts from 170 to 110 Ma with a significant "magmatic gap" between 150 and 135 Ma, inferring a $J_3$–$K_1$ contractional tectonics (Li, 2000; Wu *et al*., 2019). The regional unconformity and E–W fold and thrust structures also indicate a NE–SW contractional tectonics during the latest Jurassic–earliest Cretaceous (Wong *et al*., 1929, among others). A representative southward thrusting named Gubeikou fault is dated at148–132 Ma in the Yanshan area (Davis *et al*., 2001). In the Lingyuan-Qinglong area, a regional SE-directed thrusting, previously considered by Davis *et al*. (2009) as Late Triassic or pre-middle Jurassic, was recognized as a latest Jurassic event by Hu *et al*. (2010). A $J_3$–$K_1$ SE-directed thrusting also has been documented in the Liaodong Peninsula (Qiu *et al*., 2018). Even though the fold and thrust structures have variable directions, ductile deformation events developed in the Sihetang, Yiwulüshan, and Jiaodong Peninsula,

referred to as the $D_2$ event in this study, pointing to a top-to-the-SW kinematics (a summary in the Figure 22B; Davis *et al*., 2001; Lin *et al*., 2013a; Zhu *et al*., 2015).

Recognition of Early Cretaceous extensional $D_3$ event in the study area is consistent with previous studies about MCC, magmatic domes, syn-kinematic plutons, and detachment faults in East China (Figure 22C; Davis *et al*., 2002, among others). These extensional structures share common features, such as the conspicuous NW–SE linear structures with either top-to-the-NW or top-to-the-SE kinematics, coupled supra-detachment basins (Lin & Wei, 2018). The dating of syn-kinematic minerals constrains these structures to be 130–115 Ma in age, in agreement with the timing of the $D_3$ event of QKYS massif (Wang *et al*., 2012; Zhu *et al*., 2015; Lin & Wei, 2018 and references therein). In this period, several extensional basins, intensive magmatism, and gold mineralization likewise occurred in East China, associated with the extensional tectonics (Ren *et al*., 2002; Meng, 2003; Lin *et al*., 2019). After then, fractures development in the upper crust provided the channels for Early Cretaceous magma, here referred to $Mag_2$ event.

### 6.4 Geodynamic Implications

Geodynamics of the Jurassic–Cretaceous tectonics of East China remains enigmatic. Several models have been proposed, including (1) subduction of the Izanagi plate beneath Eastern Eurasian continent (Xu & Wang 1983; Zhu *et al*., 2011, 2012); (2) closure of the Mongol-Okhostk Ocean (Yin & Nie, 1996; Davis *et al*., 2001); (3) collision between the Lhasa and the Qiangtang terranes (Ma *et al*., 2017). Subduction of Izanagi Plate with the slab roll-back is responsible for the Late Mesozoic extension in East China (Ren *et al*., 2002; Zhu *et al*., 2011, 2012). Induced by the Izanagi Plate subduction, partial melting of lower crust took place at Late Jurassic, forming the intermediate to felsic calc-alkalic magmatism in East China (*e.g.*, Li *et al*., 2019). Recently, Wu *et al*. (2019) proposed that the Izanagi Plate subduction angle changed from steep to flat, followed by slab roll-back

576 during Jurassic–Early Cretaceous times to interpret the episodic extensional and contractional
577 tectonics in East China. In our case, the Late Jurassic NE–SW extension ($D_1$) and the Early
578 Cretaceous NW–SE extension ($D_3$) also corresponds to the subduction direction variation deduced
579 from the model of Mattauer et al. (1997) (Figure 22). Final closure of the Mongol-Okhotsk ocean is
580 constrained at Late Jurassic–Early Cretaceous according to the paleomagnetic results (van der Voo *et*
581 *al*., 2015). It is likely to interpret the $J_3$–$K_1$ contractional tectonics and "magma quiescence" in East
582 China, as previously proposed by Yin & Nie (1996) and Davis *et al*. (2001). However, the
583 non-significant reactivation of the Solonker-Xilamulun belt, located between the Mongol-Okhotsk and
584 NCC and considered as a weak zone due to the Late Paleozoic accretionary orogenic belt, is not well
585 explained (*e.g.*, Lin *et al*., 2013a). Ratschbacher *et al*. (2000) proposed that the model of interaction
586 between Pacific back-arc extension and tectonic escape related to the collision between Qiangtang and
587 Lhasa is a possible mechanism to explain Early Cretaceous extension. However, recent SKS wave
588 splitting data seem to discard the eastward escape of the NCC (Zhao *et al*., 2011).

589 The rapid change from the latest Jurassic to earliest Cretaceous crustal contraction($J_3$–$K_1$) to
590 Early Cretaceous crustal extension favors that a previous thickened has a significant effect on
591 subsequent intense crustal extension. From the view of regional tectonics, multi-plate convergence
592 around East China may account for its crustal thickening at latest Jurassic to earliest Cretaceous (*e.g.*,
593 Dong *et al*., 2015). Numerical modeling also suggests that a thickened continental crust facilitates the
594 decoupling between the upper crust and the lower crust, leading to intensive extension (Gueydan *et al.*,
595 2008). Furthermore, the model of lithosphere foundering is speculated to be a significant mechanism
596 that resulted in the loss of the lithospheric root beneath East China, through which the continental crust
597 and lithospheric mantle are highly decoupled (Lin & Wang, 2006; Lin & Wei, 2018). Subsequent
598 asthenospheric upwelling led a high mantle heat flux able to weaken the middle-lower crust, favoring
599 the setting of the exhuming domes (Brun *et al*., 2018). In a plate tectonic framework (Figure 22C), the

NW-directed subduction of the Izanagi Plate and its subsequent roll-back may enhanced the lithospheric foundering at the origin of the vast extensional tectonics during the Early Cretaceous (*e.g.*, Lin & Wei, 2018; Chu *et al*., 2019).

## 7 Conclusions

Three phases of deformation and two periods of magmatism recognized in a single area (QKYS massif) allow us to understand Late Mesozoic episodic intracontinental extension and contraction of East China. We have presented detailed structural analyses, magnetic fabrics and gravity modeling, documenting an Late Mesozoic extension-contraction-extension history that QKYS massif experienced. Our new data, together with published work, suggests that East China suffered Late Jurassic NE–SW extension, latest Jurassic–earliest Cretaceous NE–SW contraction, then to Early Cretaceous NW–SE extension. This periodicity likely links with the subduction of Izanagi Plate beneath Eurasian continent, inferring a variation from oblique to orthogonal subduction during the Late Mesozoic.

## Acknowledgements

We thank the Editor in Chief Prof. Laurent Jolivet, Associate Editor, Prof. Jean-luc Bouchez, Prof. Jeremie Lehmann and Prof. Jiří Žák for their constructive comments and suggestions that were helpful to improve the manuscript. The manuscript benefited greatly from discussions with Prof. Michel Faure, Dr. Wei Wei and Dr. Yang Chu. Dr. Zhiheng Ren, Dr. Huabiao Qiu, Mr. Jipei Zeng and Mr. Zhentian Feng are acknowledged for their help in the field work. This study was funded by the Chinese Ministry of Science and Technology (2016YFC0600102) and the National Natural Science Foundation of China (91855212). All data can be archived online in https://doi.org/10.6084/m9.figshare.11313335.v5.

## References

622 Améglio, L., Vigneresse, J. L., & Bouchez, J. L. (1997). Granite pluton geometry and emplacement
623 mode inferred from combined fabric and gravity data. *In* J. L. Bouchez, D. H. W. Hutton, & W. E.
624 Stephens (*Eds.*), Granite: From segregation of melt to emplacement fabrics (pp. 199–214). Paris:
625 Springer Science & Business Media. https://doi.org/10.1007/978-94-017-1717-5_6

626 Archanjo, C. J., Trindade, R. I. F., Bouchez, J. L., & Ernesto, M. (2002). Granite fabrics and
627 regional-scale strain partitioning in the Seridó belt (Borborema Province, NE Brazil). *Tectonics, 21*(1), 1003. https://doi.org/10.1029/2000tc001269

629 Avouac, J. P., Tapponnier, P., Bai, M., You, H., & Wang, G. (1993). Active thrusting and folding along
630 the Northern Tien Shan and late Cenozoic rotation of the Tarim relative to Dzungaria and
631 Kazakhstan. *Journal of Geophysical Research 98* (B4), 6755–6804.
632 https://doi.org/10.1029/92jb01963

633 Axen, G. J., Bartley, J. M., & Selverstone, J. (1995). Structural expression of a rolling hinge in the
634 footwall of the Brenner Line normal fault, eastern Alps. *Tectonics, 14*(6), 1380–1392.
635 https://doi.org/10.1029/95tc02406

636 Baer, G. (1991). Mechanisms of dike propagation in layered rocks and in massive, porous sedimentary
637 rocks. *Journal of Geophysical Research, 96*, 11911–11929. https://doi.org/10.1029/91JB00844

638 Bouchez, J. L. (1977). Plastic deformation of quartzites at low temperature in an area of natural strain
639 gradient. *Tectonophysics, 39*(1-3), 25–50. https://doi.org/10.1016/0040-1951(77)90086-5

640 Bouchez, J. L., Gleizes, G., Djouadi, T., & Rochette, P. (1990). Microstructure and magnetic
641 susceptibility applied to emplacement kinematics of granites: the example of the Foix pluton
642 (French Pyrenees). *Tectonophysics, 184*(2), 157–171.
643 https://doi.org/10.1016/0040-1951(90)90051-9

644 Bouchez, J. L., Delas, C., Gleizes, G., Nédélec, A., & Cuney, M. (1992). Submagmatic microfractures

in granites. *Geology, 20*(1), 35–38. https://doi.org/10.1130/0091-7613(1992)020<0035:smig>2.3.co;2

Bouchez, J. L. (1997). Granite is never isotropic: An introduction to AMS studies of granitic rocks. *In* Bouchez, J. L., Hutton, D. H. W., & Strphens, W. E. (*Eds.*), Granite: From Segregation of Melt to Emplacement Fabrics (pp. 95–112). Paris: Springer Science & Business Media. https://doi.org/10.1007/978-94-017-1717-5_6

Bonvalot, S., Balmino, G., Briais, A., Kuhn, M., Peyrefitte, A., Vales, N., et al. (2012). World gravity map. (1:50000000 map), BGI-CGMWCNES-IRD, Paris.

Brun, J. P., Sokoutis, D., Tirel, C., Gueydan, F., Driessche, J. V. D., & Beslier, M. -O. (2018). Crustal versus mantle core complexes. *Tectonophysics, 746*(30), 22–45. https://doi.org/10.1016/j.tecto.2017.09.017

Cao, W., Kaus, B. J. P., & Paterson, S. (2016). Intrusion of granitic magma into the continental crust facilitated by magma pulsing and dike-diapir interactions: Numerical simulations. *Tectonics, 35*, 1575–1594, https://doi.org/10.1002/2015TC004076.

Charles, N., Chen, Y., Augier, R., Gumiaux, C., Lin, W., & Faure, M., et al. (2011b). Palaeomagnetic constraints from granodioritic plutons (Jiaodong Peninsula): new insights on Late Mesozoic continental extension in eastern Asia. *Physics of the Earth and Planetary Interiors, 187*, 276–291. https://doi.org/10.1016/j.pepi.2011.05.006

Charles, N., Gumiaux, C., Augier, R., Chen, Y., Zhu, R. X., & Lin, W. (2011a). Metamorphic core complex *vs.* synkinematic pluton in continental extension setting: Insights from key structures (Shandong Province, eastern China). *Journal of Asian Earth Sciences, 40*(1), 261–278. https://doi.org/10.1016/j.jseaes.2010.07.006

Chen, A. (1998). Geometric and kinematic evolution of basement-cored structure: intraplate orogenesis

668 within the Yanshan Orogen, North China. *Tectonophysics, 292*, 17–42.
669 https://doi.org/10.1016/S0040-1951(98)00062-6

670 Chen, W., Harrison, T. M., Heizler, M.T., Liu, R., Ma, B. & Li, J. (1992). The cooling history of
671 melange zone in north Jiangsu–south Shandong region: evidence from multiple diffusion
672 domain $^{40}$Ar-$^{39}$Ar thermal geochronology. *Acta Petrologica Sinica, 8*, 1–17. (in Chinese with
673 English abstract).

674 Chu, Y., & Lin, W. (2018). Strain analysis of the Xuefengshan Belt, South China: From internal strain
675 variation to formation of the orogenic curvature. *Journal of Structural Geology, 116*, 131–145.
676 https://doi.org/10.1016/j.jsg.2018.08.002

677 Chu, Y., Faure, M., Lin, W., & Wang, Q. (2012). Early Mesozoic tectonics of the South China block:
678 insights from the Xuefengshan intracontinental orogen. *Journal of Asian Earth Sciences, 61*,
679 199–220. https://doi.org/10.1016/j.jseaes.2012.09.029

680 Chu, Y., Lin, W., Faure, M., Xue, Z., Ji, W., & Feng, Z. (2019). Cretaceous episodic extension in the
681 South China Block, East Asia: evidence from the Yuechengling massif of Central South
682 China. *Tectonics, 38*(10), 3675–3702. http://doi.org/10.1029/2019TC005516

683 Clemens, J. D., & Mawer, C. K. (1992). Granitic magma transport by fracture propagation.
684 *Tectonophysics, 204*, 339–360. https://doi.org/10.1016/0040-1951(92)90316-X

685 Cong, B., Zhai, M., Carswell, D.A., Wilson, R.N., Wang, Q., & Zhao, Z., et al. (1995). Petrogenesis of
686 ultrahigh-pressure rocks and their country rocks at Shuanghe in Dabieshan, Central China.
687 *European Journal of Mineralogy, 7*, 119–138. https://doi.org/10.1016/10.1127/ejm/7/1/0119

688 Cope, T. D., Shultz, M. R., & Graham, S. A. (2007). Detrital record of Mesozoic shortening in the
689 Yanshan belt, NE China: testing structural interpretations with basin analysis. *Basin*
690 *Research, 19*(2), 253–272. https://doi.org/10.1111/j.1365-2117.2007.00321.x

691 Coward, M. P., Butler, R. W. H., Khan, M. A., & Knipe, R. J. (1987). The tectonic history of Kohistan
692 and its implications for Himalayan structure. *Journal of the Geological Society, 144*(3), 377–
693 391. http://doi.org/10.1144/gsjgs.144.3.0377

694 Darby, B. J., & Ritts, B. D. (2002). Mesozoic contractional deformation in the middle of the Asian
695 tectonic collage: the intraplate western Ordos fold–thrust belt, China. *Earth and Planetary*
696 *Science Letters, 205*(1), 13–24. https://doi.org/10.1016/S0012-821X(02)01026-9

697 Davis, G. H. (1983). Shear-zone model for the origin of metamorphic core complexes. *Geology*, 11(6),
698 342. https://doi.org/10.1130/0091-7613(1983)11<342:smftoo>2.0.co;2

699 Davis, G. A., Darby, B. J., Zheng, Y., & Spell, T. L. (2002). Geometric and temporal evolution of an
700 extensional detachment fault, Hohhot metamorphic core complex, inner Mongolia,
701 China. *Geology*, *30*(11), 1003–1006.
702 https://doi.org/10.1130/0091-7613(2002)030<1003:GATEOA>2.0.CO;2

703 Davis, G. A., Meng, J., Cao, W., & Du, X. Q. (2009). Triassic and Jurassic tectonics in the eastern
704 Yanshan belt, North China: insights from the controversial Dengzhangzi formation and its
705 neighboring units. *Earth Science Frontiers*, *16*(3), 69–86.
706 https://doi.org/10.1016/S1872-5791(08)60090-1

707 Davis, G. A., Zheng, Y. D., Wang, C., Darby, B. J., Zhang, C. H., & Gehrels, G. (2001). Mesozoic
708 tectonic evolution of the Yanshan fold and thrust belt, with emphasis on Hebei and Liaoning
709 provinces, northern China. *Geological Society of America Memoirs*, *194*, 171–194.
710 https://doi.org/10.1130/0-8137-1194-0.171

711 Dickinson, W. R., & Snyder, W. S. (1978). Plate tectonics of the Laramide orogeny. *In*: Matthews Ili,
712 V (*Ed.*), Laramide Folding Associated with Basement Block Faulting in the Western United
713 States. *Geological Society of America Memoir*, *151*, 55–366.

do Nascimento, H. S., Bouchez, J. L., Nédélec A., & Sabaté P. (2004). Evidence of an early NS magmatic event in the Paleoproterozoic Teofilandia granitoids (Sao Francisco Craton, Brazil): a combined microstructural and magnetic fabric study. *Precambrian Research, 134*(1-2), 41–59.

Dong, S., Zhang, Y., Zhang, F., Cui, J., Chen, X., & Zhang, S., et al. (2015). Late Jurassic–Early Cretaceous continental convergence and intracontinental orogenesis in East Asia: a synthesis of the Yanshan revolution. *Journal of Asian Earth Sciences, 114,* 750–770. https://doi.org/10.1016/j.jseaes.2015.08.011

Dou, J.-Z., Zhang, H.-F., Tong, Y., Wang, F., Chen, F.-K., & Li, S.-R. (2018). Application of geothermo-barometers to Mesozoic granitoids in the Jiaodong Peninsula, eastern China: Criteria for selecting methods of pressure estimation and implications for crustal exhumation. *Journal of Asian Earth Sciences, 160,* 271–286. https://doi.org/10.1016/j.jseaes.2018.01.019

Dunlop, D. J. (2002). Theory and application of the Day plot (Mrs/Ms versus Hcr/Hc) 1. Theoretical curves and tests using titanomagnetite data. *Journal of Geophysical Research, 107*(B3). https://doi.org/10.1029/2001jb000486

Echtler, H., & Malavieille, J. (1990). Extensional tectonics, basement uplift and Stephano-Permian collapse basin in a late Variscan metamorphic core complex (Montagne Noire, Southern Massif Central). *Tectonophysics, 177*(1-3), 125–138. https://10.1016/0040-1951(90)90277-f

Faure, M., Lin, W., & Breton, N. L. (2001). Where is the North China-South China boundary in eastern China? *Geology, 29*(2), 119–122. https://doi.org/10.1130/0091-7613(2001)029<0119:WITNCS>2.0.CO;2

Faure, M., Lin, W., & Chen, Y. (2012). Is the Jurassic (Yanshanian) intraplate tectonics of north China due to westward indentation of the North China Block? *Terra Nova, 24*(6), 456–466. https://doi.org/10.1111/ter.12002

737 Faure, M., Lin, W., Monié, P., Le Breton, N., Poussineau, S., & Panis, D., et al. (2003). Exhumation
738 tectonics of the ultrahigh-pressure metamorphic rocks in the Qinling orogen in east China: New
739 petrological-structural-radiometric insights from the Shandong Peninsula. *Tectonics, 22*(3),
740 1018. https://doi.org/10.1029/2002TC001450

741 Faure, M., Lin, W., Shu, L. S., Sun, Y., & Scharer, U. (1999). Tectonics of the Dabieshan (eastern China)
742 and possible exhumation mechanism of ultra-high-pressure rocks. *Terra Nova, 11*, 251–258.
743 https://doi.org/10.1046/j.1365-3121.1999.00257.x

744 Faure, M., Lin, W., & Sun, Y. (1998). Doming in the southern foreland of the Dabieshan (Yangtse block,
745 China). *Terra Nova, 10*(6), 307–311. https://doi.org/10.1046/j.1365-3121.1998.00207.x

746 Gébelin, A., Martelet, G., Chen, Y., Brunel, M., & Faure, M. (2006). Structure of late Variscan
747 Millevaches leucogranite massif in the French Massif Central: AMS and gravity modeling
748 results. *Journal of Structural Geology, 28*(1), 148–169.
749 https://doi.org/10.1016/j.jsg.2005.05.021

750 Goss, S. C., Wilde, S. A., Wu, F., & Yang, J. (2010). The age, isotopic signature and significance of the
751 youngest Mesozoic granitoids in the Jiaodong terrane, Shandong province, North China
752 Craton. *Lithos, 120*(3), 309–326. https://doi.org/10.1016/j.lithos.2010.08.019

753 Gueydan, F., Morency, C., & Brun, J. P. 2008. Continental rifting as a function of lithosphere mantle
754 strength. *Tectonophysics, 460,* 83–93. https://doi.org/10.1016/j.tecto.2008.08.012

755 Guineberteau, B., Bouchez, J. L., & Vigneresse, J. L. (1987). The Mortagne granite pluton (France)
756 emplaced by pull-apart along a shear zone: Structural and gravimetric arguments and regional
757 implication. *Geological Society of America Bulletin*, *99*(6), 763–770.
758 https://doi.org/10.1130/0016-7606

759 Guo, J. H., Chen, F. K., Zhang, X. M., Siebel, W., & Zhai, M. G. (2005). Evolution of syn- to

post-collisional magmatism from north Sulu UHP belt, eastern China: zircon U-Pb geochronology. *Acta Petrologica Sinica, 21*(4), 1281–1301. (in Chinese with English abstract).

Hacker, B. R., Wallis, S. R., Mcwilliams, M. O., & Gans, P. B. (2009). $^{40}Ar/^{39}Ar$ constraints on the tectonic history and architecture of the ultrahigh-pressure Sulu orogen. *Journal of Metamorphic Geology, 27*(9), 827–844. https://doi.org/10.1111/j.1525-1314.2009.00840.x

Hacker, B. R., Wallis, S. R., Ratschbacher, L., Grove, M., & Gehrels, G. (2006). High-temperature geochronology constraints on the tectonic history and architecture of the ultrahigh-pressure Dabie-Sulu Orogen. *Tectonics, 25*, TC5006. https://doi.org/10.1029/2001JB001129/2005TC001937

Hacker, B. R., Ratschbacher, L., Webb, L. E., Ireland, T., Walker, D., & Dong, S. W. (1998). U/Pb zircon ages constrain the architecture of the ultrahigh-pressure Qinling-Dabie orogen, China. *Earth and Planet Science Letters, 161*, 215–230. https://doi.org/10.1016/s0012-821x(98)00152-6

Hu, F., Fan, H., Yang, J., Wan, Y., Liu, D., & Zhai, M., et al. (2004). Mineralizing age of the Rushan lode gold deposit in the Jiaodong Peninsula: SHRIMP U-Pb dating on hydrothermal zircon. *Chinese Science Bulletin, 49*(15), 1629–1636. https://doi.org/10.1007/bf03184134

Hu, J., Zhao, Y., Liu, X., & Xu, G. (2010). Early Mesozoic deformations of the eastern Yanshan thrust belt, northern China. *International Journal of Earth Sciences, 99*(4), 785–800. https://doi.org/10.1007/s00531-009-0417-5

Hrouda, F., & Kahan, S. (1991). The magnetic fabric relationship between sedimentary and basement nappes in the High Tatra Mountains, N. Slovakia. *Journal of Structural Geology, 13*(4), 431–442. https://doi.org/10.1016/0191-8141(91)90016-c

Jelinek, V. (1978). Statistical processing of anisotropy of magnetic susceptibility measured on groups of specimens. *Studia Geophysica et Geodaetica, 22*(1), 50–62.

https://doi.org/10.1007/BF01613632

Jelinek, V. (1981). Characterization of the magnetic fabric of rocks. *Tectonophysics, 79*, 63–67. https://doi.org/10.1016/0040-1951(81)90110-4

Ji, W., Chen, Y., Chen, K., Wei, W., Faure, M., & Lin, W. (2018b). Multiple emplacement and exhumation history of the late mesozoic dayunshan–mufushan batholith in southeast china and its tectonic significance: 2. magnetic fabrics and gravity survey. *Journal of Geophysical Research: Solid Earth, 123*, 711–731. https://doi.org/10.1002/ 2017JB014597

Ji, W., Faure, M., Lin, W., Chen, Y., Chu, Y., & Xue, Z. (2018a). Multiple emplacement and exhumation history of the Late Mesozoic Dayunshan–Mufushan batholith in southeast China and its tectonic significance: 1. Structural analysis and geochronological constraints. *Journal of Geophysical Research: Solid Earth, 123*, 689–710. https://doi.org/10.1002/2017JB014597

Kratinová, Z., Závada, P., Hrouda, F., & Schulmann, K. (2006). Non-scaled analogue modelling of AMS development during viscous flow: A simulation on diapir-like structures. *Tectonophysics, 418*(1), 51–61. https://doi.org/10.1016/j.tecto.2005.12.013

Laske, G., Masters, G., Ma, Z., & Pasyanos, M. (2013). Update on CRUST1.0 — A1-Degree Global Model of Earth's Crust. EGU General Assembly Conference Abstracts.

Lehmann, J., Schulmann, K., Edel, J. B., Jezek, J., Hrouda, F., & Lexa, O., et al. (2013). Structural and anisotropy of magnetic susceptibility records of granitoid sheets emplacement during growth of a continental gneiss dome (Central sudetes, European Variscan Belt). *Tectonics, 32*(3), 797–820. https://doi.org/10.1002/tect.20028

Li, J., & Hou, G. (2018). Cretaceous stress field evolution and origin of the Jiaolai Basin, Eastern North China. *Journal of Asian Earth Sciences, 160*, 258–270. https://doi.org/10.1016/j.jseaes.2018.01.024

Li, J. W., Paulo, V., Zhou, M. F., Zhao, X. F., & Ma, C. Q. (2006). Geochronology of the Pengjiakuang and Rushan gold deposits, Eastern Jiaodong Gold province, Northeastern China: Implications for regional mineralization and geodynamic setting. *Economic Geology, 101*(5), 1023–1038. https://doi.org/10.2113/gsecongeo.101.5.1023

Li, S., Suo, Y., Li, X., Zhou, J., Santosh, M., & Wang, P., et al. (2019). Mesozoic tectono-magmatic response in the East Asian ocean-continent connection zone to subduction of the Paleo-Pacific Plate. *Earth-Science Reviews*, *192*, 91–137. https://doi.org/10.1016/j.earscirev.2019.03.003

Li, X. H. (2000). Cretaceous magmatism and lithospheric extension in southeast China. *Journal of Asian Earth Sciences, 18,* 293–305. https://doi.org/10.1016/S1367-9120(99)00060-7

Li, X. H., Chen, F., Guo, J. H., Li, Q. L., Xie, L. W., & Siebel, W. (2007). South China provenance of the lower-grade Penglai Group north of the Sulu UHP orogenic belt, eastern China: Evidence from detrital zircon ages and Nd-Hf isotopic composition. *Geochemical Journal, 41*, 29–45. https://doi.org/10.2343/geochemj.41.29

Lin, W., Charles, N., Chen, K., Chen, Y., Faure, M., & Wu, L., et al. (2013b). Late Mesozoic compressional to extensional tectonics in the Yiwulüshan massif, NE China and its bearing on the evolution of the Yinshan–Yanshan orogenic belt. Part II: Anisotropy of magnetic susceptibility and gravity modeling. *Gondwana Research*, *23*(1), 78–94. https://doi.org/10.1016/j.gr.2012.02.012

Lin, W., Chen, Y., Faure, M., & Wang, Q. (2003). Tectonic implications of new Late Cretaceous paleomagnetic constraints from Eastern Liaoning Peninsula, NE China. *Journal of Geophysical Research: Solid Earth*, *108*(B6). https://doi.org/10.1029/2002jb002169

Lin, W., Faure, M., Chen, Y., Ji, W. B., Wang, F., & Wu, L., et al. (2013a). Late Mesozoic compressional to extensional tectonics in the Yiwulüshan massif, NE China and its bearing on the evolution of

the Yinshan–Yanshan orogenic belt. Part I: Structural analyses and geochronological constraints. *Gondwana Research, 23*(1), 54–77. https://doi.org/10.1016/j.gr.2012.02.013

Lin, W., Faure, M., Sun, Y., Shu, L., & Wang, Q. (2001). Compression to extension switch during the Middle Triassic orogeny of Eastern China: the case study of the Jiulingshan massif in the southern foreland of the Dabieshan. *Journal of Asian Earth Sciences, 20*(1), 31–43. https://doi.org/10.1016/s1367-9120(01)00020-7

Lin, W., & Wang, Q. (2006). Late Mesozoic extensional tectonics in North China Block— response to the Lithosphere removal of North China Craton? *Bulletin de la Société Géologique de France, 177*, 287–294.

Lin, W., & Wei, W. (2018). Late Mesozoic extensional tectonics in the North China Craton and its adjacent regions: a review and synthesis. *International Geology Review*, 1–29. https://doi.org/10.1080/00206814.2018.1477073

Lin, W., Xu, D., Hou, Q., Li, S., Meng, L., & Ren, Z., et al. (2019). Early Cretaceous extensional dome and related polymetallic mineralization in the Central and Eastern China. *Geotectonica et Metallogenia, 43*(3), 409–430. (in Chinese with English abstract).

Liu, F. L., & Liou, J. G. (2011). Zircon as the best mineral for P–T–time history of UHP metamorphism: A review on mineral inclusions and U–Pb SHRIMP ages of zircons from the Dabie–Sulu UHP rocks. *Journal of Asian Earth Sciences, 40*(1), 1–39. https://doi.org/10.1016/j.jseaes.2010.08.007

Liu, F., Liu, L., Liu, P., Wang, F., Cai, J., & Liu, J., et al. (2017a). A relic slice of Archean–early Paleoproterozoic basement of Jiaobei Terrane identified within the Sulu UHP belt: Evidence from protolith and metamorphic ages from meta-mafic rocks, TTG–granitic gneisses, and metasedimentary rocks in the Haiyangsuo region. *Precambrian Research, 303*, 117–152.

https://doi.org/10.1016/j.precamres.2017.03.014

Liu, H., Martelet, G., Wang, B., Erdmann, S., Chen, Y., & Faure, M., et al. (2018). Incremental emplacement of the Late Jurassic midcrustal, lopolith-like Qitianling pluton, South China, revealed by AMS and Bouguer gravity data. *Journal of Geophysical Research: Solid Earth, 123*. https://doi.org/10.1029/2018JB015761

Liu, J. L., Shen, L., Ji, M., Guan, H. M., Zhang, Z. C., & Zhao, Z. D. (2013). The Liaonan/Wanfu metamorphic core complexes in the Liaodong Peninsula: Two stages of exhumation and constraints on the destruction of the North China Craton. *Tectonics, 32*(5), 1121–1141. https://doi.org/10.1002/tect.20064

Liu, L. P., Li, Z.-X., Danišík, M., Li, S., Evans, N., Jourdan, F., & Tao, N. (2017b). Thermochronology of the Sulu ultrahigh-pressure metamorphic terrane: Implications for continental collision and lithospheric thinning. *Tectonophysics, 712-713*, 10–29. https://doi.org/10.1016/j.tecto.2017.05.003

Ma, A., Hu, X., Garzanti, E., Han, Z., & Lai, W. (2017). Sedimentary and tectonic evolution of the Southern Qiangtang basin: implications for the Lhasa-Qiangtang collision timing. *Journal of Geophysical Research Solid Earth*, 122. https://doi.org/10.1002/2017JB014211.

Maruyama, S., Isozaki, Y., Kimura, G., & Terabayashi, M. (1997). Paleogeographic maps of the Japanese Islands: Plate tectonic synthesis from 750 Ma to present: *Island Arc, 6*, 121–142. https://doi.org/10.1111/j.1440-1738.1997. tb00043.x

Mattauer, M., Matte, P., Malavieille, J., Tapponnier, P., Maluski, H., & Xu, Z. Q., et al. (1985). Tectonics of the Qinling Belt: build-up and evolution of eastern Asia. *Nature, 317*(6037), 496–500. https://doi.org/10.1038/317496a0

874 Meng, Q. R. (2003). What drove late Mesozoic extension of the northern China–Mongolia tract?
875 *Tectonophysics, 369*(3–4), 155–174. https://doi.org/10.1016/S0040-1951(03)00195-1

876 Menzies, M. A, Fan, W, & Zhang, M. (1993). Palaeozoic and Cenozoic lithoprobes and the loss of >120
877 km of Archaean lithosphere, Sino-Korean craton, China. *Magmatic Processes and Plate*
878 *Tectonics, 76*(1), 71–81. http://dx.doi.org/10.1144/GSL.SP.1993.076.01.04

879 Miller, R. B., & Paterson, S. R. (1994). The transition from magmatic to high-temperature solid-state
880 deformation: implications from the Mount Stuart batholith, Washington. *Journal of Structural*
881 *Geology, 16*(6), 853–865. https://doi.org/10.1016/0191-8141(94)90150-3

882 Miller, R. B., Paterson, S. R., & Matzel, J. P. (2009). Plutonism at different crustal levels: Insights from
883 the ~5–40 km (paleodepth) North Cascades crustal section, Washington. *Geological Society of*
884 *America Special Paper, 456*, 125–149. https://doi.org/10.1130/2009.2456(05)

885 Paterson, S. R., Ardilla, K., Vernon, R., & Žák, J. (2019). A review of mesoscopic magmatic structures
886 and their potential for evaluating the hypersolidus evolution of intrusive complexes. *Journal of*
887 *Structural Geology, 125*, 134–147. https://doi.org/10.1016/j.jsg.2018.04.022

888 Paterson, S. R., Fowler, T. K., Schmidt, K. L., Yoshinobu, A. S., Yuan, E. S., & Miller, R. B. (1998).
889 Interpreting magmatic fabric patterns in plutons. *Lithos, 44*(1–2), 53–82.
890 https://doi.org/10.1016/S0024-4937(98)00022-X

891 Passchier, C. W., & Trouw, R. A. J. (*Eds.*). (2005). Microtectonics. Berlin: Springer

892 Qiu, L., Kong, R., Yan, D. P., Wells, M. L., Wang, A., & Sun, W., et al. (2018). The Zhayao tectonic
893 window of the Jurassic Yuantai thrust system in Liaodong Peninsula, NE China: Geometry,
894 kinematics and tectonic implications. *Journal of Asian Earth Sciences, 164*, 58–71.
895 https://doi.org/10.1016/j.jseaes.2018.06.012

896 Rabillard, A., Arbaret, L., Jolivet, L., Le Breton, N., Gumiaux, C., & Augier, R., et al. (2015).

Interactions between plutonism and detachments during metamorphic core complex formation, Serifos Island (Cyclades, Greece), *Tectonics, 34*, 1080–1106, https://doi.org/10.1002/2014TC003650

Ratschbacher, L., Hacker, B. R., Webb, L. E., McWilliams, M., Ireland, T., & Dong, S., et al. (2000). Exhumation of the ultrahigh-pressure continental crust in east central China: Cretaceous and Cenozoic unroofing and the Tan-Lu fault. *Journal of Geophysical Research: Solid Earth, 105*(B6), 13303–13338. https://doi.org/10.1029/2000jb900040

Ren, J., Tamaki, K., Li, S., & Junxia, Z. (2002). Late Mesozoic and Cenozoic rifting and its dynamic setting in Eastern China and adjacent areas. *Tectonophysics, 344*, 175–205. https://doi.org/10.1016/s0040-1951(01)00271-2

Richard, S. M., Fryxell, J. E., & Sutter, J. F. (1990). Tertiary structure and thermal history of the Harquahala and Buckskin Mountains, west central Arizona: Implications for denudation by a major detachment fault system. *Journal of Geophysical Research, 95*, 19973–19987. http://doi.org/10.1029/JB095iB12p19973.

Roure, F., Choukroune, P., Berastegui, X., Munoz, J. A., Villien, A., & Matheron, P., et al. (1989). ECORS Deep seismic data and balanced cross sections: geometric constraints on the evolution of the Pyrenees. *Tectonics, 8*, 41–50. https://doi.org/10.1029/TC008i001p00041

Schmid, S. M., & Casey, M. (1986). Complete fabric analysis of some commonly observed quartz c-axis patterns. *In* Hobbs, B.E., Heard, H.C. (*Eds.*), Mineral and Rock Deformation: Laboratory Studies (pp. 246–261). American Geophysical Union.

Shen, Y. C., Xie, H. Y., Li, G. M., Liu, T. B., Sun, X. Y., & Wang, Y. J. (1998). Geology and prospecting of the Pengjiakuang gold deposit, Shandong. *Geology and Prospecting, 34*(5), 3–13. (in Chinese with English abstract).

Stipp, M., Stuenitz, H., Heilbronner, R., & Schmid, S. M. (2002). The eastern Tonale fault zone: a natural laboratory for crystal plastic deformation of quartz over a temperature range from 250 to 700°C. *Journal of Structural Geology, 5*, 1–24. https://doi.org/10.1016/S0191-8141(02)00035-4

Tang, H., Zheng, J., Yu, C., Ping, X., & Ren, H. (2014). Multistage crust–mantle interactions during the destruction of the North China Craton: Age and composition of the Early Cretaceous intrusions in the Jiaodong Peninsula. *Lithos, 190–191*, 52–70. https://doi.org/10.1016/j.lithos.2013.12.002

Trindade, R. I. F., Raposo, M. I. B., Ernesto, M., & Siqueira, R. (1999). Magnetic susceptibility and partial anhysteretic remanence anisotropies in the magnetite-bearing granite pluton of Tourão, NE Brazil. *Tectonophysics, 314*(4), 443–468. https://doi.org/10.1016/S0040-1951(99)00220-6

Turrillot, P., Faure, M., Martelet, G., Chen, Y., & Augier, R. (2011). Pluton-dyke relationships in a Variscan granitic complex from AMS and gravity modeling. Inception of the extensional tectonics in the South Armorican Domain (France). *Journal of Structural Geology, 33,* 1681–1698. https://doi.org/10.1016/j.jsg.2011.08.004

Van der Voo, R., Van Hinsbergen, D. J. J., Domeier, M., Spakman, W., & Torsvik, T. H. (2015). Latest Jurassic–earliest Cretaceous closure of the Mongol–Okhotsk Ocean: A paleomagnetic and seismological–tomographic analysis. *Geological Society of America Special Papers, 513*, 589–606. https://doi.org/10.1130/2015.2513(19)

Vernon, R. H. (2000). Review of microstructural evidence of magmatic and solid-state flow. *Electronic Geosciences, 5*, 1–23. https://doi.org/10.1007/s10069-000-0002-3

Vigneresse, J. L. (1990). Use and misuse of geophysical data to determine the shape at depth of granitic intrusions. *Geological Journal, 25*(3–4), 249–260. https://doi.org/10.1002/gj.3350250308

Vigneresse, J. L. (1995). Crustal regime of deformation and ascent of granitic magma. *Tectonophysics, 249*(3-4), 187–202. https://doi.org/10.1016/0040-1951(95)00005-8

943 Vigneresse, J. L., & Bouchez, J. L. (1997). Successive granitic magma batches during pluton
944 emplacement: the case of Cabeza de Araya (Spain). *Journal of Petrology, 38*(12), 1767–1776.
945 https://doi.org/10.1093/petroj/38.12.1767

946 Wallis, S. R., Ishiwatari, A., Hirajima, T., Ye, K., Guo, J., & Nakamura, D., et al. (1997). Occurrence
947 and field relationships of ultrahigh-pressure metagranitoid and coesite eclogite in the Su-Lu
948 terrane, eastern China. *Journal of the Geological Society, 154*(1), 45–54.
949 https://doi.org/10.1144/gsjgs.154.1.0045

950 Wan, Y., Song, B., Liu, D., Wilde, S. A., Wu, J., & Zhou, H. (2006). SHRIMP U–Pb zircon
951 geochronology of Palaeoproterozoic metasedimentary rocks in the North China Craton:
952 evidence for a major Late Palaeoproterozoic tectonothermal event. *Precambrian Research,*
953 *149*(3–4), 249–271. https://doi.org/10.1016/j.precamres.2006.06.006

954 Wang, J., Chang, S.-C., Lu, H.-B., & Zhang, H.-C. (2016). Detrital zircon provenance of the Wangshi
955 and Laiyang groups of the Jiaolai basin: evidence for Early Cretaceous uplift of the Sulu orogen,
956 Eastern China. *International Geology Review, 58*(6), 719–736.
957 https://doi.org/10.1080/00206814.2015.1105728

958 Wang, Q., Ishiwatari, A., Zhao, Z., Hirajima, T., Hiramatsu, N., & Enami, M., et al. (1993).
959 Coesite-bearing granulite retrograded from eclogite in Weihai, Eastern China. *European Journal*
960 *of Mineralogy, 5*(1), 141–152. https://doi.org/10.1127/ejm/5/1/0141

961 Wang, T., Guo, L., Zheng, Y., Donskaya, T., Gladkochub, D., & Zeng, L., et al. (2012). Timing and
962 processes of late Mesozoic mid-lower-crustal extension in continental NE Asia and implications
963 for the tectonic setting of the destruction of the North China Craton: mainly constrained by
964 zircon U–Pb ages from metamorphic core complexes. *Lithos, 154*(6), 315–345.
965 https://doi.org/10.1016/j.lithos.2012.07.020

966 Wei, W., Chen, Y., Faure, M., Shi, Y., Martelet, G., & Hou, Q., et al. (2014a). A multidisciplinary study
967 on the emplacement mechanism of the Qingyang-Jiuhua massif in Southeast China and its
968 tectonic bearings. Part I: Structural geology, AMS and paleomagnetism. *Journal of Asian Earth*
969 *Sciences, 86*, 76–93. https://doi.org/10.1016/j.jseaes.2013.06.003

970 Wei, W., Chen, Y., Faure, M., Martelet, G., Lin, W., & Wang, Q., et al. (2016). An early extensional
971 event of the South China Block during the Late Mesozoic recorded by the emplacement of the
972 Late Jurassic syntectonic Hengshan Composite Granitic Massif (Hunan, SE
973 China). *Tectonophysics*, *672–673*, 50–67. http://dx.doi.org/10.1016/j.tecto.2016.01.028

974 Wei, W., Martelet, G., Le Breton, N., Shi, Y., Faure, M., & Chen, Y., et al. (2014b). A multidisciplinary
975 study of the emplacement mechanism of the Qingyang-Jiuhua massif in Southeast China and its
976 tectonic bearings. Part II: Amphibole geobarometry and gravity modeling. *Journal of Asian*
977 *Earth Sciences, 86*, 94–105. https://doi.org/10.1016/j.jseaes.2013.09.021

978 Wong, W. H. (2009). The Mesozoic Orogenic Movement in Eastern China. *Bulletin of the Geological*
979 *Society of China, 8*(1), 33–44. http://dx.doi.org/10.1111/j.1755-6724.1929.mp8001004.x

980 Wu, F. Y., Yang, J. H., Xu, Y. G., Wilde, S. A., & Walker, R. J. (2019). Destruction of the North China
981 Craton in the Mesozoic. *Annual Review of Earth and Planetary Sciences, 47(1)*, 73–95.
982 https://doi.org/10.1146/annurev-earth-053018-060342

983 Wu, L. (2014). The Mesozoic-Cenozoic thermal evolution of the Sulu Orogenic Belt: Constraints from
984 low-temperature thermochronology, (Doctoral dissertation). Retrieved from Dissertation
985 Knowledge discovery system (http://dpaper.las.ac.cn/Dpaper/homeNew). Institute of Geology
986 and Geophysics, Chinese Academy of Sciences.

987 Wu, L., Monié, P., Wang, F., Lin, W., Ji, W., & Yang, L. (2018). Multi-phase cooling of Early
988 Cretaceous granites on the Jiaodong Peninsula, East China: Evidence from $^{40}Ar/^{39}Ar$ and

(U-Th)/He thermochronology. *Journal of Asian Earth Sciences, 160*, 334–347. https://doi.org/10.1016/j.jseaes.2017.11.014

Xia, Z. M., Liu, J. L., Ni, J. L., Zhang, T. T., Shi, X. M., & Yun, W. (2016). Structure, evolution and regional tectonic implications of the Queshan metamorphic core complex in eastern Jiaodong Peninsula of China. *Science China Earth Sciences, 59*(5), 997–1013. https://doi.org/10.1007/s11430-015-5259-3

Xu, Y. G. (2001). Thermo-tectonic destruction of the Archaean lithospheric keel beneath the Sino-Korean Craton in China: evidence, timing and mechanism. *Physics and Chemistry of the Earth, Part A: Solid Earth and Geodesy, 26*(9–10), 747–757. https://doi.org/10.1016/S1464-1895(01)00124-7

Xu, S. T., Okay. A., Ji, S., Şngör, A. M. C., Su, W., & Liu, Y., et al. (1992). Diamond from Dabie Shan metamorphic rocks and its implication for tectonic setting. *Science, 256*, 80–82. https://doi.org/10.1126/science.256.5053.8

Xue, Z., Martelet, G., Lin, W., Faure, M., Chen, Y., & Wei, W., et al. (2017). Mesozoic crustal thickening of the Longmenshan belt (NE Tibet, China) by imbrication of basement slices: Insights from structural analysis, petrofabric and magnetic fabric studies, and gravity modeling. *Tectonics, 36*, 3110–3134. https://doi.org/10.1002/2017TC004754

Yang, J., Wu, F., Wilde, S., Belousova, E., & Griffin, W. (2008). Mesozoic decratonization of the North China Block. *Geology, 36*(6), 467–470. https://doi.org/10.1130/G24518A.1

Yin, A. (2004). Gneiss domes and gneiss dome systems. *Geological Society of America Special Paper 380*: Gneiss Domes in Orogeny, 1–14. https://doi.org/10.1130/0-8137-2380-9.1

Yin, A. & Nie, S. R. 1996. A Phanerozoic palinspastic reconstruction of China and its neighboring regions. *In*: Yin, A. & Harrison, T. M. (*Eds*), The Tectonic Evolution of Asia (pp. 442–485).

New York: Cambridge University Press.

Yoshinobu, A. S., Okaya, D. A., & Paterson, S. R. (1998). Modelling the thermal evolution of fault-controlled magma emplacement models. *Journal of Structural Geology, 20*, 1205–1218. https://doi.org/10.1016/S0191-8141(98)00064-9

Žák, J., Verner, K., Sláma, J., Kachlík, V., & Chlupáčová, M. (2013). Multistage magma emplacement and progressive strain accumulation in the shallow-level Krkonoše-Jizera plutonic complex, Bohemian massif. *Tectonics, 32*(5), 1493–1512. https://doi.org/10.1002/tect.20088

Žák, J., Verner, K., Tomek, F., Holub, F. V., Johnson, K., & Schwartz, J. J. (2015). Simultaneous batholith emplacement, terrane/continent collision, and oroclinal bending in the Blue Mountains province, North American Cordillera. *Tectonics, 34*(6), 1107–1128.

Zhai, M., Guo, J., & Liu, W. (2005). Neoarchean to Paleoproterozoic continental evolution and tectonic history of the North China Craton: a review. *Journal of Asian Earth Sciences, 24*(5), 547–561. https://doi.org/10.1016/j.jseaes.2004.01.018

Zhai, M. G., Bian, A. G., & Zhao, T. P. (2000). The amalgamation of the supercontinent of North China Craton at the end of Neo-Archaean and its breakup during late Palaeoproterozoic and Mesoproterozoic. *Science in China Series D: Earth Sciences, 43*, 219–232.

Zhang, D. Q., Xu, H. L., & Sun, G, Y. (1995). Emplacement ages of the Denggezuang gold deposit and the Kunyushan granite and their geological implications. *Geological Review, 41*(5), 415–425. https://doi.org/10.16509/j.georeview.1995.05.004 (in Chinese with English abstract).

Zhang, J., Zhao, Z. F., Zheng, Y. F., & Dai, M. (2010). Postcollisional magmatism: Geochemical constraints on the petrogenesis of Mesozoic granitoids in the Sulu orogen, China. *Lithos, 119*(3–4), 512–536. https://doi.org/10.1016/j.lithos.2010.08.005

Zhang, H. Y., Hou, Q. L., & Cao, D. Y. (2007). Study of thrust and nappe tectonics in the eastern

Jiaodong Peninsula, China. *Science China Earth Sciences, 50*(2), 161–171.

Zhang, K., Lü, Q., Yan, J., Hu, H., Fu, G.M., & Shao, L. (2018). Crustal structure beneath the Jiaodong Peninsula, North China, revealed with a 3D inversion model of magnetotelluric data. *Journal of Geophysics and Engineering*, *15*, 2442–2454. https://doi.org/10.1088/1742-2140/aaca5e

Zhang, S. B., Tang, J., & Zheng, Y. F. (2014). Contrasting Lu–Hf isotopes in zircon from Precambrian metamorphic rocks in the Jiaodong Peninsula: constraints on the tectonic suture between North China and South China. *Precambrian Research, 245*(5), 29–50. https://doi.org/10.1016/j.precamres.2014.01.006

Zhang, T., & Zhang, Y. (2007). Geochronological sequence of Mesozoic intrusive magmatism in Jiaodong Peninsula and its tectonic constraints. *Geological Journal of China Universities, 13*(2), 323–336. https://doi.org/10.16108/j.issn1006-7493.2007.02.015 (in Chinese with English abstract).

Zhang, T., & Zhang, Y. (2008). Late Mesozoic tectono-magmatic evolution history of the Jiaobei uplift, Shandong Peninsula. *Acta Geologica Sinica, 82*(9), 1220–1228. (in Chinese with English abstract).

Zhao, L., Zheng, T., Lu, G., & Ai, Y. (2011). No direct correlation of mantle flow beneath the North China Craton to the India-Eurasia collision: Constraints from new SKS wave splitting measurements. *Geophysical Research Letters, 187*, 1027–1037. https://10.1111/j.1365-246X.2011.05201.x

Zhao, G. C., Wilde, S. A., Cawood, P. A., & Lu, L. Z. (1998). Thermal evolution of the Archaean basement rocks from the eastern part of the North China Craton and its bearing on tectonic setting. *International Geology Review, 40*, 706–721.

https://doi.org/10.1080/00206819809465233

Zhao, R., Wang, Q., Liu, X., Wang, W., & Pan, R. (2016). Architecture of the Sulu crustal suture between the North China Craton and Yangtze Craton: constraints from Mesozoic granitoids. *Lithos, 266–267*, 348–361. https://doi.org/10.1016/S0169-1368(97)00022-X

Zhu, G., Chen, Y., Jiang, D., & Lin, S. (2015). Rapid change from compression to extension in the North China Craton during the early Cretaceous: evidence from the Yunmengshan metamorphic core complex. *Tectonophysics, 656*(1), 91–110. https://doi.org/10.1016/j.tecto.2015.06.009

Zhu, G., Jiang, D., Zhang, B., & Chen, Y. (2012). Destruction of the eastern North China Craton in a back-arc setting: evidence from crustal deformation kinematics. *Gondwana Research, 22*(1), 86–103. https://doi.org/10.1016/j.gr.2011.08.005

Zhu, R. X., Chen, L., Wu, F. Y., & Liu, J. L. (2011). Timing, scale and mechanism of the destruction of the North China Craton. *Science China Earth Sciences, 54*, 789–797.

**Figure captions**

**Figure 1.** Tectonic sketch of the northern part of Jiaodong Peninsula (*after* Faure *et al*., 2003a) with the location of the study area. Inserted diagram showing the tectonic position of East China with the multi-plate convergences surrounding it.

**Figure 2.** Simplified geological map of the Queshan-Kunyushan-Yuangezhuang-Sanfoshan (QKYS) massif. Foliations and lineations are based on our field work; they show the domal architecture of the massif. Abbreviations are same as the Figure 1.

**Figure 3.** Geological cross-sections across the QKYS massif (locations are shown in Figure 2). A: Cross-section drawn parallel to the direction of the SW–NE. B and C: WNW–ESE cross-sections parallel to the direction of the ductile deformation in the western margin.

**Figure 4.** Available geochronological data of the QKYS massif. All the data are collected from

previous studies (Legends and abbreviations are the same in Figure 2). A: Zircon U-Pb ages of the Late Mesozoic plutons. B: Density plot of zircon U-Pb ages from the Late Mesozoic plutons showing their peak ages. C: $^{40}Ar/^{39}Ar$ cooling ages of the massif. D: Cooling history of the massif to constrain the timing of polyphase deformation events.

**Figure 5.** Field photographs of the Late Jurassic and Early Cretaceous plutons. A: Late Jurassic Kunyushan undeformed biotite monzogranite (KY20: 37.1109°N, 121.7139°E). B: Late Jurassic Kunyushan foliated biotite monzogranite (18JD59: 37.3275°N, 121.7749°E). C: Late Jurassic Queshan mylonitic granite (QS43: 37.1231°N, 121.3873°E). D: Early Cretaceous undeformed porphyritic biotite monzogranite with large K-feldspar phenocrysts (YG10: 37.2880°N, 121.4306°E).

**Figure 6.** Field structures represented as equal-area lower hemisphere diagrams of the planar and linear structures related to the ductile deformation developed in the QKYS massif.

**Figure 7**. Field and microscope photos of the deformed granite in the northern margin of the K pluton and gneissic country rocks, displaying a top-to-the-NE sense of shear. A: NE–SW mineral lineation marked in the foliated granite by biotite and quartz aggregates (19JD127: 37.3786°N, 121. 7445°E). B: Isoclinal fold with axis plunging to NE developed in the orthogneiss (17JD35: 37.3415°N, 121.7575°E). C: Sigma-type K-feldspar in the foliated granite (19JD127: 37.3786°N, 121. 7445°E). D: Asymmetric felsic boudin within the orthogneiss (17JD35:37.3415°N, 121.7575°E). E: Sigma-type plagioclase porphyroclast and “ribbon-like” quartz grains in the foliated granite (KY57: 37.2789°N, 121.8502°E). F: In the gneiss (17JD35: 37.3415°N, 121.7575°E), quartz and feldspars showing sigma-type features and low-temperature deformation. Symbols: Qz: quartz; Pl: plagioclase; Kfs: K-feldspar; Bi: biotite; Amp: amphibole.

**Figure 8.** Field and microscope photos of the metamorphic rocks from the south of the QKYS massif, all showing a top-to-the-SW shearing. A: ENE–WSW-trending mineral and stretching lineation marked by mineral aggregates in a mylonite (18JD28: 36.8016°N, 121.5354°E). B: Isoclinal fold axes parallel

1105 to a N50° stretching lineation formed by muscovite and feldspar aggregates (18JD29: 36.7503°N,
1106 121.5576°E). C: Asymmetric felsic boudins within the mica schist (18JD29: 36.7503°N, 121.5576°E).
1107 D: Sigma-type feldspar porphyroclasts in the mylonite (18JD28: 36.8016°N, 121.5354°E). E:
1108 Microphotograph of the sigma-type feldspar porphyroclast in a felsic mylonite (18JD13: 36.8309°N,
1109 283 121.4490°E). F: Microphotograph of muscovite "fish" in a mica schist (18JD29: 36.7503°N,
1110 121.5576°E) showing the same asymmetry. Symbols: Qz: quartz; Pl: plagioclase; Mus: muscovite.
1111 **Figure 9.** Field, hand-sample, and microscope photos of the mylonitic Q granite and its country rocks,
1112 showing a top-to-the-WNW shearing. A: WNW–ESE lineation defined by biotite and feldspar
1113 aggregates in the granite (QS29: 37.1317°N, 121. 2507°E). B: Asymmetric and top-to-the-WNW
1114 sheared felsic lenses in the meta-sedimentary rock (QS37: 37.0279°N, 121.3374°E). C: Sigma-type
1115 feldspar porphyroclasts in the granite (QS28: 37.1598°N, 121. 2585°E). D: S-C fabric and sigma-type
1116 feldspar porphyroclasts in the granite (QS43: 37.1231°N, 121.3873°E). E: Thin section: sigma- and
1117 delta-type porphyroclasts in the granite (QS41: 37.0995°N, 121.3943°E). F: Thin section: asymmetric
1118 feldspar porphyroclast surrounded by fine-grained quartz grain in the granite (QS28: 37.1598°N, 121.
1119 331 2585°E). Symbols: Qz: quartz; Pl: plagioclase; Kfs: K-feldspar; Bi: biotite.
1120 **Figure 10.** Typical microphotographs showing the microstructures of the QKYS massif. A: Typical
1121 magmatic fabric with undeformed quartz, plagioclase, biotite, and K-feldspar (SF02: 36.9333°N,
1122 121.6890°E). B: Quartz-veinlet cross-cutting a plagioclase with undulatory extinction, showing that the
1123 deformation ended at relatively low temperature and rather high stress (KY09: 37.2360°N, 121.9220°E).
1124 C: Plagioclase phenocrysts surrounded by “ribbon-like” quartz grains with straight boundaries (KY57:
1125 37.2789°N, 121.8502°E). D: K-feldspar showing the core-mantle structure (KY57: 37.2789°N,
1126 121.8502°E; lower: plane-polarized light; upper: cross-polarized light). E: Low-grade mylonite,
1127 showing the broken K-feldspar with the foliated matrix of tiny recrystallized quartz (18JD13:
1128 36.8309°N, 121.4490°E). E: The quartz grains are recrystallized to form the new grains with irregular

boundaries, showing the shape preferred orientation (QS40: 37.0989°N, 121.3904°E). Symbols: Qz: quartz; Pl: plagioclase; Kfs: K-feldspar; Bi: biotite.

**Figure 11.** Kinematic map for the tectonic events in the QKYS massif and quartz LPO diagrams obtained by universal stage measurement (Captions are the same as in Figure 2). Arrows point to the sense of shear of the upper layer over the lower layer. Samples are foliated or mylonitic monzogranite (KY05, KY09, KY57, QS27, QS30, QS43, 18JD125), mylonitic gneiss (17JD35, 18JD13, 18JD18 and 18JD28) and mica schist (QS37 and 18JD29). Equal-area lower hemisphere diagrams drawn in the XZ section of the bulk strain ellipsoid (*i.e.*, perpendicular to foliation and parallel to the mineral and stretching lineation). Contour intervals given as multiple of random distribution are shown for each sample.

**Figure 12.** Frequency histograms of $K_m$ for all the AMS sites.

**Figure 13.** Magnetic mineralogy investigation concerning granite plutons in the QKYS massif. A–C: Thermomagnetic curves. D–F: Acquisition of isothermal remanent magnetization.

**Figure 14.** $M_{rs}/M_s$ versus $H_{cr}/H_c$ diagram defining the grain size of magnetite. $M_{rs}$: remanence of saturation magnetization after removing the applied field; $M_s$: saturation magnetization under applied field; $H_{cr}$: coercivity of remanence after removing the applied field; $H_c$: coercivity under applied field. SD: single domain; PSD: pseudo single domain; MD: multi-domain.

**Figure 15.** AMS scalar parameters for the analyzed plutons. A: Distribution of $P_j$ within each pluton (Captions are the same as in Figure 2, and the offset of Zhuwu Fault is restored). B: Distribution of $T$ within each pluton. C: $P_j$ versus $K_m$ diagram showing the absence of correlation between them. D: $T$ versus $K_m$ diagram showing the absence of correlation between them. E–K: $T$ versus $P_j$ diagrams of each region of these four plutons. $T$: shape factor; $P_j$: anisotropy degree; $K_m$: mean bulk magnetic susceptibility in $10^{-3}$ SI.

**Figure 16.** Lower hemisphere equal-area projections of AMS axes for each pluton, with confidence

ellipses at 95%. A: Kunyushan pluton (K); B: Queshan pluton (Q); C: Yuangezhuang pluton (Y) and D: Sanfoshan pluton (S). Small symbols represent each individual specimen and large ones represent the tensorial mean out of 5–8 specimens.

**Figure 17.** Magnetic fabric maps of the Late Mesozoic plutons in the QKYS massif, showing the magnetic foliations/lineations and corresponding orientation diagrams (of their poles) in each region. All orientation diagrams are lower hemisphere, equal-area projections.

**Figure 18.** Residual Bouguer gravity map of the Jiaodong Peninsula obtained by subtraction of a 150 km wavelength regional trend from the original Bouguer gravity map. The red rectangles represent possible feeder zones of Late Jurassic plutons, and they show a rough NW–SE-trending when aligning them.

**Figure 19.** Forward gravity modeling across the QKYS massif revealing its geometry at depth. Along NE–SW profiles (A–E), and NW–SE profiles (F–K). The profiles are in Figure 18.

**Figure 20.** Block diagram showing the bulk geometry, kinematics of the QKYS massif and illustrating the polyphase deformation ($D_1$, $D_2$ and $D_3$) and magmatism ($Mag_1$ and $Mag_2$).

**Figure 21.** A possible tectonic scenario implied from the QKYS massif, pointing to episodic extension and compression tectonics. In these diagrams, we considered the emplacement depth of Late Mesozoic plutons (Dou et al., 2018) as the reference to describe the emplacement-exhumation process of the massif from deep to shallower crustal level. A (165–153 Ma): Emplacement of Late Jurassic plutons ($Mag_1$) at a NE–SW extensional setting, coeval with a high- to low-temperature top-to-the-NE shearing ($D_1$); B (153–135 Ma): NE–SW compressional deformation with low-temperature top-to-the-SW sense of shear ($D_2$); C (130–115 Ma): WNW–ESE regional extension tectonics corresponding to the low-temperature top-to-the-WNW shearing ($D_3$) and leading the QKYS massif exhumed; D (post-115 Ma): Emplacement of Early Cretaceous plutons ($Mag_2$) via the opened fractures and subsequent erosion.

**Figure 22.** East China surrounded by multi-plate convergences during Late Mesozoic (modified after Ji *et al*., 2018b and Lin & Wei, 2018). The subduction direction of the Izanagi Plate is based on Maruyama *et al*. (1997). Late Mesozoic extensional and compressional structures are marked to show their spatial and temporal distribution. NCC: North China Craton; SCB: South China Block; CAOB: Central Asian orogenic belt; YS–YS: Yinshan–Yanshan fold and thrust belt; JD: Jiaodong Peninsula; TLF: Tan–Lu fault; THS: Taihangshan; Gbk: Gubeikou fault; Sht: Sihetang ductile shear zone; Yw: Yiwulüshan massif; LY–QL: Lingyuan–Qinglong area; LD: Liaodong Peninsula.

**Figure 1.**

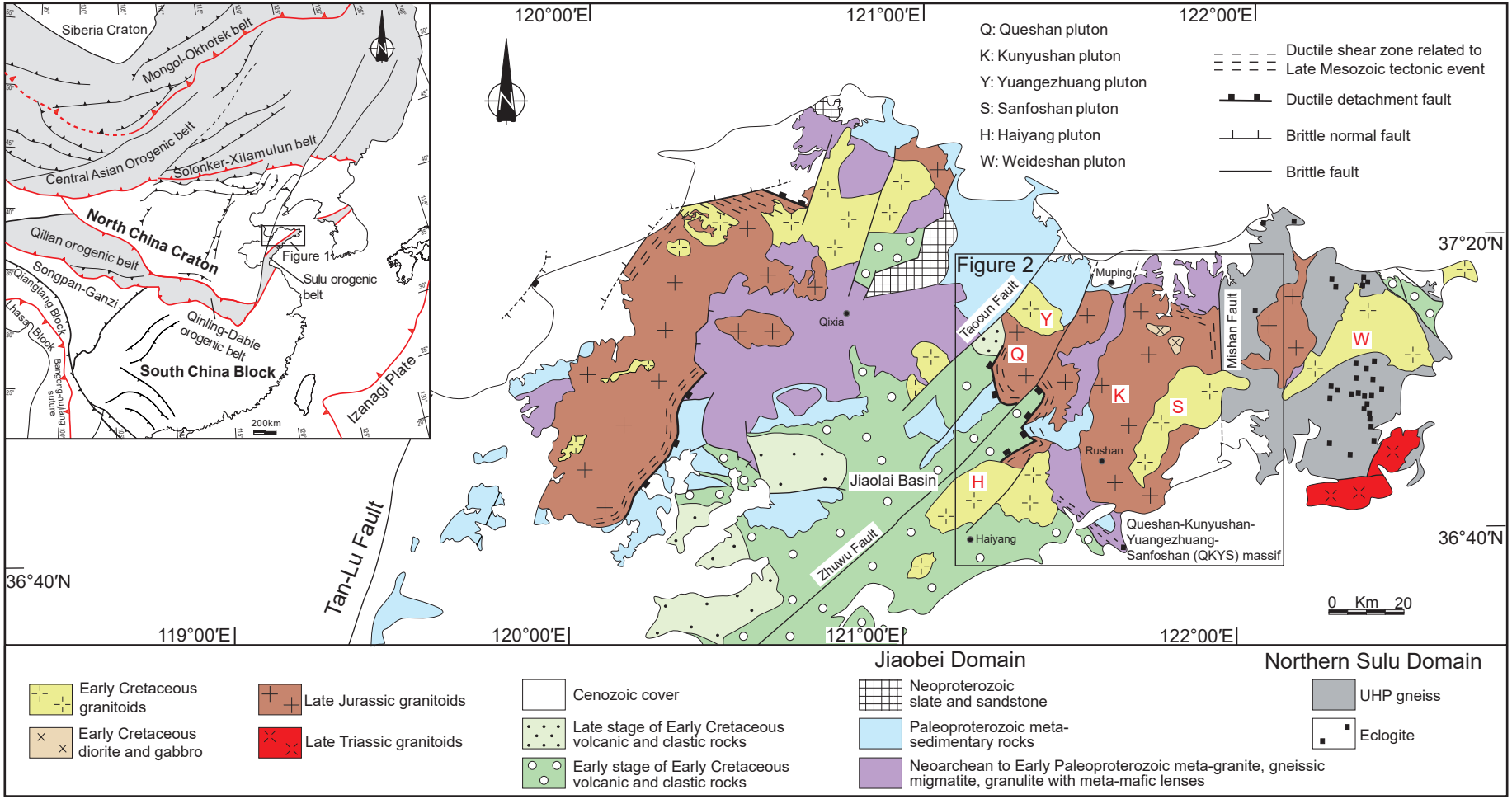
Siberia Craton
Mongol-Okhotsk belt
Central Asian Orogenic belt
Solonker-Xilamulun belt
North China Craton
Qilian orogenic belt
Songpan-Ganzi
Qiangtang Block
Lhasa Block
Bangongnuiuling suture
Qinling-Dabie orogenic belt
South China Block
Sulu orogenic belt
Izanagi Plate
Figure 1
200km
120°00′E
121°00′E
122°00′E
37°20′N
36°40′N
119°00′E
Q: Queshan pluton
K: Kunyushan pluton
Y: Yuangezhuang pluton
S: Sanfoshan pluton
H: Haiyang pluton
W: Weideshan pluton
Ductile shear zone related to Late Mesozoic tectonic event
Ductile detachment fault
Brittle normal fault
Brittle fault
Figure 2
Muping
Qixia
Taocun Fault
Mishan Fault
Rushan
Haiyang
Jiaolai Basin
Zhuwu Fault
Tan-Lu Fault
Queshan-Kunyushan-Yuangezhuang-Sanfoshan (QKYS) massif
0 Km 20
Jiaobei Domain
Northern Sulu Domain
Early Cretaceous granitoids
Early Cretaceous diorite and gabbro
Late Jurassic granitoids
Late Triassic granitoids
Cenozoic cover
Late stage of Early Cretaceous volcanic and clastic rocks
Early stage of Early Cretaceous volcanic and clastic rocks
Neoproterozoic slate and sandstone
Paleoproterozoic meta-sedimentary rocks
Neoarchean to Early Paleoproterozoic meta-granite, gneissic migmatite, granulite with meta-mafic lenses
UHP gneiss
Eclogite

**Figure 2.**

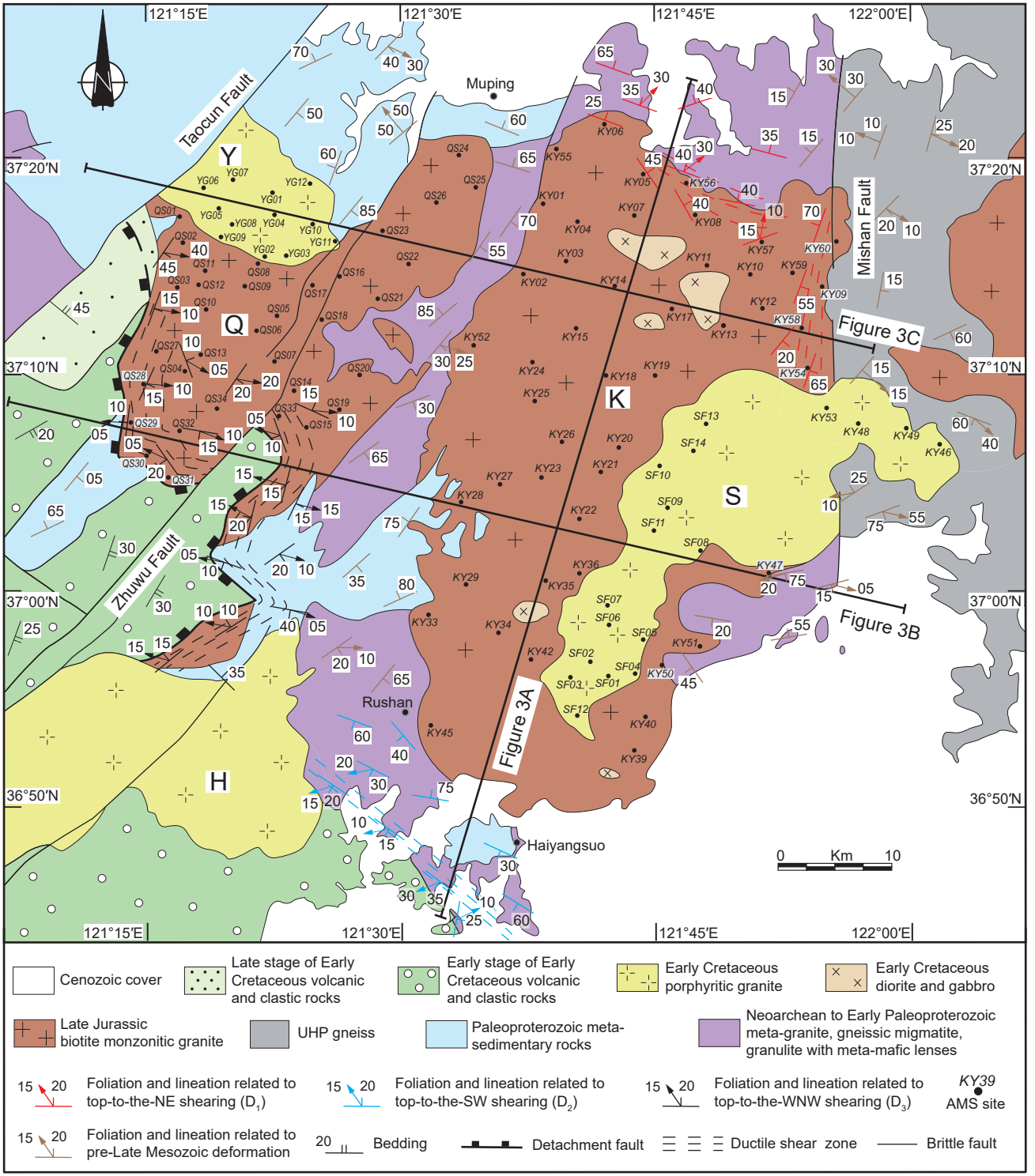
121°15′E
121°30′E
121°45′E
122°00′E
37°20′N
37°10′N
37°00′N
36°50′N
Taocun Fault
Zhuwu Fault
Mishan Fault
Muping
Rushan
Haiyangsuo
Figure 3A
Figure 3B
Figure 3C
Y
Q
K
S
H
0 Km 10
Cenozoic cover
Late stage of Early Cretaceous volcanic and clastic rocks
Early stage of Early Cretaceous volcanic and clastic rocks
Early Cretaceous porphyritic granite
Early Cretaceous diorite and gabbro
Late Jurassic biotite monzonitic granite
UHP gneiss
Paleoproterozoic meta-sedimentary rocks
Neoarchean to Early Paleoproterozoic meta-granite, gneissic migmatite, granulite with meta-mafic lenses
Foliation and lineation related to top-to-the-NE shearing (D1)
Foliation and lineation related to top-to-the-SW shearing (D2)
Foliation and lineation related to top-to-the-WNW shearing (D3)
KY39 AMS site
Foliation and lineation related to pre-Late Mesozoic deformation
Bedding
Detachment fault
Ductile shear zone
Brittle fault

**Figure 3.**

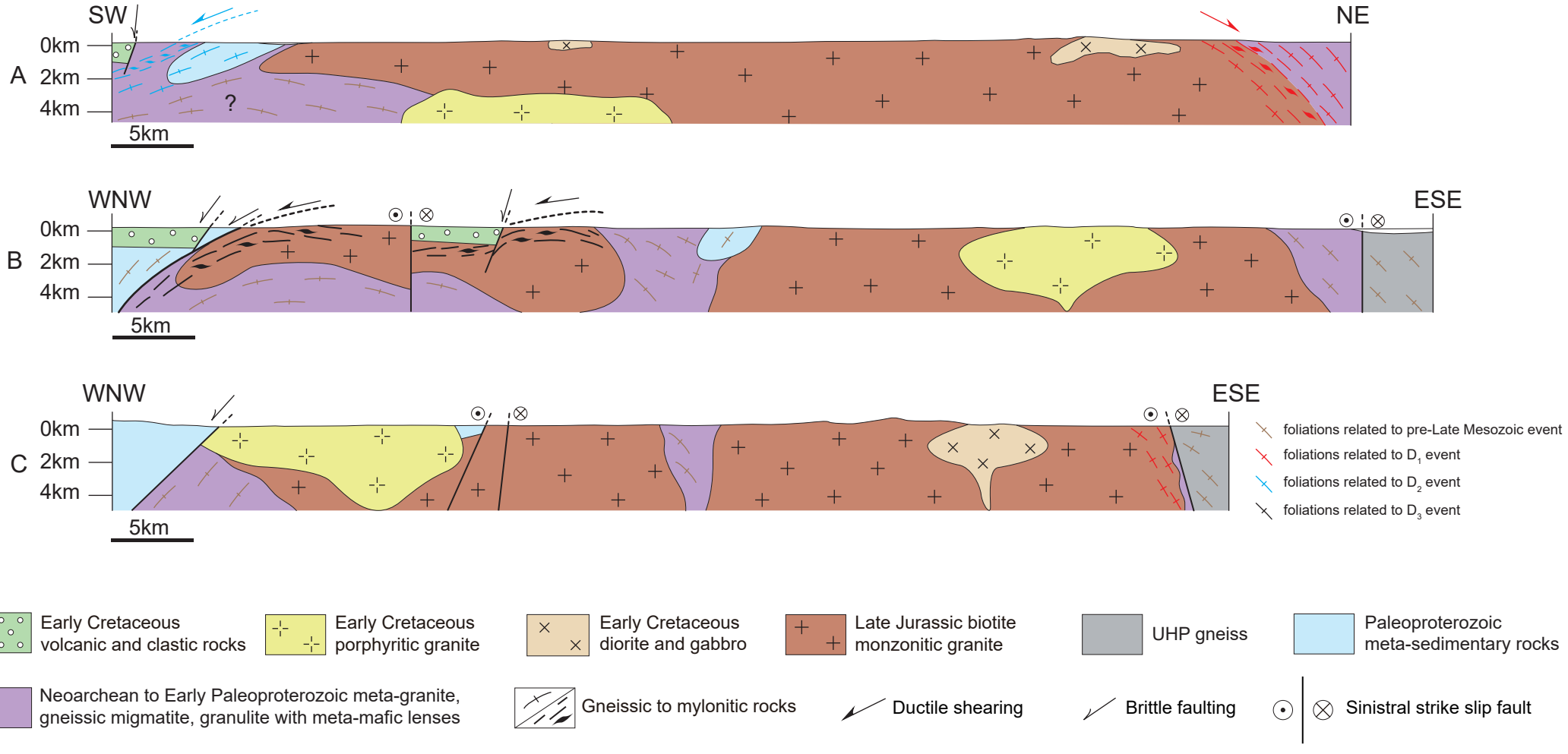
A
SW
NE
0km
2km
4km
?
5km
B
WNW
ESE
0km
2km
4km
5km
C
WNW
ESE
0km
2km
4km
5km
foliations related to pre-Late Mesozoic event
foliations related to D1 event
foliations related to D2 event
foliations related to D3 event
Early Cretaceous volcanic and clastic rocks
Early Cretaceous porphyritic granite
Early Cretaceous diorite and gabbro
Late Jurassic biotite monzonitic granite
UHP gneiss
Paleoproterozoic meta-sedimentary rocks
Neoarchean to Early Paleoproterozoic meta-granite, gneissic migmatite, granulite with meta-mafic lenses
Gneissic to mylonitic rocks
Ductile shearing
Brittle faulting
Sinistral strike slip fault

**Figure 4.**

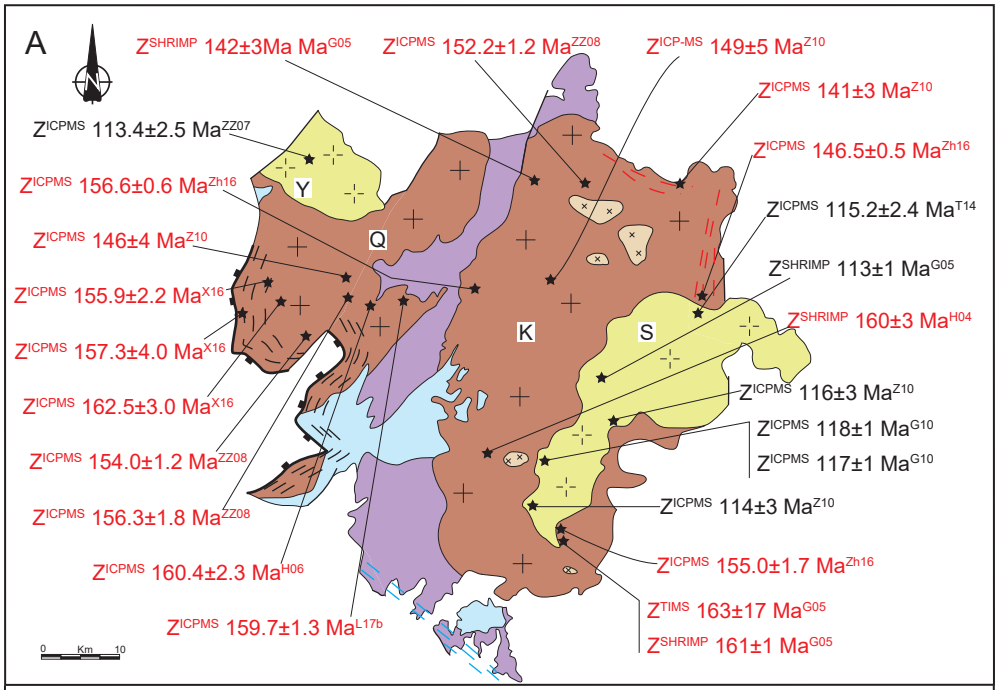


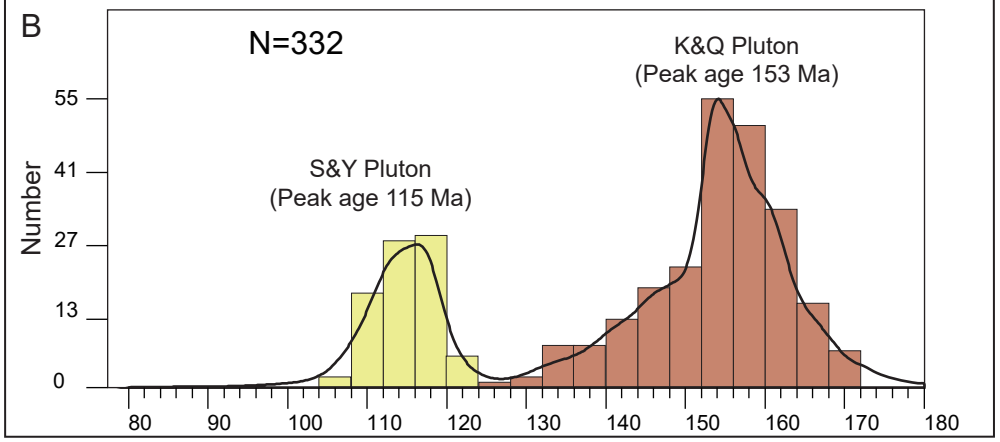


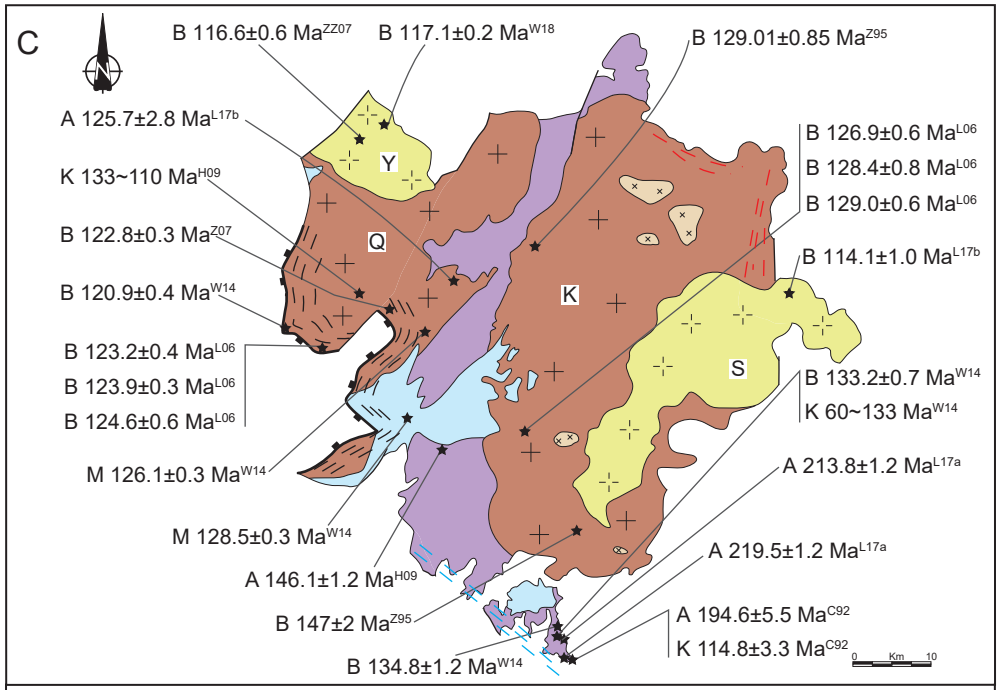


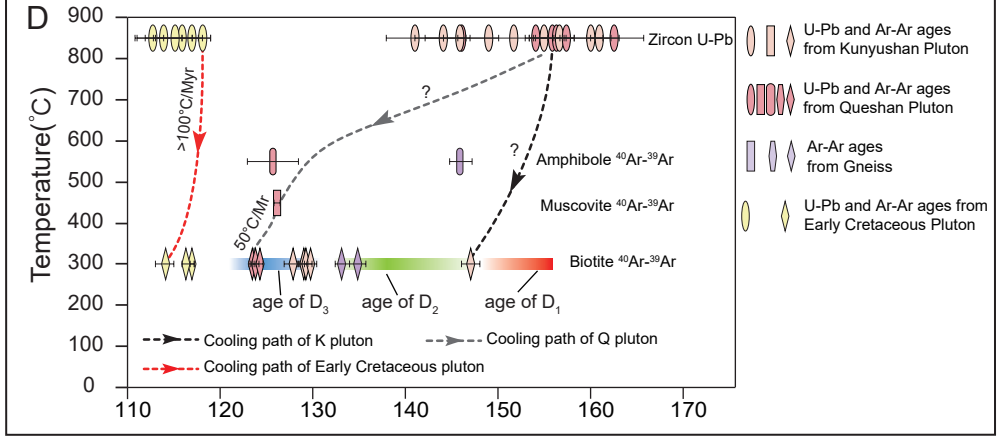


Z: zircon U-Pb
A: amphibole $^{40}Ar/^{39}Ar$
M: muscovite $^{40}Ar/^{39}Ar$
B: biotite $^{40}Ar/^{39}Ar$
K: K-feldspar $^{40}Ar/^{39}Ar$

Z^ICPMS 114±3 Ma^Z10 (Method / Reference / Location / Age)

## Data source

Chen et al., 1992: C92
Goss et al., 2009: G10
Guo et al., 2005: G05
Hacker et al., 2006: H06
Hacker et al., 2009: H09
Hu et al., 2004: H04
Li et al., 2006: L06
Liu et al., 2017a: L17a
Liu et al., 2017b: L17b
Tang et al., 2014: T14
Wu, 2014: W14
Wu et al., 2018: W18
Xia et al., 2016: X16
Zhang et al., 1995: Z95
Zhang&Zhang, 2007: ZZ07
Zhang&Zhang, 2008: ZZ08
Zhang et al., 2007: Z07
Zhang et al., 2010: Z10
Zhao et al., 2016: Zh16

**Figure 6.**

A: Orthogneiss distributed between Q and K plutons

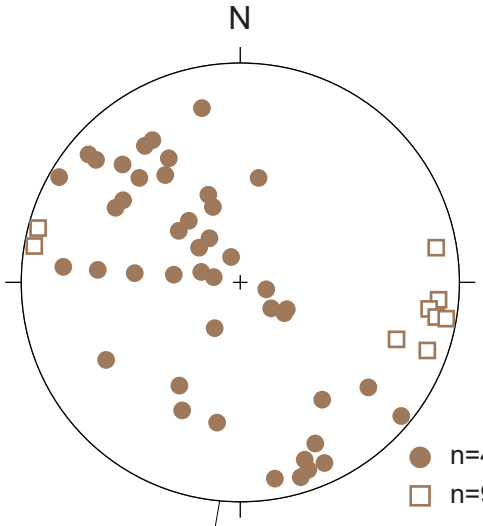


E: Mylonite along the western margin of the QKYS massif

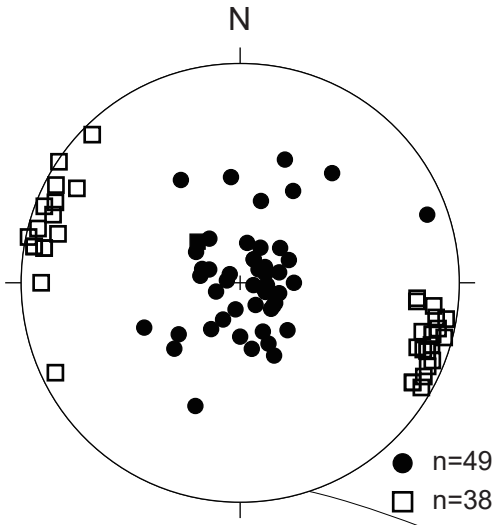


B: Deformed granite in the N-margin of the K pluton

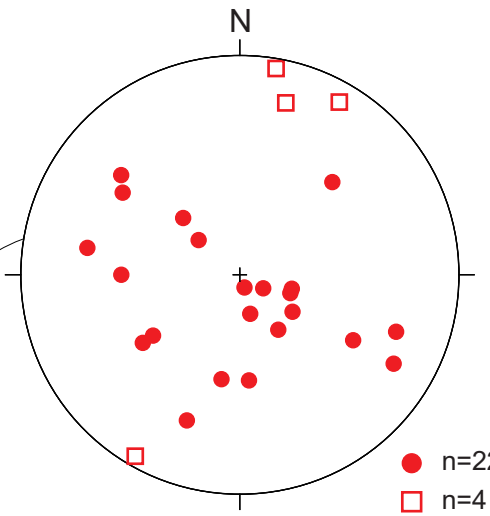


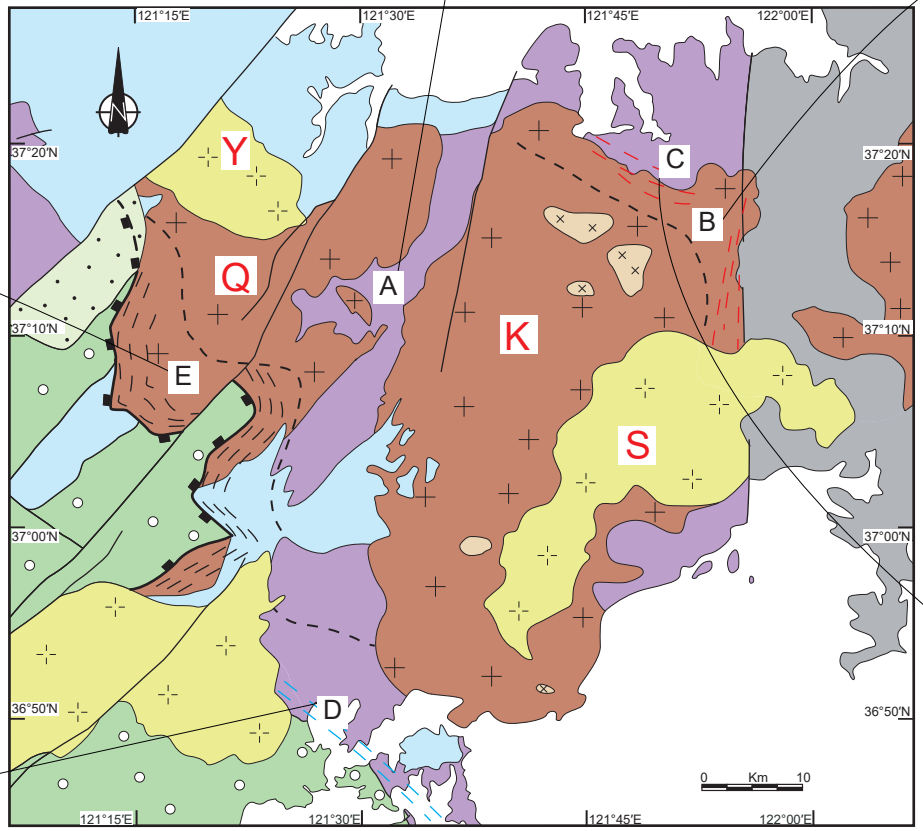


D: Gneissic country rocks at the south of the K pluton

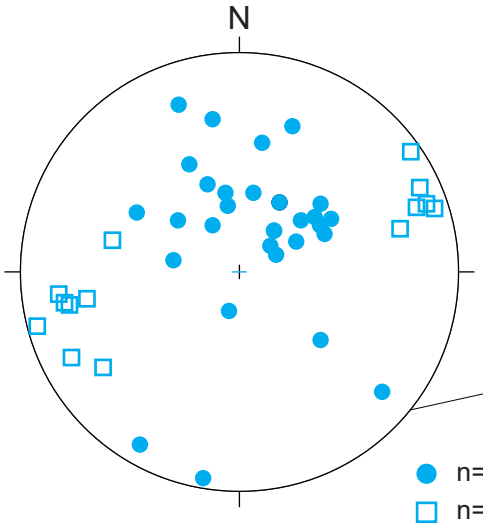


C: Well deformed country orthogneiss at the north of the K pluton

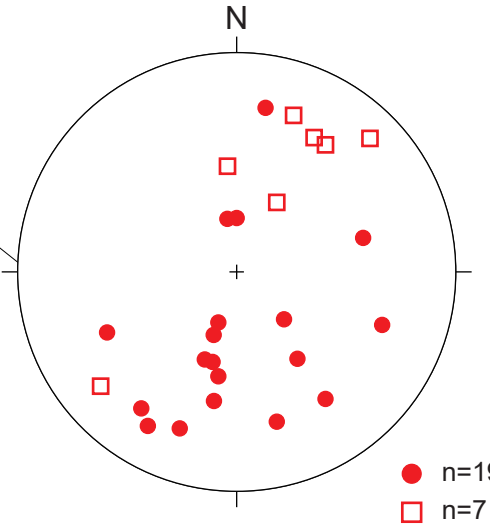

**Figure 5.**

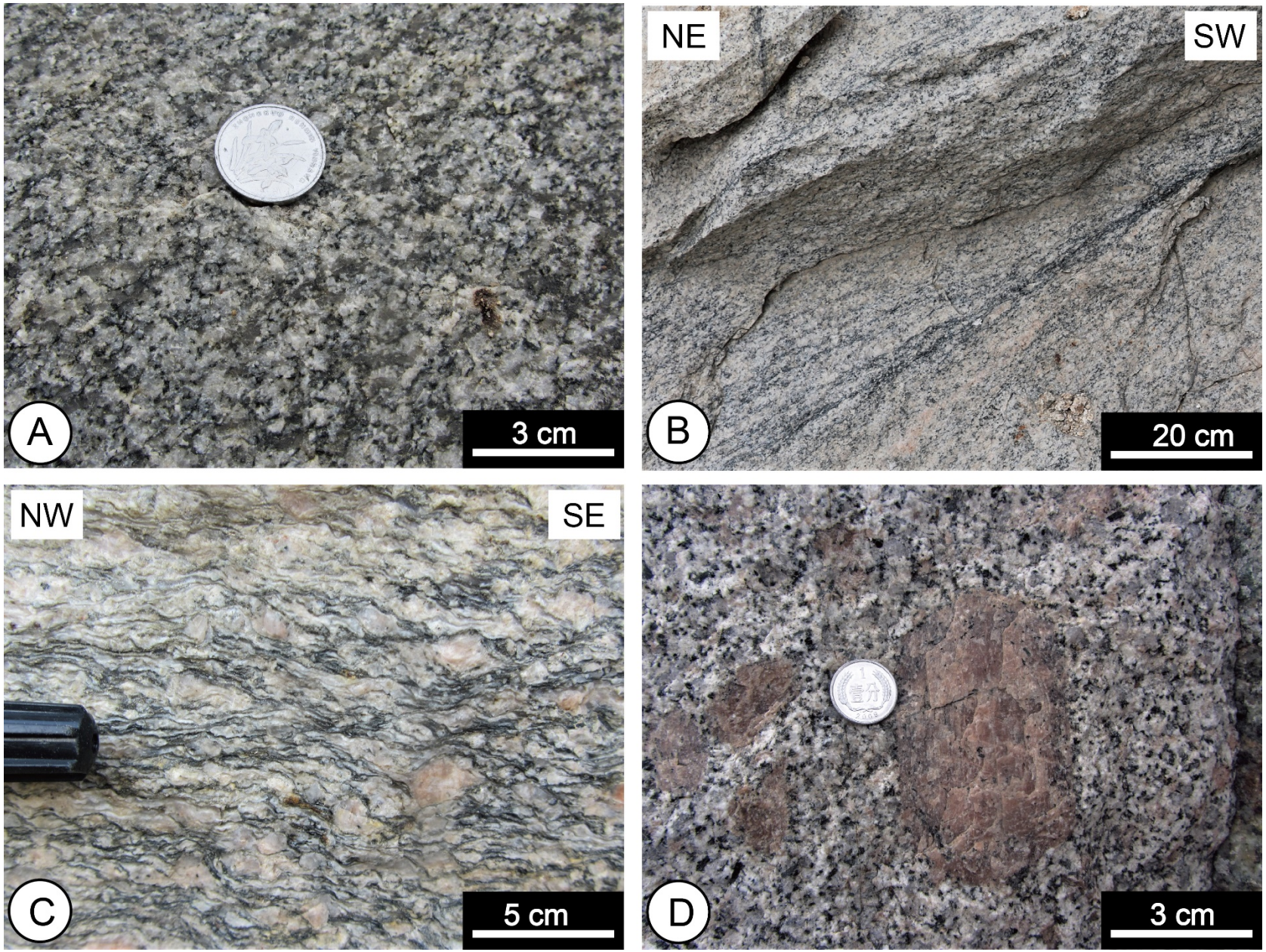
A
3 cm
NE
SW
B
20 cm
NW
SE
C
5 cm
D
3 cm

**Figure 7.**

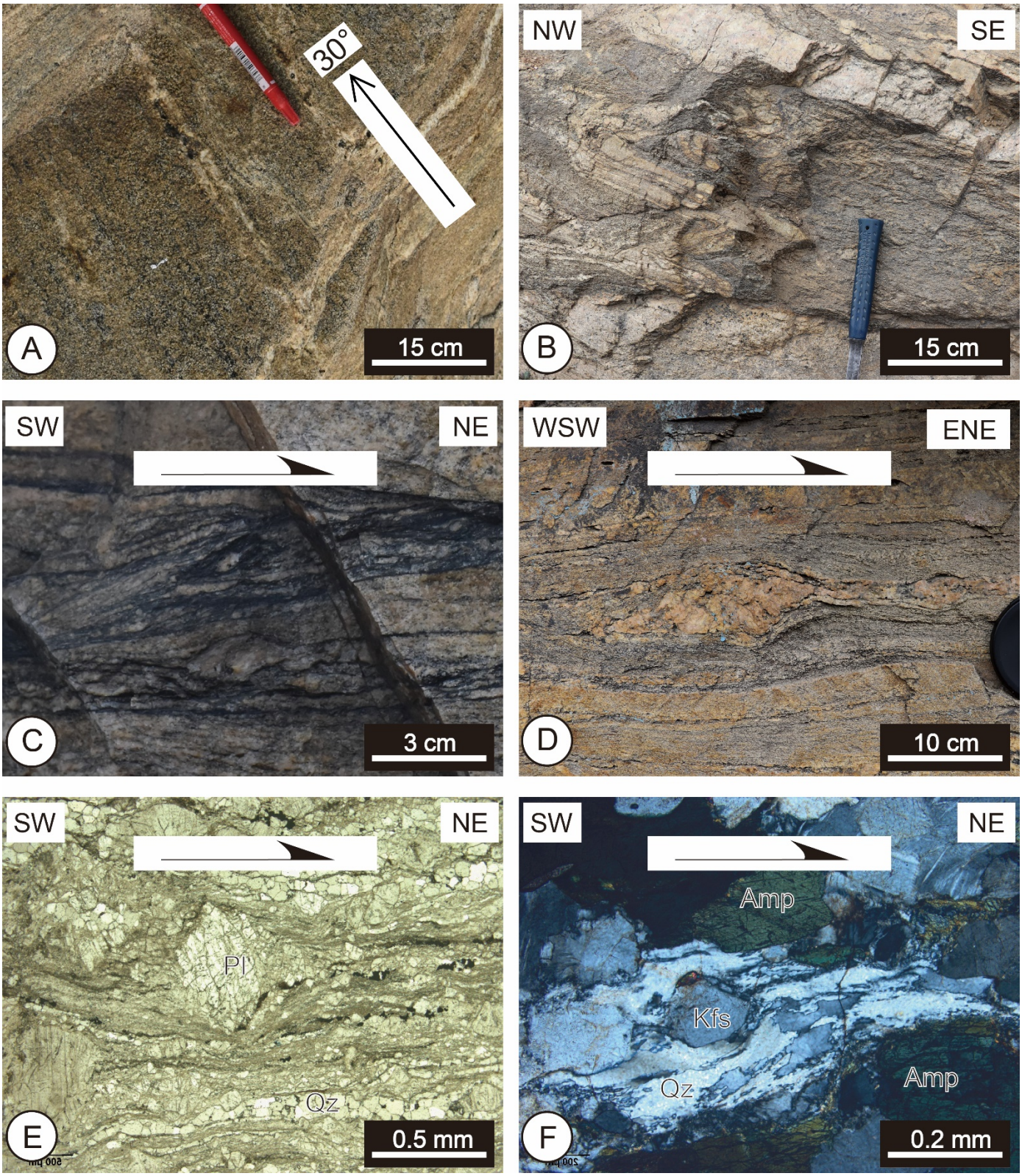
30°
A
15 cm
NW
SE
B
15 cm
SW
NE
C
3 cm
WSW
ENE
D
10 cm
SW
NE
Pl
Qz
E
0.5 mm
SW
NE
Amp
Kfs
Qz
Amp
F
0.2 mm

**Figure 8.**


70°
A
20 cm

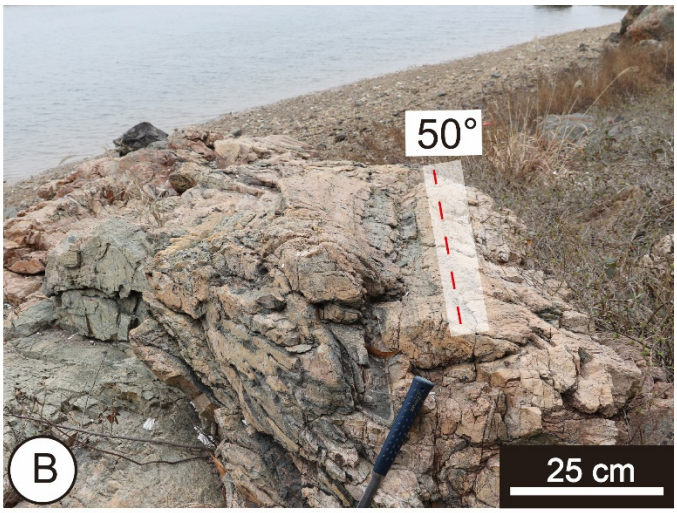
50°
B
25 cm

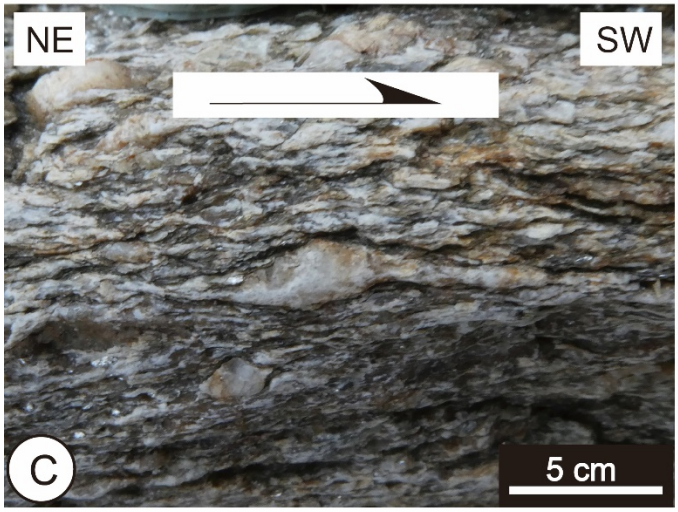
NE
SW
C
5 cm

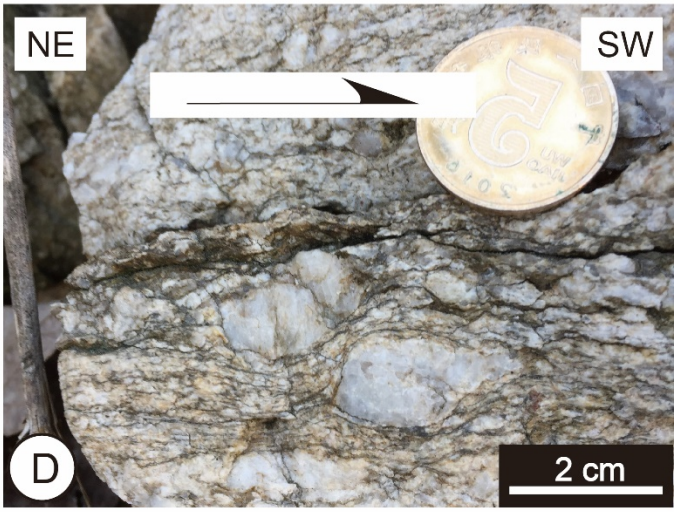
NE
SW
D
2 cm

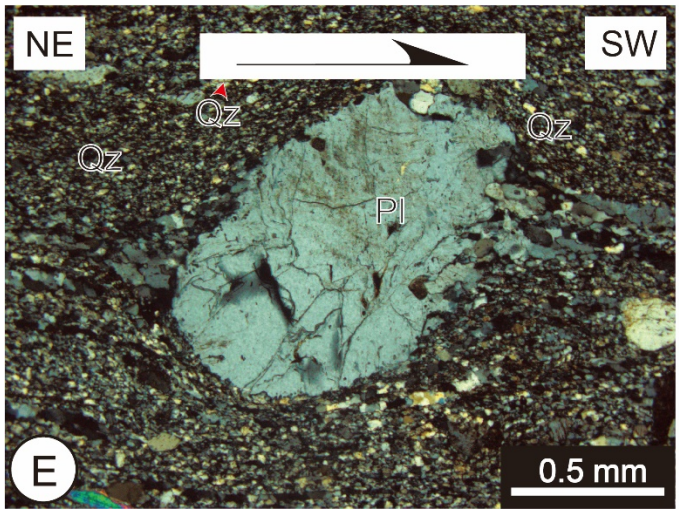
NE
SW
Qz
Qz
Qz
Pl
E
0.5 mm

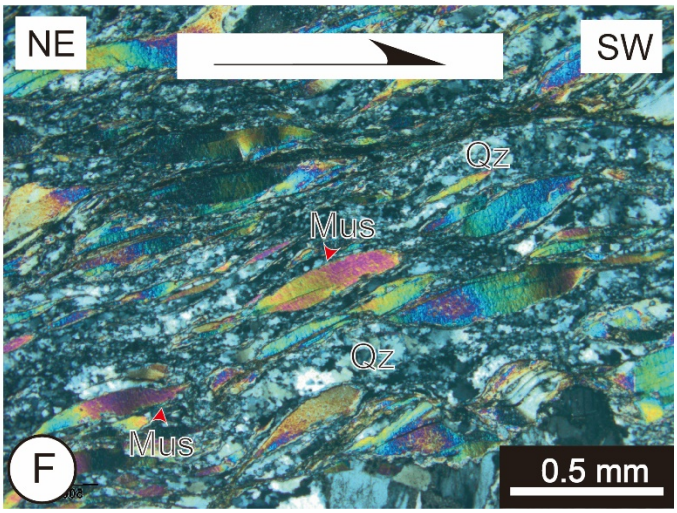
NE
SW
Qz
Mus
Qz
Mus
F
0.5 mm

**Figure 9.**

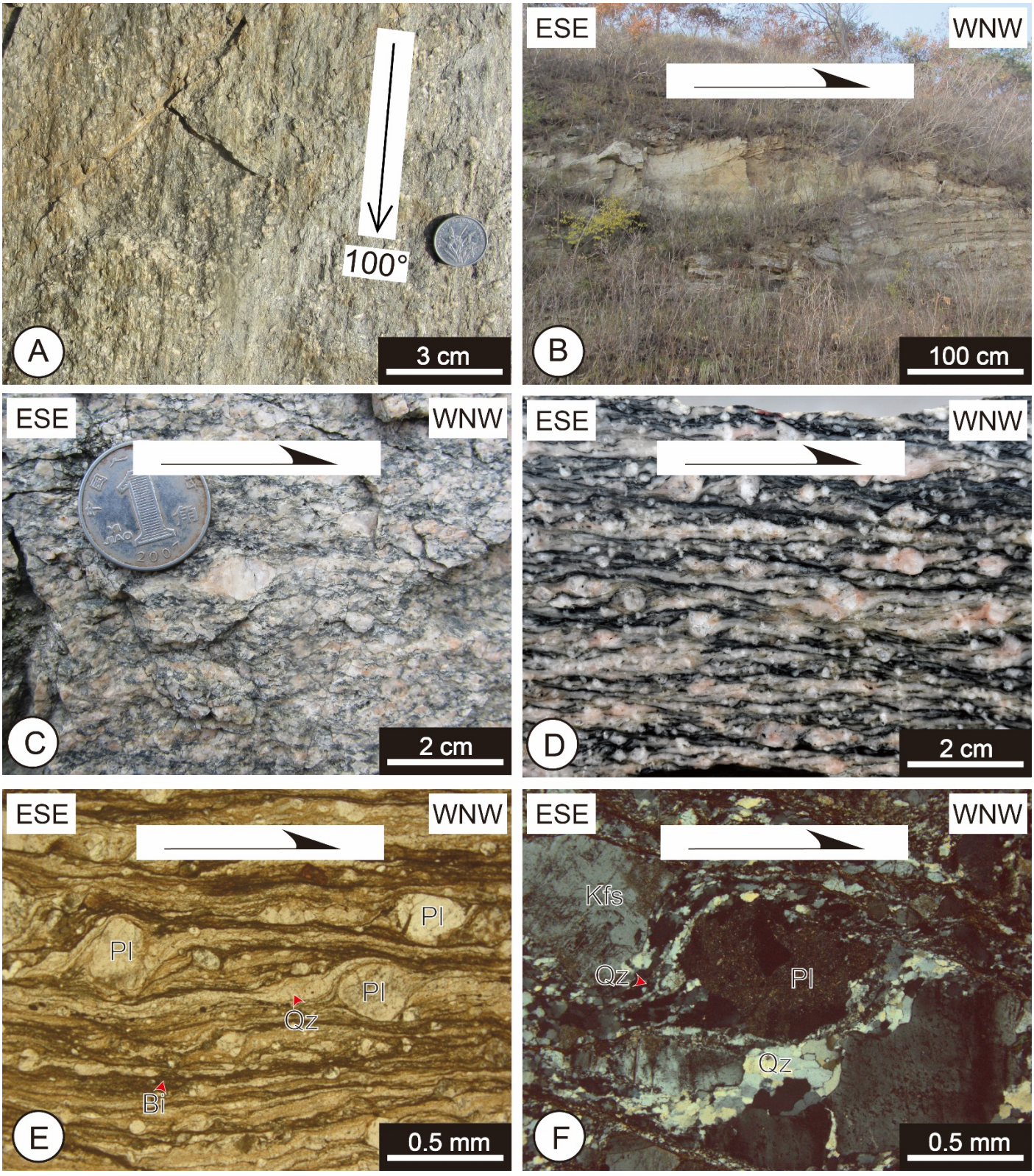
100°
3 cm
A
ESE
WNW
100 cm
B
ESE
WNW
2 cm
C
ESE
WNW
2 cm
D
ESE
WNW
Pl
Pl
Pl
Qz
Bi
0.5 mm
E
ESE
WNW
Kfs
Qz
Pl
Qz
0.5 mm
F

**Figure 10.**

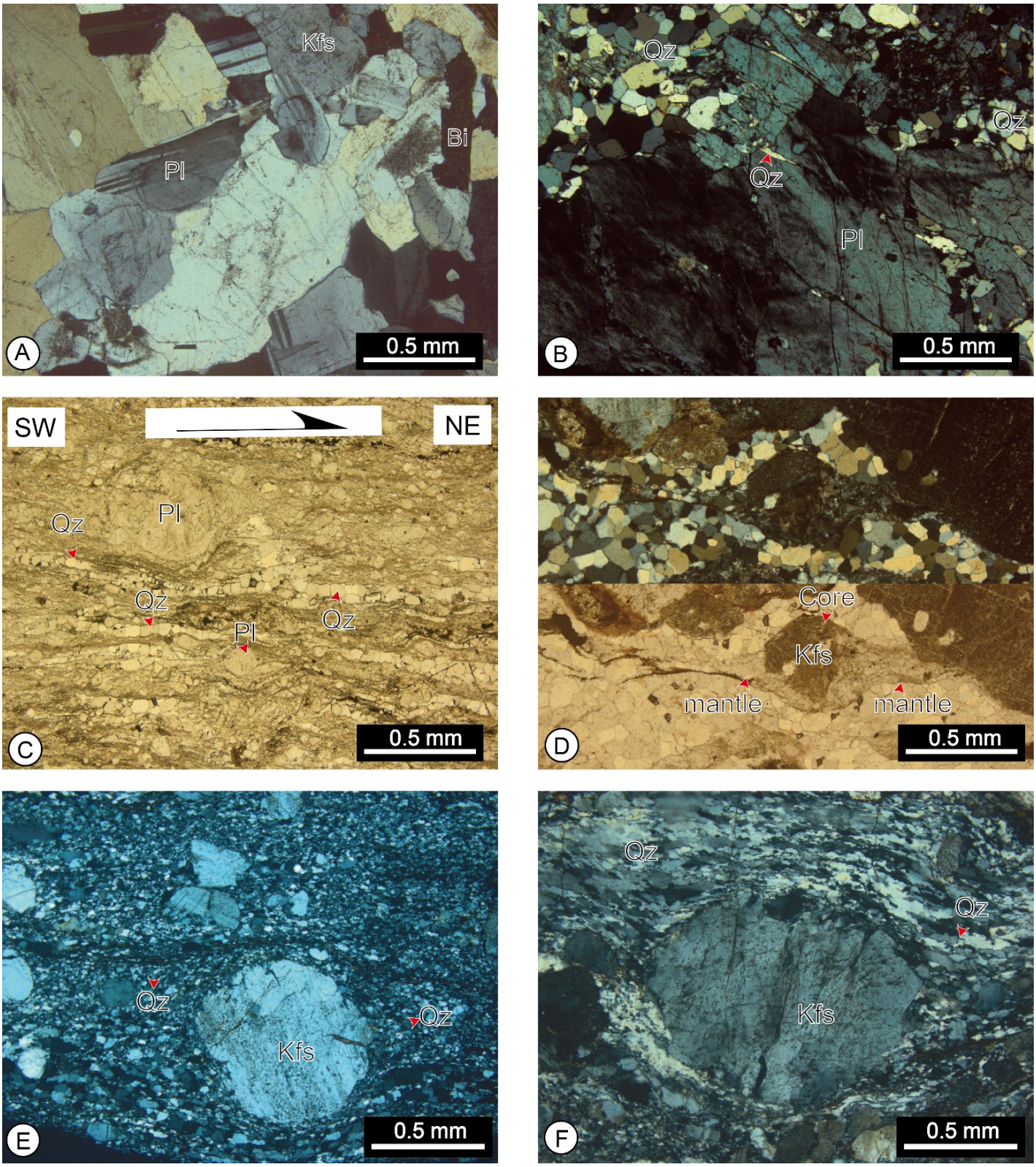
Kfs
Bi
Pl
0.5 mm
A
Qz
Qz
Qz
Pl
0.5 mm
B
SW
NE
Qz
Pl
Qz
Pl
Qz
0.5 mm
C
Core
Kfs
mantle
mantle
0.5 mm
D
Qz
Qz
Kfs
Qz
0.5 mm
E
Qz
Qz
Kfs
0.5 mm
F

**Figure 11.**

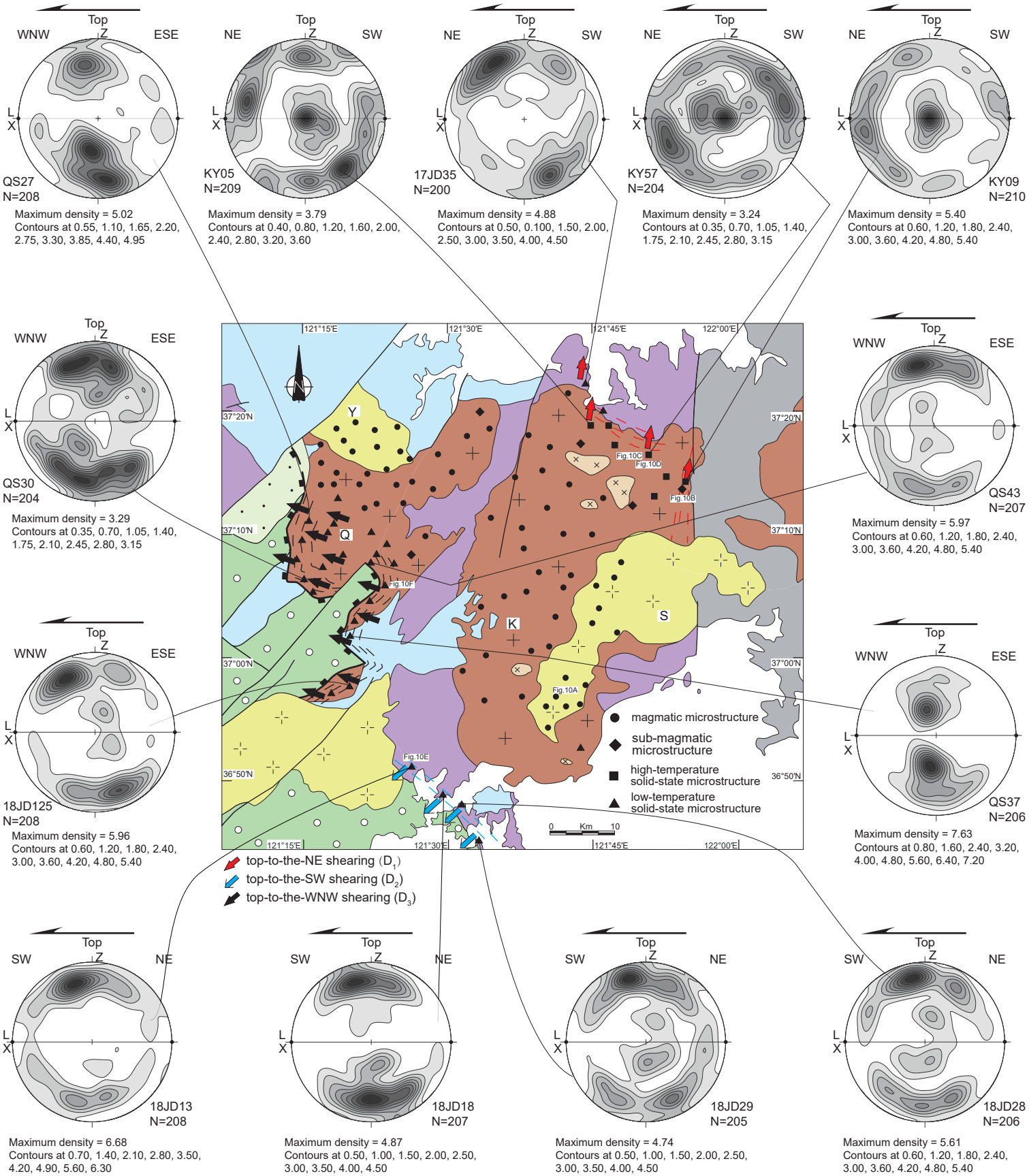
Top
WNW
ESE
Z
L
X
QS27
N=208
Maximum density = 5.02
Contours at 0.55, 1.10, 1.65, 2.20, 2.75, 3.30, 3.85, 4.40, 4.95
NE
SW
KY05
N=209
Maximum density = 3.79
Contours at 0.40, 0.80, 1.20, 1.60, 2.00, 2.40, 2.80, 3.20, 3.60
17JD35
N=200
Maximum density = 4.88
Contours at 0.50, 0.100, 1.50, 2.00, 2.50, 3.00, 3.50, 4.00, 4.50
KY57
N=204
Maximum density = 3.24
Contours at 0.35, 0.70, 1.05, 1.40, 1.75, 2.10, 2.45, 2.80, 3.15
KY09
N=210
Maximum density = 5.40
Contours at 0.60, 1.20, 1.80, 2.40, 3.00, 3.60, 4.20, 4.80, 5.40
QS30
N=204
Maximum density = 3.29
Contours at 0.35, 0.70, 1.05, 1.40, 1.75, 2.10, 2.45, 2.80, 3.15
QS43
N=207
Maximum density = 5.97
Contours at 0.60, 1.20, 1.80, 2.40, 3.00, 3.60, 4.20, 4.80, 5.40
18JD125
N=208
Maximum density = 5.96
Contours at 0.60, 1.20, 1.80, 2.40, 3.00, 3.60, 4.20, 4.80, 5.40
QS37
N=206
Maximum density = 7.63
Contours at 0.80, 1.60, 2.40, 3.20, 4.00, 4.80, 5.60, 6.40, 7.20
18JD13
N=208
Maximum density = 6.68
Contours at 0.70, 1.40, 2.10, 2.80, 3.50, 4.20, 4.90, 5.60, 6.30
18JD18
N=207
Maximum density = 4.87
Contours at 0.50, 1.00, 1.50, 2.00, 2.50, 3.00, 3.50, 4.00, 4.50
18JD29
N=205
Maximum density = 4.74
Contours at 0.50, 1.00, 1.50, 2.00, 2.50, 3.00, 3.50, 4.00, 4.50
18JD28
N=206
Maximum density = 5.61
Contours at 0.60, 1.20, 1.80, 2.40, 3.00, 3.60, 4.20, 4.80, 5.40
121°15'E
121°30'E
121°45'E
122°00'E
37°20'N
37°10'N
37°00'N
36°50'N
N
Y
Q
K
S
Fig.10A
Fig.10B
Fig.10C
Fig.10D
Fig.10E
Fig.10F
magmatic microstructure
sub-magmatic microstructure
high-temperature solid-state microstructure
low-temperature solid-state microstructure
0 Km 10
top-to-the-NE shearing (D1)
top-to-the-SW shearing (D2)
top-to-the-WNW shearing (D3)

**Figure 12.**

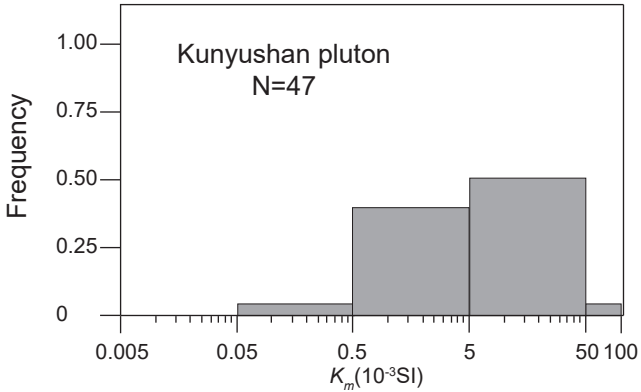
Kunyushan pluton
N=47
Frequency
1.00
0.75
0.50
0.25
0
0.005
0.05
0.5
5
50 100
$K_m$(10$^{-3}$SI)

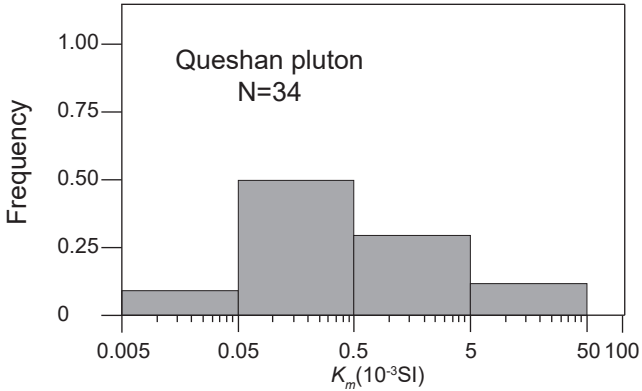
Queshan pluton
N=34
Frequency
1.00
0.75
0.50
0.25
0
0.005
0.05
0.5
5
50 100
$K_m$(10$^{-3}$SI)

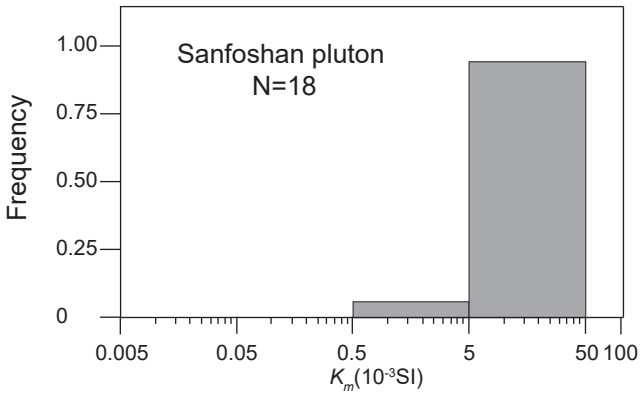
Sanfoshan pluton
N=18
Frequency
1.00
0.75
0.50
0.25
0
0.005
0.05
0.5
5
50 100
$K_m$(10$^{-3}$SI)

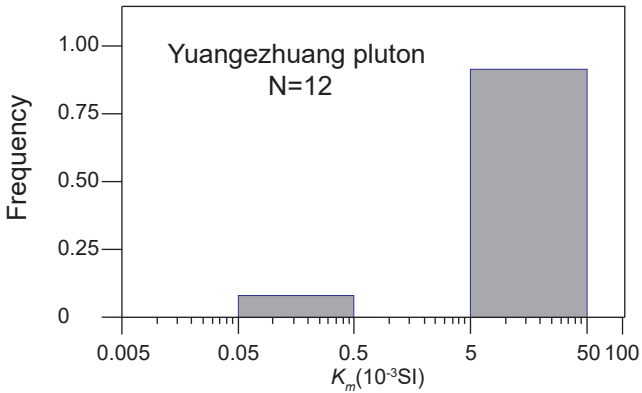
Yuangezhuang pluton
N=12
Frequency
1.00
0.75
0.50
0.25
0
0.005
0.05
0.5
5
50 100
$K_m$(10$^{-3}$SI)

**Figure 13.**

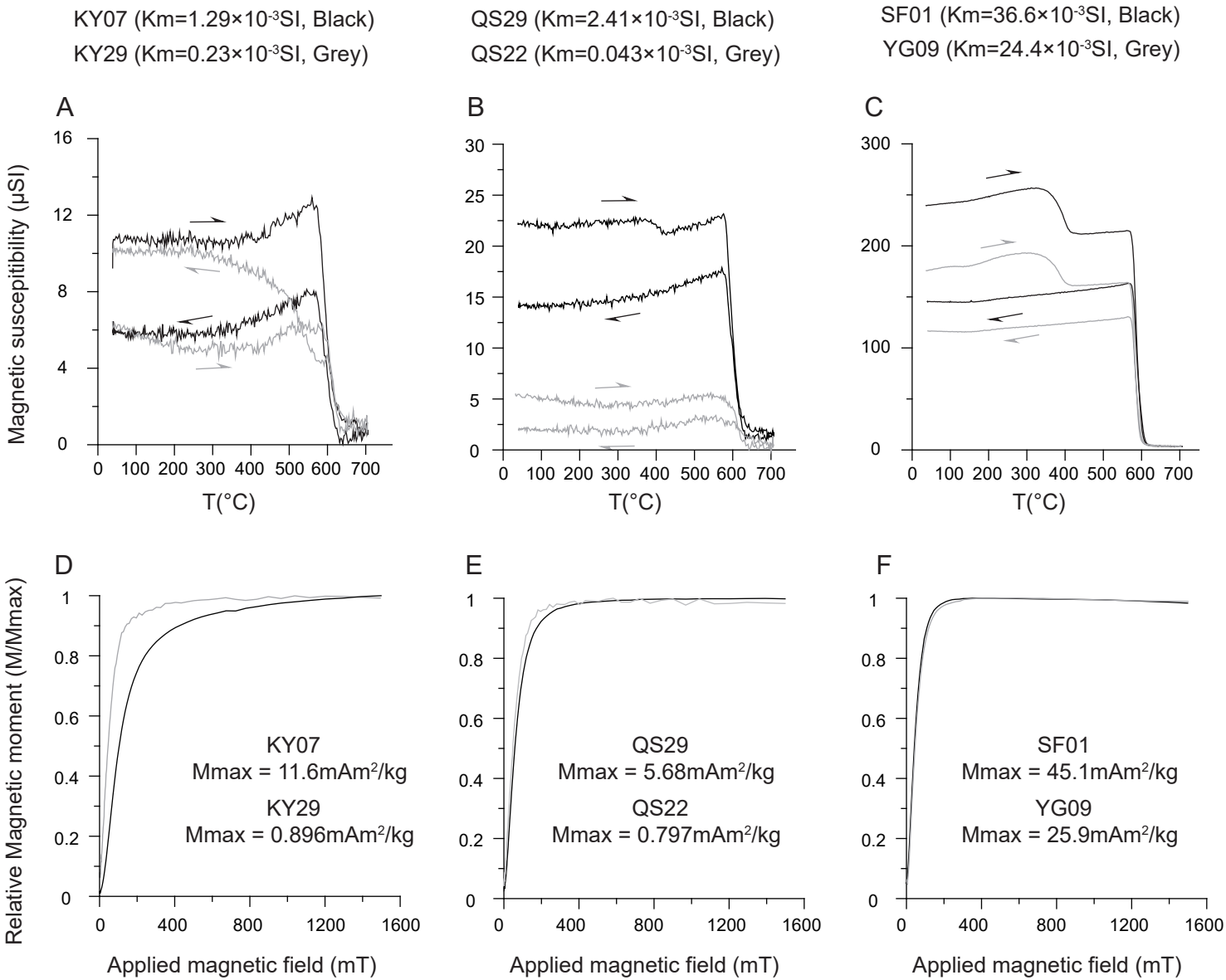
KY07 (Km=1.29×10-3SI, Black)
KY29 (Km=0.23×10-3SI, Grey)
QS29 (Km=2.41×10-3SI, Black)
QS22 (Km=0.043×10-3SI, Grey)
SF01 (Km=36.6×10-3SI, Black)
YG09 (Km=24.4×10-3SI, Grey)
A
B
C
Magnetic suscepitibility (μSI)
T(°C)
D
E
F
Relative Magnetic moment (M/Mmax)
KY07
Mmax = 11.6mAm2/kg
KY29
Mmax = 0.896mAm2/kg
QS29
Mmax = 5.68mAm2/kg
QS22
Mmax = 0.797mAm2/kg
SF01
Mmax = 45.1mAm2/kg
YG09
Mmax = 25.9mAm2/kg
Applied magnetic field (mT)

**Figure 14.**

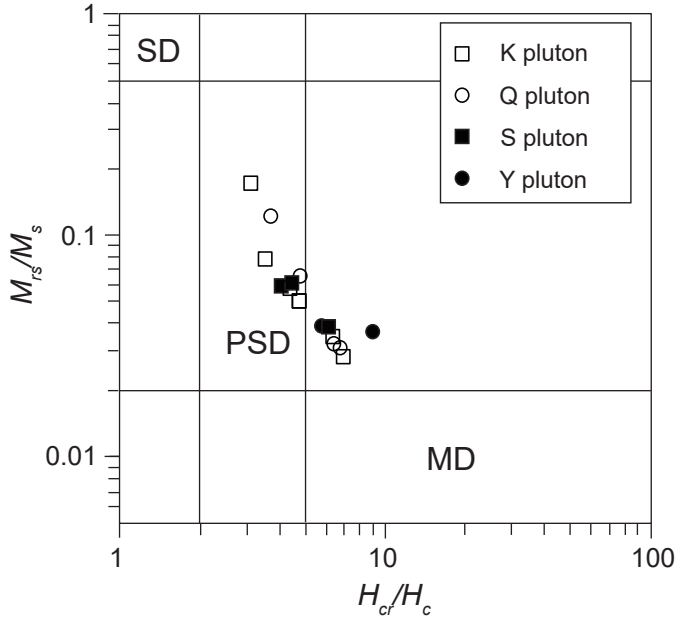
SD
PSD
MD
K pluton
Q pluton
S pluton
Y pluton
1
0.1
0.01
1
10
100
$M_{rs}/M_s$
$H_{cr}/H_c$

**Figure 16.**

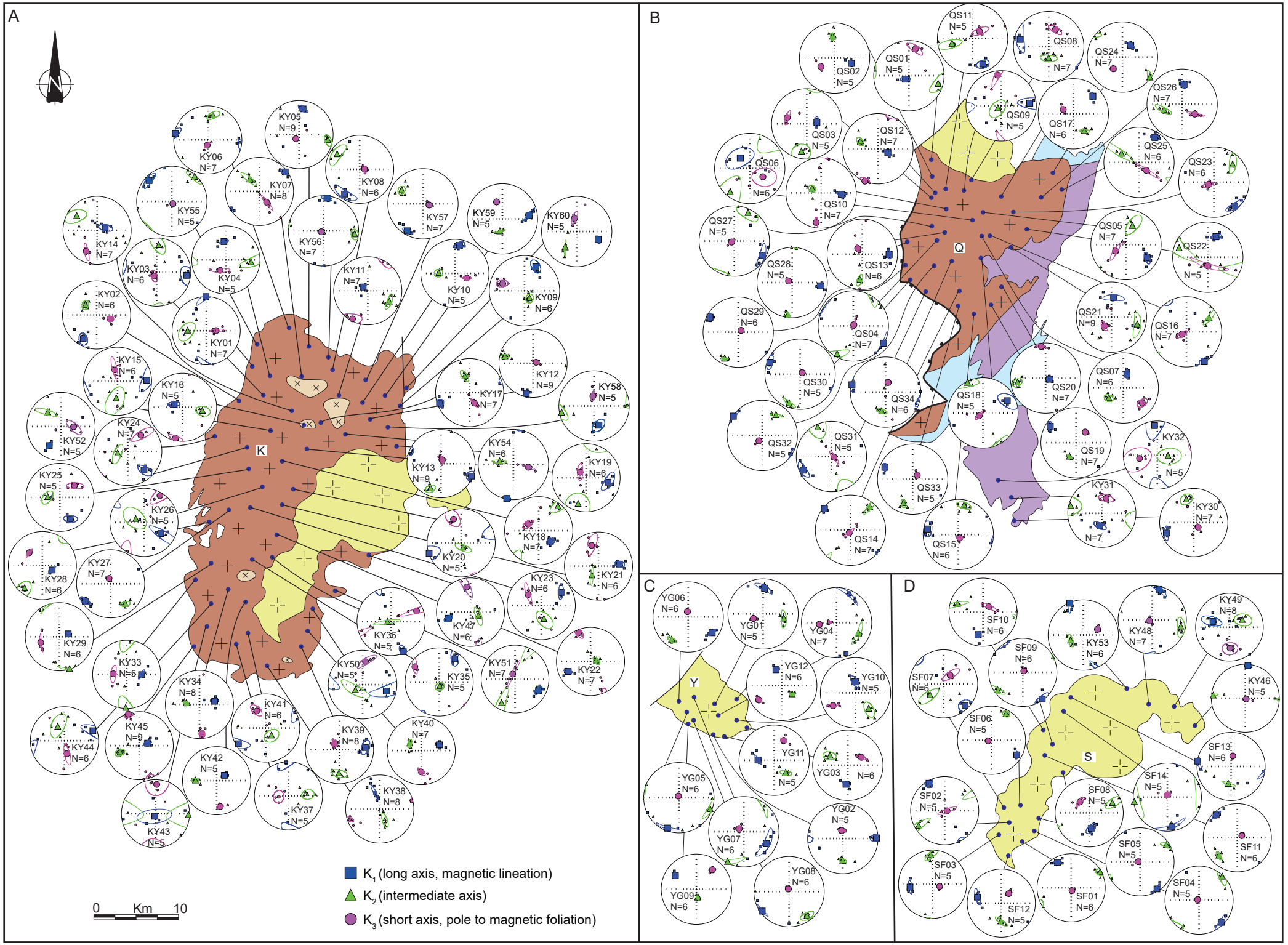
A
B
C
D
K
Q
Y
S
KY01 N=7
KY02 N=6
KY03 N=6
KY04 N=5
KY05 N=9
KY06 N=7
KY07 N=8
KY08 N=6
KY09 N=6
KY10 N=5
KY11 N=7
KY12 N=9
KY13 N=9
KY14 N=7
KY15 N=6
KY16 N=5
KY17 N=7
KY18 N=7
KY19 N=6
KY20 N=5
KY21 N=6
KY22 N=7
KY23 N=6
KY24 N=7
KY25 N=5
KY26 N=5
KY27 N=7
KY28 N=6
KY29 N=6
KY30 N=7
KY31 N=7
KY32 N=5
KY33 N=5
KY34 N=8
KY35 N=5
KY36 N=5
KY37 N=5
KY38 N=8
KY39 N=8
KY40 N=7
KY41 N=6
KY42 N=5
KY43 N=5
KY44 N=6
KY45 N=9
KY46 N=5
KY47 N=6
KY48 N=7
KY49 N=8
KY50 N=5
KY51 N=7
KY52 N=5
KY53 N=6
KY54 N=6
KY55 N=5
KY56 N=7
KY57 N=7
KY58 N=5
KY59 N=5
KY60 N=5
QS01 N=5
QS02 N=5
QS03 N=5
QS04 N=7
QS05 N=7
QS06 N=6
QS07 N=6
QS08 N=7
QS09 N=5
QS10 N=7
QS11 N=5
QS12 N=7
QS13 N=6
QS14 N=7
QS15 N=6
QS16 N=7
QS17 N=6
QS18 N=5
QS19 N=7
QS20 N=7
QS21 N=9
QS22 N=5
QS23 N=6
QS24 N=7
QS25 N=6
QS26 N=7
QS27 N=5
QS28 N=5
QS29 N=6
QS30 N=5
QS31 N=5
QS32 N=5
QS33 N=5
QS34 N=6
YG01 N=5
YG02 N=5
YG03 N=6
YG04 N=7
YG05 N=6
YG06 N=6
YG07 N=6
YG08 N=6
YG09 N=6
YG10 N=5
YG11 N=5
YG12 N=6
SF01 N=6
SF02 N=5
SF03 N=5
SF04 N=5
SF05 N=5
SF06 N=5
SF07 N=6
SF08 N=5
SF09 N=6
SF10 N=6
SF11 N=6
SF12 N=5
SF13 N=6
SF14 N=5
0 Km 10
K1 (long axis, magnetic lineation)
K2 (intermediate axis)
K3 (short axis, pole to magnetic foliation)

**Figure15.**

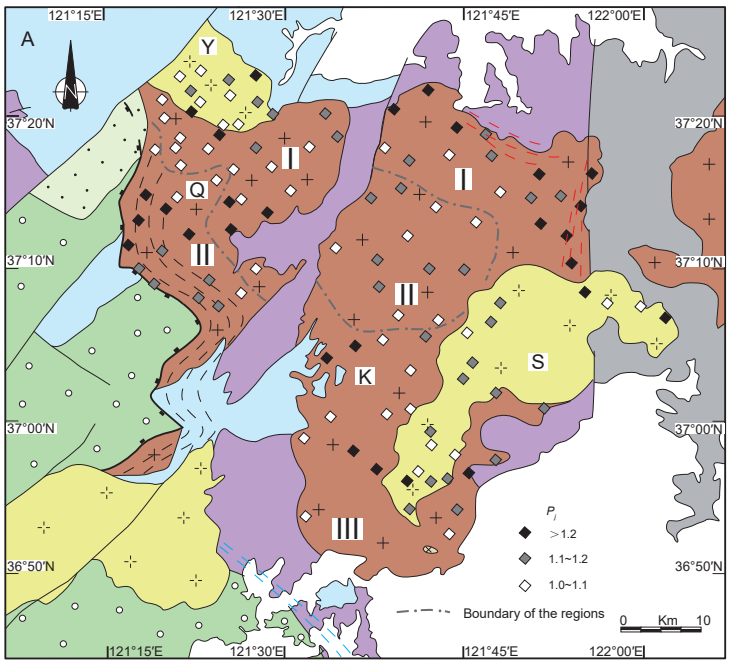
A
121°15'E
121°30'E
121°45'E
122°00'E
37°20'N
37°10'N
37°00'N
36°50'N
Y
Q
K
S
I
II
III
$P_j$
>1.2
1.1~1.2
1.0~1.1
Boundary of the regions
0 Km 10

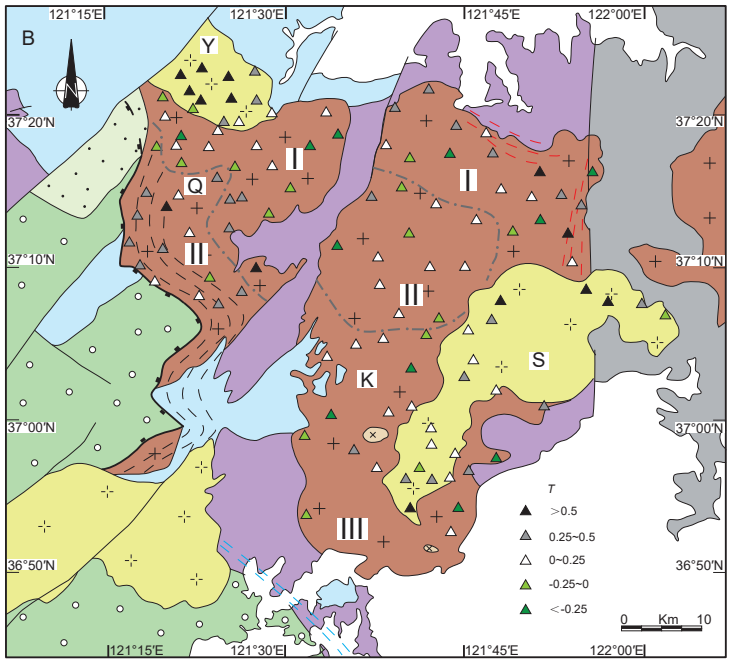
B
121°15'E
121°30'E
121°45'E
122°00'E
37°20'N
37°10'N
37°00'N
36°50'N
Y
Q
K
S
I
II
III
T
>0.5
0.25~0.5
0~0.25
-0.25~0
<-0.25
0 Km 10

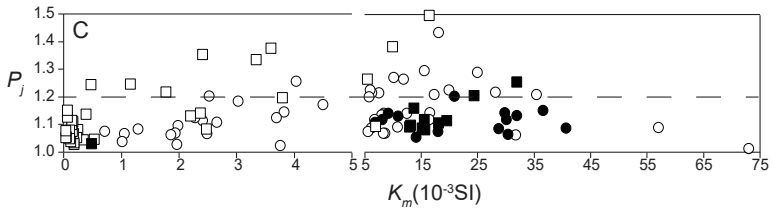
C
$P_j$
$K_m$(10$^{-3}$SI)

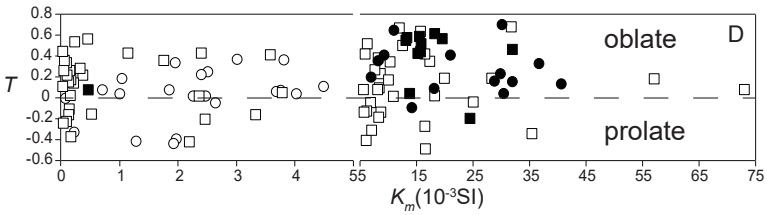
D
T
oblate
prolate
$K_m$(10$^{-3}$SI)

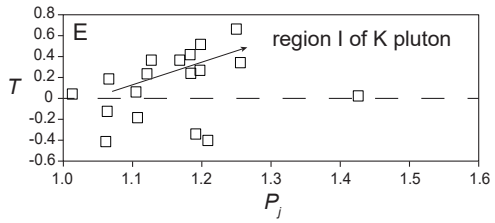
E
region I of K pluton
T
$P_j$

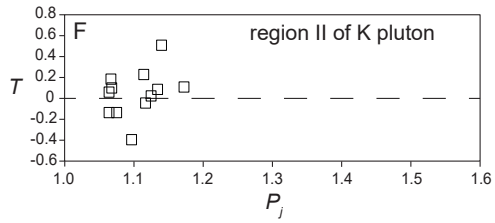
F
region II of K pluton
T
$P_j$

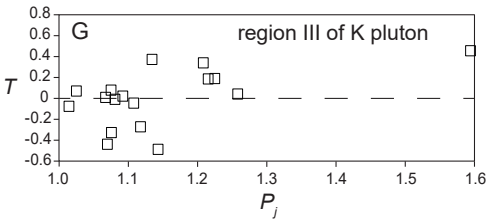
G
region III of K pluton
T
$P_j$

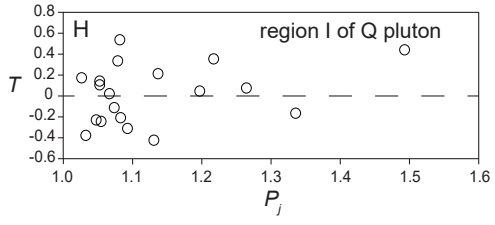
H
region I of Q pluton
T
$P_j$

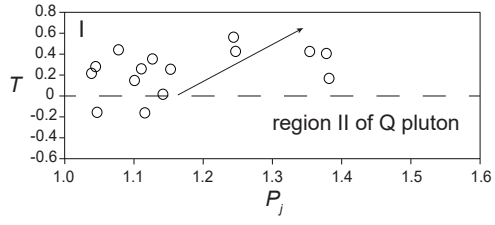
I
region II of Q pluton
T
$P_j$

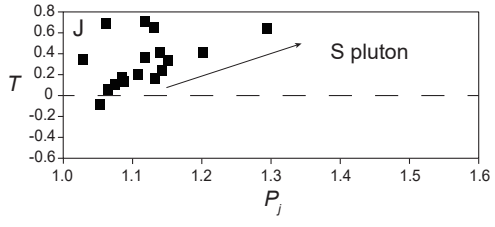
J
S pluton
T
$P_j$

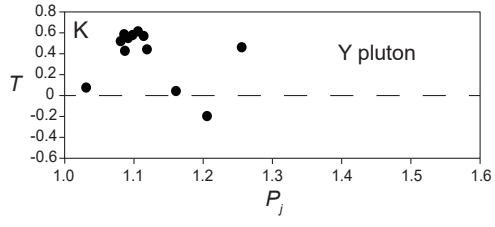
K
Y pluton
T
$P_j$

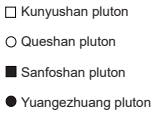
Kunyushan pluton
Queshan pluton
Sanfoshan pluton
Yuangezhuang pluton

**Figure 17.**

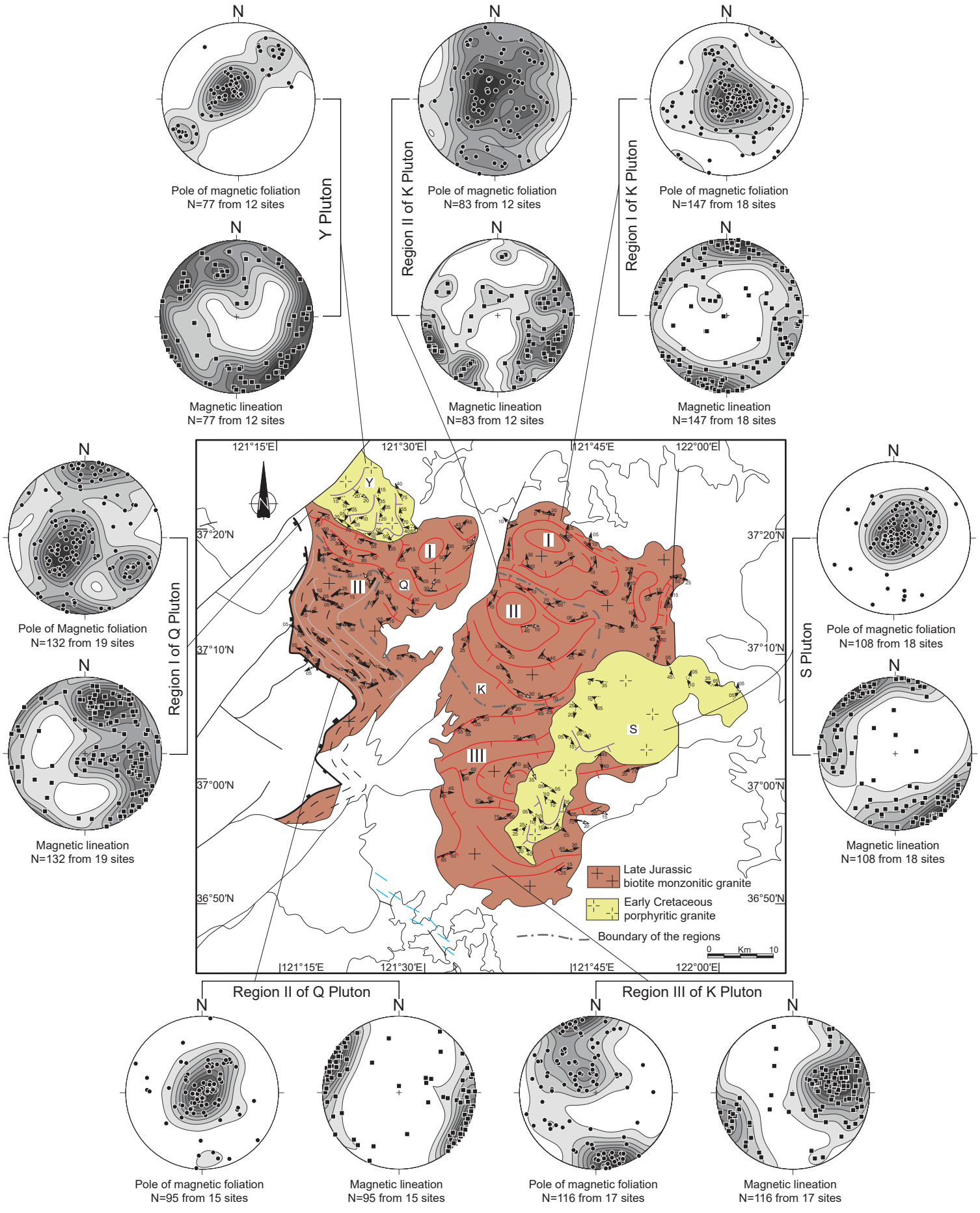
N
Pole of magnetic foliation
N=77 from 12 sites
Y Pluton
Magnetic lineation
N=77 from 12 sites
Region II of K Pluton
Pole of magnetic foliation
N=83 from 12 sites
Magnetic lineation
N=83 from 12 sites
Region I of K Pluton
Pole of magnetic foliation
N=147 from 18 sites
Magnetic lineation
N=147 from 18 sites
Pole of Magnetic foliation
N=132 from 19 sites
Region I of Q Pluton
Magnetic lineation
N=132 from 19 sites
S Pluton
Pole of magnetic foliation
N=108 from 18 sites
Magnetic lineation
N=108 from 18 sites
121°15′E
121°30′E
121°45′E
122°00′E
37°20′N
37°10′N
37°00′N
36°50′N
Y
I
II
III
Q
K
S
Late Jurassic
biotite monzonitic granite
Early Cretaceous
porphyritic granite
Boundary of the regions
0 Km 10
Region II of Q Pluton
Pole of magnetic foliation
N=95 from 15 sites
Magnetic lineation
N=95 from 15 sites
Region III of K Pluton
Pole of magnetic foliation
N=116 from 17 sites
Magnetic lineation
N=116 from 17 sites
Magnetic foliation/lineation acquired during
Late Jurassic magma crystallization (Mag1)
well-defined
poorly-defined
Magnetic foliation/lineation acquired during
top-to-the-NE shearing (D1)
well-defined
poorly-defined
Magnetic foliation/lineation acquired during
top-to-the-WNW shearing (D3)
well-defined
poorly-defined
Magnetic foliation/lineation acquired during
Early Cretaceous magma crystallization (Mag2)
well-defined
poorly-defined
Magnetic foliation
trajectory related to Mag1/D1
Magnetic foliation
trajectory related to D3
Magnetic foliation
trajectory related to Mag2

**Figure 18.**

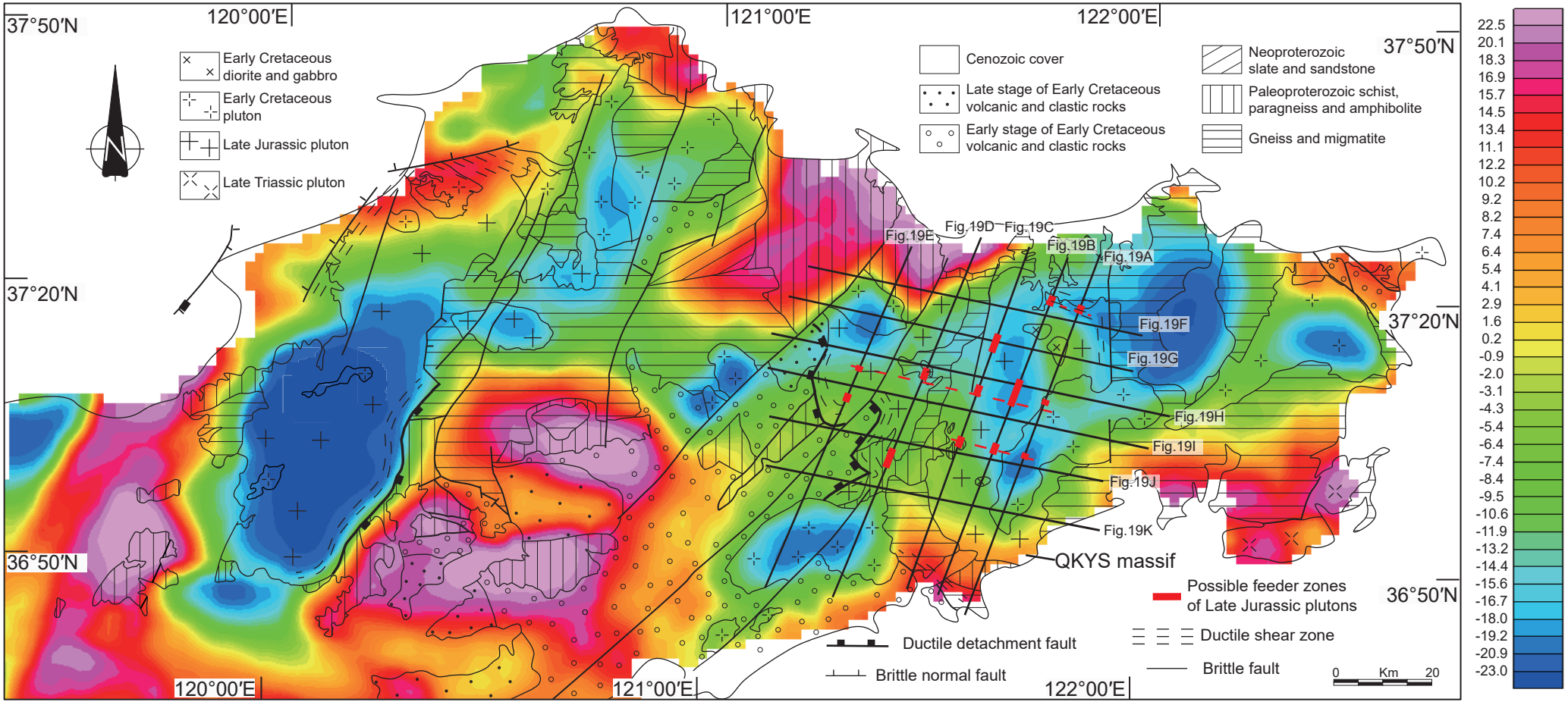
37°50′N
120°00′E
121°00′E
122°00′E
37°20′N
36°50′N
N
Early Cretaceous diorite and gabbro
Early Cretaceous pluton
Late Jurassic pluton
Late Triassic pluton
Cenozoic cover
Late stage of Early Cretaceous volcanic and clastic rocks
Early stage of Early Cretaceous volcanic and clastic rocks
Neoproterozoic slate and sandstone
Paleoproterozoic schist, paragneiss and amphibolite
Gneiss and migmatite
Fig.19E
Fig.19D
Fig.19C
Fig.19B
Fig.19A
Fig.19F
Fig.19G
Fig.19H
Fig.19I
Fig.19J
Fig.19K
QKYS massif
Possible feeder zones of Late Jurassic plutons
Ductile shear zone
Brittle fault
Ductile detachment fault
Brittle normal fault
0 Km 20
22.5
20.1
18.3
16.9
15.7
14.5
13.4
11.1
12.2
10.2
9.2
8.2
7.4
6.4
5.4
4.1
2.9
1.6
0.2
-0.9
-2.0
-3.1
-4.3
-5.4
-6.4
-7.4
-8.4
-9.5
-10.6
-11.9
-13.2
-14.4
-15.6
-16.7
-18.0
-19.2
-20.9
-23.0

**Figure 19.**

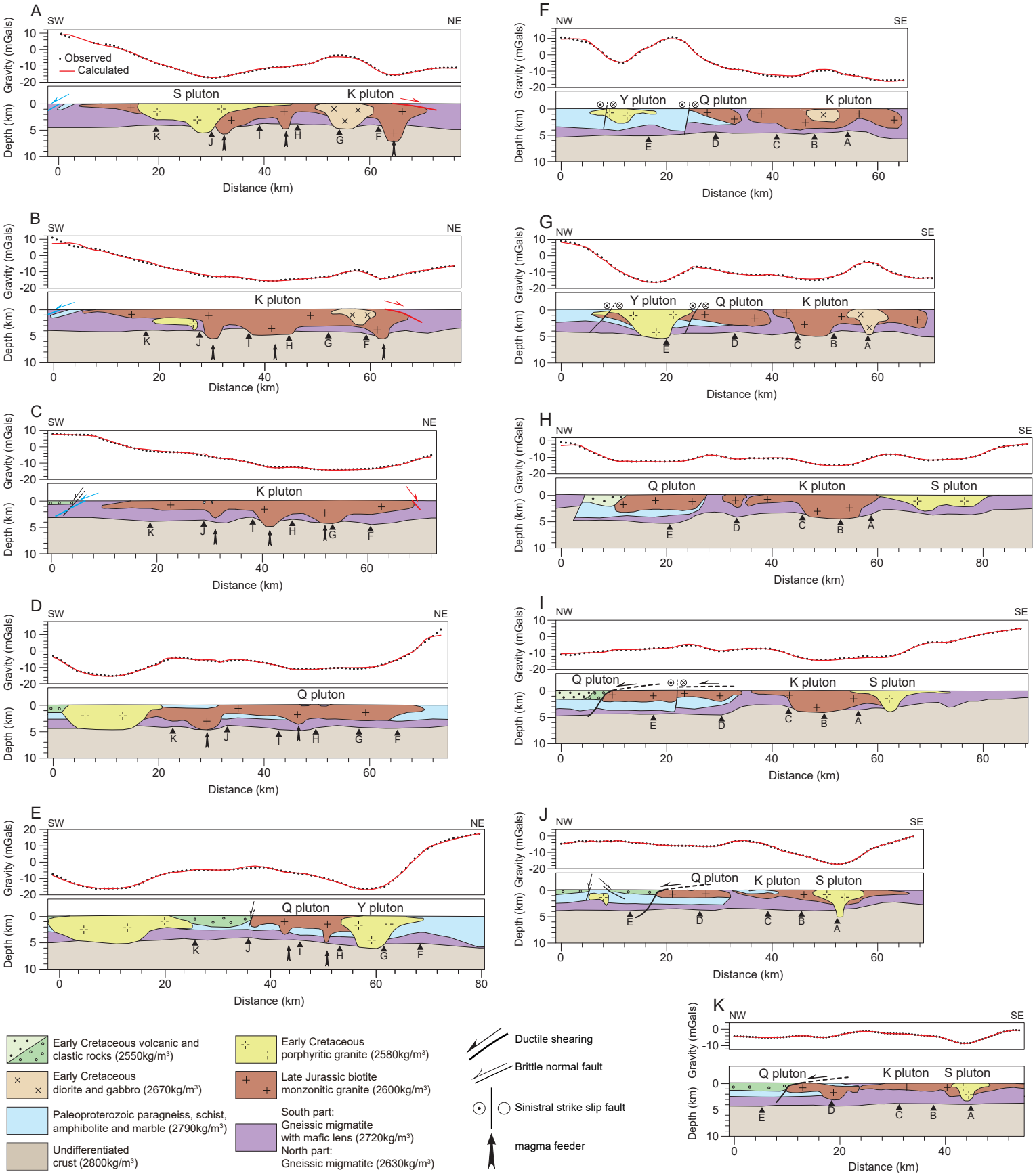
A
SW
NE
Gravity (mGals)
Observed
Calculated
S pluton
K pluton
Depth (km)
Distance (km)
B
K pluton
C
K pluton
D
Q pluton
E
Q pluton
Y pluton
F
NW
SE
Y pluton
Q pluton
K pluton
G
Y pluton
Q pluton
K pluton
H
Q pluton
K pluton
S pluton
I
Q pluton
K pluton
S pluton
J
Q pluton
K pluton
S pluton
K
Q pluton
K pluton
S pluton
Early Cretaceous volcanic and clastic rocks (2550kg/m³)
Early Cretaceous diorite and gabbro (2670kg/m³)
Paleoproterozoic paragneiss, schist, amphibolite and marble (2790kg/m³)
Undifferentiated crust (2800kg/m³)
Early Cretaceous porphyritic granite (2580kg/m³)
Late Jurassic biotite monzonitic granite (2600kg/m³)
South part: Gneissic migmatite with mafic lens (2720kg/m³)
North part: Gneissic migmatite (2630kg/m³)
Ductile shearing
Brittle normal fault
Sinistral strike slip fault
magma feeder

**Figure 20.**

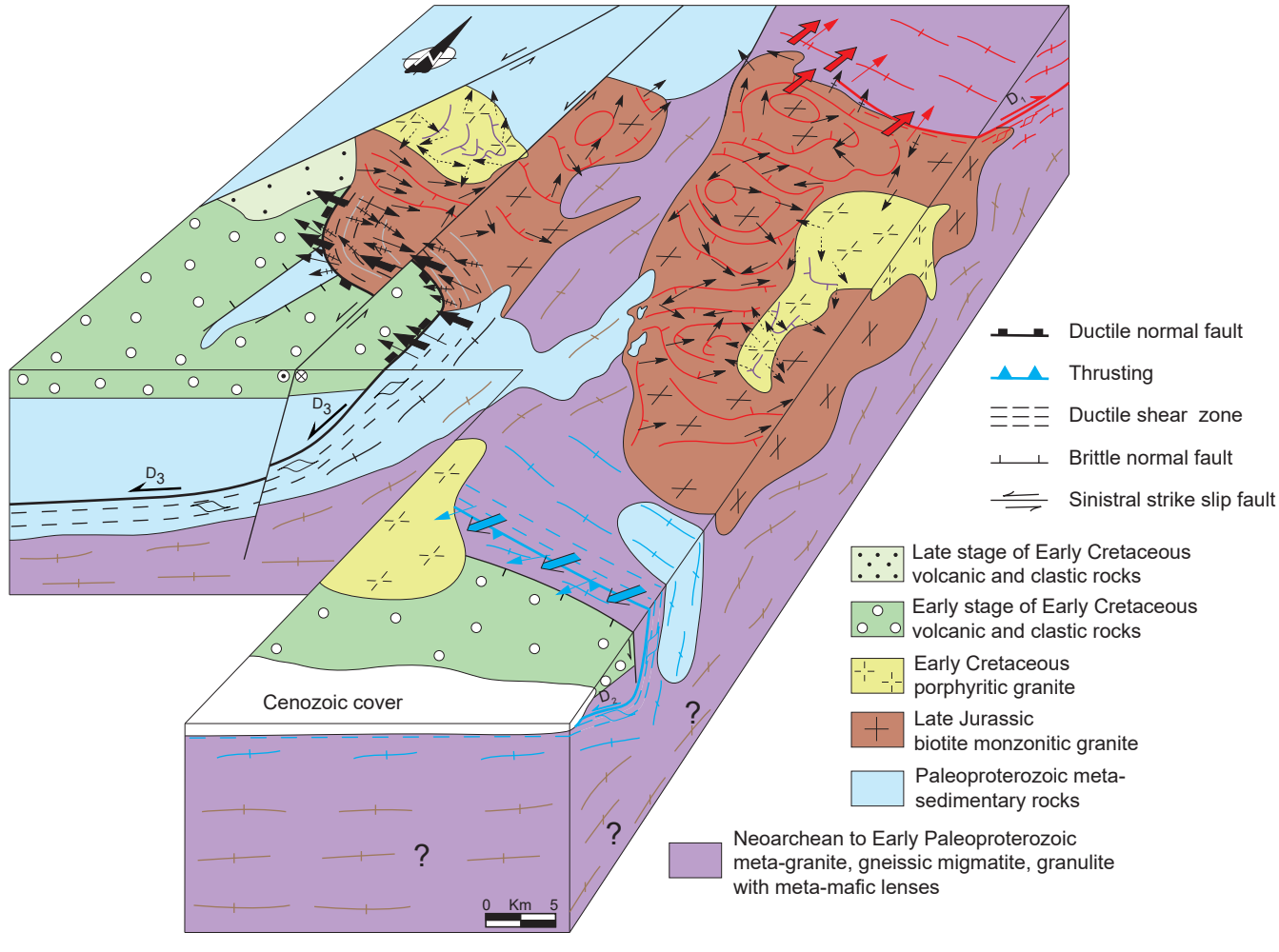
D1
D3
D3
D2
Cenozoic cover
?
?
?
0 Km 5
Ductile normal fault
Thrusting
Ductile shear zone
Brittle normal fault
Sinistral strike slip fault
Late stage of Early Cretaceous volcanic and clastic rocks
Early stage of Early Cretaceous volcanic and clastic rocks
Early Cretaceous porphyritic granite
Late Jurassic biotite monzonitic granite
Paleoproterozoic meta-sedimentary rocks
Neoarchean to Early Paleoproterozoic meta-granite, gneissic migmatite, granulite with meta-mafic lenses
Sub-solidus foliation related to D1
Sub-solidus foliation related to D2
Sub-solidus foliation related to D3
Sub-solidus foliation related to pre-D1
Mineral lineation related to D1
Mineral lineation related to D2
Mineral lineation related to D3
AMS foliation trajectory related to Mag1/D1
AMS foliation trajectory related to D3
AMS foliation trajectory related to Mag2
AMS lineation related to Mag1
AMS lineation related to D1
AMS lineation related to D3
AMS lineation related to Mag2
Ductile shearing related to D1
Ductile shearing related to D2
Ductile shearing related to D3

**Figure 21.**

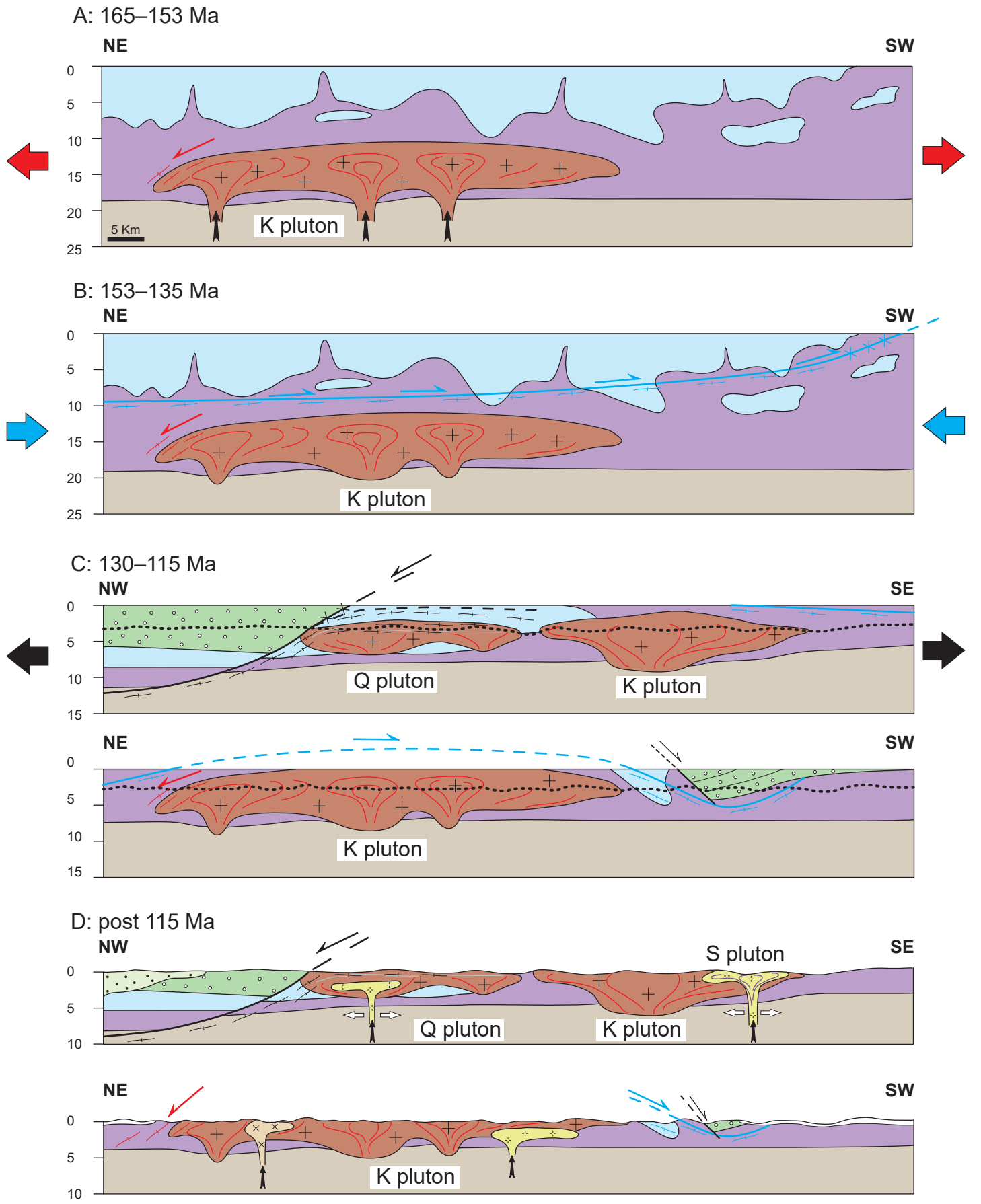
A: 165–153 Ma
NE
SW
0
5
10
15
20
25
5 Km
K pluton
B: 153–135 Ma
NE
SW
0
5
10
15
20
25
K pluton
C: 130–115 Ma
NW
SE
0
5
10
15
Q pluton
K pluton
NE
SW
0
5
10
15
K pluton
D: post 115 Ma
NW
SE
0
5
10
S pluton
Q pluton
K pluton
NE
SW
0
5
10
K pluton
Cenozoic cover
Late stage of Early Cretaceous volcanic and clastic rocks
Early stage of Early Cretaceous volcanic and clastic rocks
Early Cretaceous porphyritic granite
Early Cretaceous diorite and gabbro
Late Jurassic biotite monzonitic granite
Paleoproterozoic meta-sedimentary rocks
Neoarchean to Early Paleoproterozoic meta-granite, gneissic migmatite and granulite with meta-mafic lenses
Undifferentiated crust
Top-to-the-NE shearing related to NE-SW extension (D1)
Top-to-the-SW shearing related to NE-SW compression (D2)
Top-to-the-WNW shearing related to WNW-ESE extension (D3)
Sub-solidus foliation related to D1
Sub-solidus foliation related to D2
Sub-solidus foliation related to D3
Magnetic foliation related to Mag1/D1
Magneitc foliation related to D3
Magnetic foliation related to Mag2
Possible opening orientation of the fracture
Magma feeder
Brittle normal faulting
Brittle phase overprint
Denudation line

**Figure 22.**

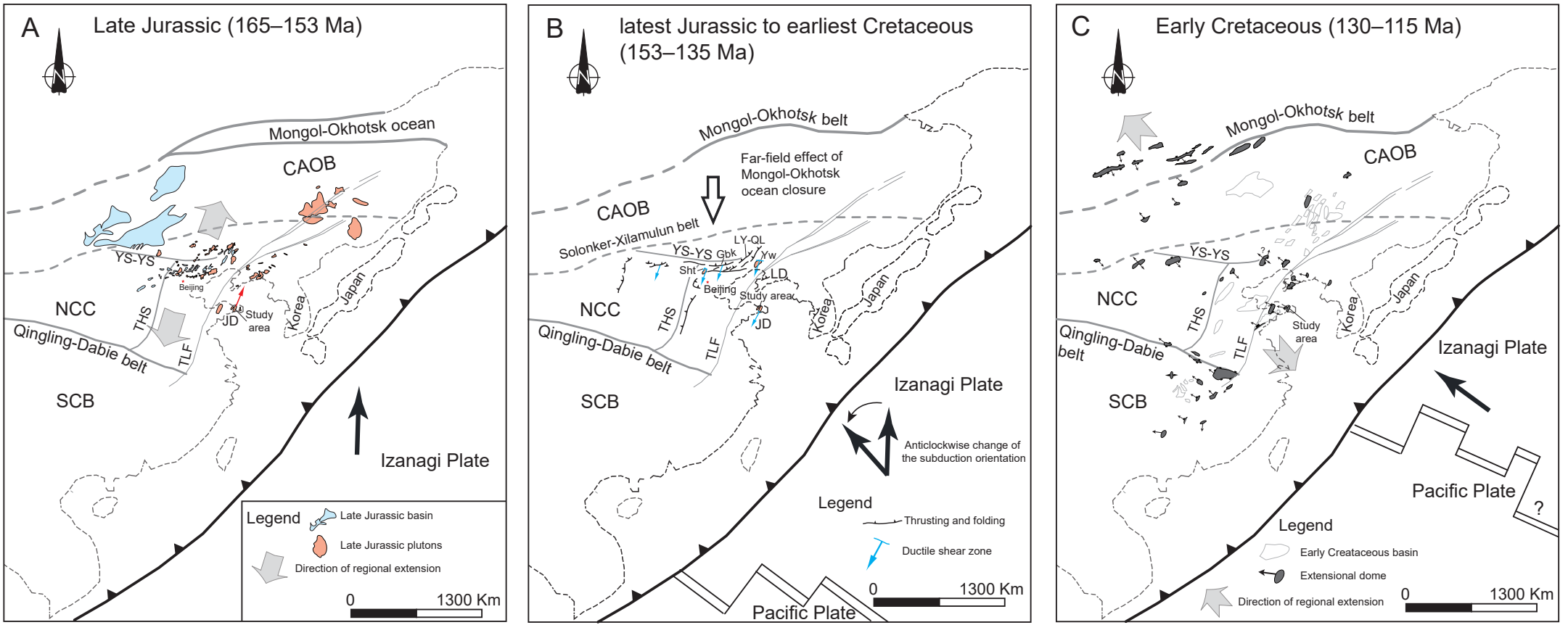
A
Late Jurassic (165–153 Ma)
Mongol-Okhotsk ocean
CAOB
YS-YS
Beijing
NCC
THS
TLF
JD
Study area
Korea
Japan
Qingling-Dabie belt
SCB
Izanagi Plate
Legend
Late Jurassic basin
Late Jurassic plutons
Direction of regional extension
0
1300 Km
B
latest Jurassic to earliest Cretaceous (153–135 Ma)
Mongol-Okhotsk belt
Far-field effect of Mongol-Okhotsk ocean closure
CAOB
Solonker-Xilamulun belt
YS-YS
Gbk
LY-QL
Yw
Sht
LD
Beijing
Study area
JD
NCC
THS
TLF
Korea
Japan
Qingling-Dabie belt
SCB
Izanagi Plate
Anticlockwise change of the subduction orientation
Legend
Thrusting and folding
Ductile shear zone
0
1300 Km
Pacific Plate
C
Early Cretaceous (130–115 Ma)
Mongol-Okhotsk belt
CAOB
YS-YS
NCC
THS
TLF
Study area
Korea
Japan
Qingling-Dabie belt
SCB
Izanagi Plate
Pacific Plate
?
Legend
Early Creataceous basin
Extensional dome
Direction of regional extension
0
1300 Km

| site | Coordinates | | Lithology | N | Km | $P_J$ | T | $K_1$ | | | | $K_3$ | | | |
|---|---|---|---|---|---|---|---|---|---|---|---|---|---|---|---|
| | Long(°E) | Lat(°N) | | | ($10^{-3}$SI) | | | Dec(°) | Inc(°) | $\alpha_{95max}$(°) | $\alpha_{95min}$(°) | Dec(°) | Inc(°) | $\alpha_{95max}$(°) | $\alpha_{95min}$(°) |
| KY01 | 121.6419 | 37.2974 | biotite monzogranite(KYS) | 7 | 1.01 | 1.038 | 0.036 | 359.5 | 0.0 | 23.8 | 4.4 | 89.5 | 57.4 | 22 | 4.1 |
| KY02 | 121.6151 | 37.2439 | biotite monzogranite(KYS) | 6 | 12.50 | 1.14 | 0.5 | 209.4 | 12.8 | 12.7 | 8.7 | 106.4 | 44.8 | 10.1 | 7.8 |
| KY03 | 121.6648 | 37.2539 | biotite monzogranite(KYS) | 6 | 6.78 | 1.117 | -0.046 | 96.2 | 7.0 | 18.4 | 11.7 | 212.6 | 74.6 | 19.3 | 10.1 |
| KY04 | 121.6760 | 37.2846 | biotite monzogranite(KYS) | 5 | 8.26 | 1.128 | -0.187 | 354.4 | 33.3 | 11.7 | 3.4 | 208.3 | 51.6 | 30.3 | 6.6 |
| KY05 | 121.7458 | 37.3295 | biotite monzogranite(KYS) | 9 | 7.51 | 1.214 | 0.265 | 8.8 | 15.3 | 11.9 | 4.6 | 218.9 | 72.5 | 7.8 | 4.9 |
| KY06 | 121.7120 | 37.3561 | biotite monzogranite(KYS) | 7 | 2.52 | 1.203 | 0.251 | 281.4 | 1.6 | 13.6 | 5.5 | 186.4 | 72.2 | 12.2 | 2.9 |
| KY07 | 121.7305 | 37.2885 | biotite monzogranite(KYS) | 8 | 1.29 | 1.084 | -0.418 | 52.8 | 3.1 | 9.5 | 4 | 146.3 | 48.4 | 26.2 | 4.1 |
| KY08 | 121.7936 | 37.2911 | biotite monzogranite(KYS) | 6 | 3.82 | 1.147 | 0.364 | 211.3 | 9.2 | 26.3 | 7.2 | 87.3 | 73.8 | 13.6 | 4.1 |
| KY09 | 121.9219 | 37.2359 | biotite monzogranite(KYS) | 6 | 10.20 | 1.271 | 0.344 | 25.5 | 16.1 | 15 | 8.6 | 288.2 | 23.8 | 13.4 | 23.8 |
| KY10 | 121.8445 | 37.2421 | biotite monzogranite(KYS) | 5 | 8.40 | 1.141 | 0.224 | 9.4 | 10.2 | 10.7 | 5.8 | 111.3 | 48.8 | 11.9 | 5.9 |
| KY11 | 121.8059 | 37.2407 | biotite monzogranite(KYS) | 7 | 57.00 | 1.088 | 0.181 | 308.9 | 70.3 | 9.4 | 6.2 | 208.6 | 3.7 | 18.3 | 9.2 |
| KY12 | 121.8566 | 37.2179 | biotite monzogranite(KYS) | 9 | 35.40 | 1.209 | -0.344 | 192.7 | 5.5 | 4.9 | 3.6 | 72.6 | 79.1 | 8 | 4.1 |
| KY13 | 121.8106 | 37.2048 | biotite monzogranite(KYS) | 9 | 6.15 | 1.086 | -0.13 | 112.2 | 2.1 | 9.6 | 8.6 | 13.2 | 76.5 | 11.5 | 5.8 |
| KY14 | 121.7138 | 37.2335 | biotite monzogranite(KYS) | 7 | 1.86 | 1.064 | 0.074 | 72.1 | 62.0 | 22.7 | 9.9 | 207.8 | 20.9 | 20.3 | 4.4 |
| KY15 | 121.6732 | 37.2017 | biotite monzogranite(KYS) | 6 | 5.59 | 1.074 | -0.141 | 88 | 8.7 | 27.8 | 9.9 | 346.6 | 52.2 | 35.3 | 6.7 |
| KY16 | 121.7397 | 37.2056 | Early Creataceous diorite | 5 | 10.60 | 1.019 | 0.572 | 290.5 | 60.7 | 18.7 | 7.8 | 192.9 | 4.2 | 14.1 | 3.8 |
| KY17 | 121.7634 | 37.2145 | biotite monzogranite(KYS) | 7 | 8.28 | 1.068 | 0.096 | 250.7 | 3.8 | 8.4 | 6.9 | 155.6 | 52.8 | 17.9 | 3.3 |
| KY18 | 121.6993 | 37.1647 | biotite monzogranite(KYS) | 7 | 2.27 | 1.125 | 0.015 | 133 | 39.8 | 11.9 | 8.6 | 301.7 | 49.7 | 18.6 | 8.4 |
| KY19 | 121.7519 | 37.1648 | biotite monzogranite(KYS) | 6 | 4.50 | 1.173 | 0.105 | 101.4 | 23.2 | 24.7 | 9.3 | 312.8 | 63.3 | 26.2 | 8.3 |
| KY20 | 121.7139 | 37.1110 | biotite monzogranite(KYS) | 5 | 8.61 | 1.068 | -0.141 | 251.9 | 0.6 | 24.2 | 12.4 | 342.1 | 17.7 | 21 | 13.3 |
| KY21 | 121.7007 | 37.0931 | biotite monzogranite(KYS) | 6 | 2.65 | 1.108 | -0.049 | 84.50 | 26.4 | 11.9 | 7.1 | 341.4 | 24.6 | 26.3 | 9.5 |
| KY22 | 121.6871 | 37.0537 | biotite monzogranite(KYS) | 7 | 1.93 | 1.07 | -0.437 | 245.9 | 18.8 | 9.3 | 2.8 | 337.8 | 5.3 | 13.8 | 5.5 |
| KY23 | 121.6377 | 37.0857 | biotite monzogranite(KYS) | 6 | 2.48 | 1.068 | 0.017 | 56.4 | 20.2 | 17.3 | 5.5 | 310.3 | 36.9 | 30 | 5.3 |
| KY24 | 121.6294 | 37.1753 | biotite monzogranite(KYS) | 7 | 2.41 | 1.115 | 0.223 | 138.8 | 18.3 | 16.9 | 8.5 | 39 | 27.3 | 29.8 | 9 |
| KY25 | 121.6328 | 37.1474 | biotite monzogranite(KYS) | 5 | 7.99 | 1.134 | 0.079 | 154.3 | 19.9 | 15.7 | 7.8 | 51.1 | 32.4 | 22.3 | 7.5 |
| KY26 | 121.6584 | 37.1132 | biotite monzogranite(KYS) | 5 | 1.05 | 1.067 | 0.184 | 123.6 | 28.6 | 40.1 | 9.8 | 30.8 | 5.1 | 27 | 10.1 |
| KY27 | 121.5992 | 37.0811 | biotite monzogranite(KYS) | 7 | 19.90 | 1.225 | 0.188 | 235.8 | 5.8 | 10.2 | 4.6 | 343.6 | 71.5 | 6.3 | 4.2 |
| KY28 | 121.5584 | 37.0658 | biotite monzogranite(KYS) | 6 | 4.03 | 1.258 | 0.039 | 114.2 | 55.1 | 16.2 | 0.9 | 314.1 | 33.3 | 14.1 | 2.5 |
| KY29 | 121.5651 | 37.0034 | biotite monzogranite(KYS) | 6 | 0.23 | 1.076 | -0.332 | 72.4 | 59.6 | 6.5 | 0.8 | 252.5 | 30.4 | 23.8 | 1.8 |
| KY30 | 121.4989 | 36.8105 | mylonitic gneiss | 7 | 1.11 | 1.159 | -0.059 | 249 | 8.6 | 14.3 | 4.3 | 136.5 | 68.5 | 10.8 | 4.2 |
| KY31 | 121.4873 | 36.8450 | felsic vein | 7 | 0.20 | 1.028 | 0.047 | 189 | 49.4 | 20 | 8.3 | 15.8 | 40.4 | 21.3 | 9.2 |
| KY32 | 121.4726 | 36.8737 | felsic vein | 5 | 0.45 | 1.024 | 0.163 | 354.7 | 8.0 | 33.7 | 15.7 | 259.2 | 34 | 37.5 | 27.3 |
| KY33 | 121.5264 | 36.9803 | biotite monzogranite(KYS) | 5 | 0.09 | 1.081 | -0.004 | 91 | 42.9 | 15 | 3.5 | 272.6 | 47.1 | 25.6 | 7.7 |
| KY34 | 121.5996 | 36.9666 | biotite monzogranite(KYS) | 8 | 2.10 | 1.595 | 0.451 | 78.1 | 41.1 | 6.8 | 6.4 | 175.3 | 8.2 | 7.4 | 5.5 |
| KY35 | 121.6425 | 37.0062 | biotite monzogranite(KYS) | 5 | 3.76 | 1.025 | 0.069 | 34.1 | 11.2 | 16 | 8.1 | 302.2 | 9.7 | 15.8 | 4.5 |
| KY36 | 121.6826 | 37.0094 | biotite monzogranite(KYS) | 5 | 0.71 | 1.075 | 0.073 | 157.9 | 2.8 | 13.6 | 5.7 | 67.4 | 12.1 | 42 | 5.1 |
| KY37 | 121.6111 | 36.8808 | felsic vein | 5 | 1.68 | 1.029 | -0.243 | 355.9 | 0.7 | 20.8 | 9.1 | 264.7 | 58.2 | 19.6 | 15.9 |
| KY38 | 121.6692 | 36.8484 | felsic vein | 8 | 0.26 | 1.031 | 0.283 | 343.7 | 38.2 | 21.6 | 3.3 | 250.5 | 4.1 | 7.7 | 3.6 |
| KY39 | 121.7309 | 36.8761 | biotite monzogranite(KYS) | 8 | 10.80 | 1.092 | 0.015 | 85.3 | 15.5 | 16.1 | 8.3 | 320.1 | 64.3 | 11.6 | 8.3 |
| KY40 | 121.7414 | 36.9019 | biotite monzogranite(KYS) | 7 | 16.40 | 1.118 | -0.272 | 72.3 | 31.8 | 7.4 | 4.5 | 179.9 | 26 | 11.8 | 4.6 |
| KY41 | 121.6353 | 36.8967 | felsic vein | 6 | 25.70 | 1.023 | 0.308 | 240 | 4.6 | 24.9 | 8.2 | 332.8 | 31 | 18.1 | 9.1 |
| KY42 | 121.6286 | 36.9453 | biotite monzogranite(KYS) | 5 | 28.20 | 1.216 | 0.187 | 55.3 | 58.9 | 8.3 | 4.5 | 172.1 | 15.2 | 7.5 | 3.5 |
| KY43 | 121.5588 | 36.9097 | felsic vein | 5 | 0.54 | 1.038 | 0.34 | 196 | 81.2 | 54.5 | 23.2 | 2.3 | 8.5 | 26 | 21.8 |
| KY44 | 121.5653 | 36.9415 | felsic vein | 6 | 73.00 | 1.012 | 0.079 | 70.7 | 7.1 | 27.2 | 8.9 | 168.6 | 47.9 | 30 | 7.5 |
| KY45 | 121.5273 | 36.8736 | biotite monzogranite(KYS) | 9 | 32.30 | 1.015 | -0.07 | 73.1 | 61.3 | 13 | 6.9 | 341 | 1.2 | 7.8 | 7 |
| KY46 | 122.0301 | 37.1140 | porphyritic granite(SFS) | 5 | 25.00 | 1.29 | -0.04 | 4.6 | 2.1 | 4.4 | 1.4 | 127.5 | 86.2 | 9 | 1.4 |
| KY47 | 121.8757 | 37.0147 | biotite monzogranite(KYS) | 6 | 8.09 | 1.135 | 0.38 | 254.5 | 22.4 | 11.1 | 4.8 | 351.6 | 16.7 | 29.9 | 7 |
| KY48 | 121.9498 | 37.1291 | porphyritic granite(SFS) | 7 | 31.70 | 1.062 | 0.681 | 12.8 | 5.0 | 20 | 3.7 | 253.3 | 80 | 8 | 6.8 |
| KY49 | 121.9962 | 37.1278 | porphyritic granite(SFS) | 8 | 1.96 | 1.028 | 0.337 | 289.1 | 35.6 | 27.3 | 11.7 | 178.4 | 26.3 | 19 | 14.7 |
| KY50 | 121.7542 | 36.9357 | biotite monzogranite(KYS) | 6 | 17.30 | 1.208 | 0.346 | 105.2 | 18.9 | 47.2 | 11.7 | 7.3 | 21.9 | 25.8 | 6.3 |
| KY51 | 121.7936 | 36.9618 | biotite monzogranite(KYS) | 7 | 16.50 | 1.143 | -0.491 | 116.1 | 14.8 | 10.2 | 5.2 | 335.4 | 71.2 | 46 | 4.5 |
| KY52 | 121.5739 | 37.0055 | biotite monzogranite(KYS) | 5 | 1.98 | 1.097 | -0.398 | 211.6 | 23.2 | 12.6 | 1.8 | 91.3 | 49.6 | 28.2 | 10.9 |
| KY53 | 121.9096 | 37.1543 | porphyritic granite(SFS) | 6 | 15.60 | 1.295 | 0.634 | 337.1 | 0.9 | 18.9 | 3.1 | 68 | 42.9 | 8.2 | 4.4 |
| KY54 | 121.9072 | 37.1763 | biotite monzogranite(KYS) | 6 | 18.10 | 1.433 | 0.017 | 190.9 | 0.8 | 5.9 | 2.4 | 100.1 | 43.4 | 20.2 | 2.2 |
| KY55 | 121.6480 | 37.3293 | biotite monzogranite(KYS) | 5 | 5.84 | 1.201 | 0.417 | 312.6 | 7.3 | 16.7 | 5.4 | 154.4 | 82.1 | 6.7 | 3.9 |
| KY56 | 121.7776 | 37.3129 | biotite monzogranite(KYS) | 7 | 3.69 | 1.126 | 0.056 | 6.2 | 3.8 | 9.6 | 3.8 | 246.2 | 82.4 | 7.2 | 3.7 |
| KY57 | 121.8501 | 37.2789 | biotite monzogranite(KYS) | 7 | 6.24 | 1.215 | 0.515 | 209.9 | 6.7 | 9.8 | 3.1 | 101 | 70 | 7.5 | 4.7 |

| | | | | | | | | | | | | | | | |
|---|---|---|---|---|---|---|---|---|---|---|---|---|---|---|---|
| KY58 | 121.8920 | 37.2069 | biotite monzogranite(KYS) | 5 | 11.90 | 1.265 | 0.668 | 166 | 31.3 | 18.6 | 11.2 | 353.7 | 58.5 | 15.2 | 5.5 |
| KY59 | 121.8870 | 37.2536 | biotite monzogranite(KYS) | 5 | 3.02 | 1.186 | 0.367 | 82.4 | 15.2 | 16.9 | 2.9 | 341 | 36 | 3.1 | 1.8 |
| KY60 | 121.9211 | 37.2578 | biotite monzogranite(KYS) | 5 | 6.03 | 1.225 | -0.409 | 110 | 24.0 | 6.6 | 2.3 | 350 | 48.5 | 20.3 | 5.5 |
| SF01 | 121.7004 | 36.9348 | porphyritic granite(SFS) | 6 | 36.60 | 1.151 | 0.326 | 331.6 | 9.6 | 7.8 | 3.5 | 164.2 | 80.2 | 6.6 | 3.3 |
| SF02 | 121.6890 | 36.9333 | porphyritic granite(SFS) | 5 | 14.10 | 1.053 | -0.097 | 330.2 | 4.3 | 8.8 | 7.4 | 92.5 | 82 | 32.7 | 6.2 |
| SF03 | 121.6644 | 36.9279 | porphyritic granite(SFS) | 5 | 20.90 | 1.202 | 0.406 | 262.8 | 22.7 | 16 | 4.3 | 106.6 | 65.5 | 6.3 | 4.7 |
| SF04 | 121.7338 | 36.9378 | porphyritic granite(SFS) | 5 | 31.90 | 1.133 | 0.153 | 134.9 | 4.8 | 16.3 | 3.3 | 293.2 | 84.8 | 7.9 | 3.3 |
| SF05 | 121.7433 | 36.9522 | porphyritic granite(SFS) | 5 | 28.70 | 1.085 | 0.161 | 148 | 3.8 | 9.6 | 2.8 | 274.2 | 83.6 | 9 | 3.4 |
| SF06 | 121.7068 | 36.9741 | porphyritic granite(SFS) | 5 | 18.00 | 1.074 | 0.09 | 120.1 | 8.9 | 7.4 | 1.7 | 260.5 | 78.5 | 5.4 | 3.4 |
| SF07 | 121.7042 | 36.9980 | porphyritic granite(SFS) | 6 | 6.87 | 1.108 | 0.194 | 135.4 | 6.3 | 13.3 | 10.9 | 36.5 | 54.4 | 30.3 | 9.6 |
| SF08 | 121.7999 | 37.0305 | porphyritic granite(SFS) | 5 | 40.60 | 1.086 | 0.129 | 172.8 | 40.5 | 17 | 9 | 319.7 | 44.4 | 16.4 | 4.8 |
| SF09 | 121.7691 | 37.0548 | porphyritic granite(SFS) | 6 | 29.80 | 1.142 | 0.231 | 143.9 | 2.0 | 14.7 | 5.3 | 34.1 | 84.1 | 7.1 | 5.7 |
| SF10 | 121.7465 | 37.1017 | porphyritic granite(SFS) | 6 | 30.40 | 1.065 | 0.041 | 192 | 22.3 | 7.8 | 5.7 | 46.6 | 63.5 | 26.8 | 5.8 |
| SF11 | 121.7493 | 37.0470 | porphyritic granite(SFS) | 6 | 9.19 | 1.14 | 0.407 | 317.1 | 5.3 | 10.2 | 3.1 | 65.3 | 73.5 | 4.4 | 3.5 |
| SF12 | 121.6734 | 36.9048 | porphyritic granite(SFS) | 5 | 30.10 | 1.118 | 0.702 | 284 | 18.3 | 18.9 | 4.4 | 38 | 50.9 | 7.6 | 2.5 |
| SF13 | 121.7994 | 37.1271 | porphyritic granite(SFS) | 6 | 10.90 | 1.131 | 0.646 | 279 | 0.2 | 19.3 | 2.4 | 9.3 | 55.2 | 4.9 | 2 |
| SF14 | 121.7889 | 37.1080 | porphyritic granite(SFS) | 5 | 8.12 | 1.118 | 0.351 | 171.3 | 7.4 | 32.5 | 3.3 | 0.4 | 82.5 | 10.7 | 8.9 |
| QS01 | 121.2914 | 37.2937 | biotite monzogranite(QS) | 5 | 0.10 | 1.049 | -0.23 | 226.4 | 73.8 | 16.3 | 5.9 | 14 | 13.8 | 19.2 | 5.9 |
| QS02 | 121.2924 | 37.2692 | biotite monzogranite(QS) | 5 | 0.16 | 1.068 | 0.022 | 107.4 | 36.9 | 7.7 | 4 | 238 | 40.9 | 7.8 | 2.5 |
| QS03 | 121.2918 | 37.2363 | biotite monzogranite(QS) | 5 | 0.53 | 1.047 | -0.156 | 80.8 | 57.5 | 18.1 | 5 | 287.8 | 29.6 | 18 | 4.2 |
| QS04 | 121.3021 | 37.1710 | mylonitic monzogranite(QS) | 7 | 0.47 | 1.244 | 0.564 | 119.7 | 0.6 | 20.6 | 2.2 | 21.8 | 85.7 | 17.4 | 2.4 |
| QS05 | 121.3871 | 37.2144 | biotite monzogranite(QS) | 7 | 2.47 | 1.084 | -0.208 | 121.8 | 19.6 | 13.6 | 4.9 | 238.5 | 51.6 | 27.9 | 5.7 |
| QS06 | 121.3689 | 37.2024 | biotite monzogranite(QS) | 6 | 0.34 | 1.045 | 0.282 | 317.6 | 46.6 | 41.4 | 24.6 | 122.5 | 42.4 | 32.4 | 24.2 |
| QS07 | 121.3855 | 37.1773 | biotite monzogranite(QS) | 6 | 1.77 | 1.218 | 0.355 | 14.7 | 45.8 | 11.4 | 3.9 | 128.2 | 21.3 | 12.8 | 7.5 |
| QS08 | 121.3688 | 37.2547 | biotite monzogranite(QS) | 7 | 5.54 | 1.265 | 0.076 | 284.2 | 10.4 | 28.4 | 7.9 | 21.6 | 35.1 | 19.9 | 7.3 |
| QS09 | 121.3565 | 37.2373 | biotite monzogranite(QS) | 5 | 0.04 | 1.054 | 0.106 | 84.7 | 11.5 | 28.5 | 10.3 | 353.2 | 7.3 | 29.1 | 4.8 |
| QS10 | 121.3191 | 37.2186 | biotite monzogranite(QS) | 7 | 0.15 | 1.075 | -0.112 | 94.1 | 29.9 | 10.5 | 5 | 189.5 | 9.3 | 11.2 | 3 |
| QS11 | 121.3182 | 37.2494 | biotite monzogranite(QS) | 5 | 0.17 | 1.034 | -0.377 | 158 | 14.1 | 13.4 | 8.1 | 44.1 | 58.2 | 27.2 | 9.3 |
| QS12 | 121.3121 | 37.2378 | biotite monzogranite(QS) | 7 | 0.22 | 1.054 | 0.142 | 111.4 | 56.3 | 11.4 | 5.5 | 202 | 0.4 | 9.1 | 5 |
| QS13 | 121.3145 | 37.1840 | biotite monzogranite(QS) | 6 | 0.12 | 1.039 | 0.218 | 90.7 | 15.5 | 8.8 | 3.9 | 321.7 | 66.2 | 12.1 | 3.6 |
| QS14 | 121.4058 | 37.1547 | biotite monzogranite(QS) | 7 | 0.14 | 1.116 | -0.161 | 309.8 | 2.1 | 5.5 | 3.6 | 207.1 | 80.7 | 20.2 | 3.9 |
| QS15 | 121.4175 | 37.1259 | mylonitic monzogranite(QS) | 6 | 0.07 | 1.127 | 0.356 | 280.1 | 6.5 | 14.5 | 8.9 | 157.1 | 78.2 | 9.6 | 6.5 |
| QS16 | 121.4472 | 37.2443 | biotite monzogranite(QS) | 7 | 0.10 | 1.08 | 0.335 | 149.2 | 0.7 | 8.9 | 6 | 241.6 | 73.5 | 19.3 | 6.4 |
| QS17 | 121.4218 | 37.2377 | biotite monzogranite(QS) | 6 | 3.79 | 1.198 | 0.047 | 47.9 | 16.5 | 7.8 | 1.8 | 292.5 | 55.4 | 10.3 | 1.3 |
| QS18 | 121.4322 | 37.2106 | biotite monzogranite(QS) | 5 | 16.40 | 1.496 | 0.419 | 63.5 | 14.7 | 22.7 | 12.3 | 233.3 | 75.1 | 16.7 | 4.1 |
| QS19 | 121.4491 | 37.1395 | biotite monzogranite(QS) | 7 | 0.04 | 1.078 | 0.443 | 302.4 | 8.0 | 8.6 | 4.4 | 40.9 | 46.5 | 4.6 | 1.9 |
| QS20 | 121.4689 | 37.1672 | biotite monzogranite(QS) | 7 | 0.24 | 1.083 | 0.537 | 104.7 | 76.4 | 9.9 | 5.3 | 352 | 5.3 | 9.3 | 2.3 |
| QS21 | 121.4859 | 37.2275 | biotite monzogranite(QS) | 9 | 3.34 | 1.336 | -0.165 | 6.5 | 31.4 | 26.9 | 7.2 | 218.4 | 54.2 | 15.5 | 7.2 |
| QS22 | 121.5156 | 37.2553 | biotite monzogranite(QS) | 5 | 0.04 | 1.056 | -0.244 | 21.6 | 25.9 | 13.1 | 5.1 | 179.7 | 62.4 | 57.6 | 6.6 |
| QS23 | 121.4903 | 37.2811 | biotite monzogranite(QS) | 6 | 0.18 | 1.028 | 0.174 | 139 | 5.9 | 18.1 | 5 | 246.4 | 70.9 | 17.4 | 6.8 |
| QS24 | 121.5648 | 37.3416 | biotite monzogranite(QS) | 7 | 0.38 | 1.138 | 0.213 | 35.2 | 45.7 | 14.2 | 3.8 | 218.4 | 44.2 | 4.1 | 3.3 |
| QS25 | 121.5810 | 37.3153 | biotite monzogranite(QS) | 6 | 2.20 | 1.132 | -0.424 | 32.3 | 9.8 | 9 | 4 | 137.3 | 56.2 | 39 | 4.1 |
| QS26 | 121.5432 | 37.3034 | biotite monzogranite(QS) | 7 | 6.98 | 1.094 | -0.311 | 5.5 | 31.5 | 9.1 | 6.3 | 127.7 | 41.1 | 24.4 | 3 |
| QS27 | 121.2807 | 37.1856 | mylonitic monzogranite(QS) | 5 | 3.59 | 1.378 | 0.408 | 117 | 6.5 | 22.3 | 5.1 | 250.1 | 80.5 | 11.7 | 2.6 |
| QS28 | 121.2585 | 37.1598 | mylonitic monzogranite(QS) | 5 | 1.15 | 1.247 | 0.428 | 96.8 | 12.0 | 6.5 | 3.4 | 293.3 | 77.5 | 8.6 | 3.1 |
| QS29 | 121.2507 | 37.1317 | mylonitic monzogranite(QS) | 6 | 2.41 | 1.354 | 0.427 | 297.9 | 5.4 | 6.3 | 3.5 | 57.8 | 79.1 | 3.7 | 2.7 |
| QS30 | 121.2641 | 37.1053 | mylonitic monzogranite(QS) | 5 | 0.16 | 1.111 | 0.261 | 291.3 | 4.5 | 13.1 | 5.2 | 53.7 | 81.6 | 5.5 | 3.2 |
| QS31 | 121.2786 | 37.0828 | mylonitic monzogranite(QS) | 5 | 2.37 | 1.142 | 0.017 | 244.1 | 6.9 | 16.3 | 5.7 | 102.3 | 81.3 | 24 | 4.9 |
| QS32 | 121.2961 | 37.1222 | mylonitic monzogranite(QS) | 5 | 0.06 | 1.153 | 0.257 | 303.7 | 0.6 | 12.3 | 2.4 | 212.1 | 69.7 | 6.5 | 2.8 |
| QS33 | 121.3881 | 37.1383 | mylonitic monzogranite(QS) | 5 | 0.14 | 1.101 | 0.149 | 293.5 | 8.8 | 7.2 | 3.9 | 49 | 70.3 | 7.5 | 3.9 |
| QS34 | 121.3301 | 37.1410 | mylonitic monzogranite(QS) | 6 | 10.00 | 1.382 | 0.169 | 282.2 | 1.3 | 13.9 | 4.4 | 14.3 | 58.4 | 5.4 | 5.2 |
| YG1 | 121.3831 | 37.3124 | porphyritic granite(YGZ) | 5 | 18.10 | 1.105 | 0.612 | 3.4 | 17.4 | 21.1 | 4.8 | 245.3 | 56.4 | 6.1 | 4.8 |
| YG2 | 121.3754 | 37.2624 | porphyritic granite(YGZ) | 5 | 15.20 | 1.086 | 0.422 | 89.1 | 2.6 | 11.8 | 6.1 | 353.7 | 64.2 | 10.5 | 5.2 |
| YG3 | 121.3943 | 37.2606 | porphyritic granite(YGZ) | 6 | 0.48 | 1.03 | 0.075 | 185.3 | 33.2 | 10.6 | 3 | 59.6 | 41.8 | 15.6 | 3.1 |
| YG4 | 121.3882 | 37.2979 | porphyritic granite(YGZ) | 7 | 13.20 | 1.097 | 0.576 | 23.6 | 7.3 | 27.3 | 2.8 | 274.5 | 68.5 | 5 | 3.1 |
| YG5 | 121.3320 | 37.2992 | porphyritic granite(YGZ) | 6 | 19.50 | 1.113 | 0.567 | 200.2 | 4.6 | 21 | 2 | 344.6 | 84.3 | 4.4 | 2.1 |
| YG6 | 121.3169 | 37.3184 | porphyritic granite(YGZ) | 6 | 13.00 | 1.091 | 0.546 | 123.2 | 11.7 | 9.5 | 2.7 | 352.1 | 72.6 | 4.3 | 2.7 |
| YG7 | 121.3464 | 37.3208 | porphyritic granite(YGZ) | 6 | 15.70 | 1.08 | 0.518 | 117.7 | 17.8 | 34.6 | 6.9 | 302.8 | 72.2 | 9.6 | 6.2 |
| YG8 | 121.3425 | 37.2851 | porphyritic granite(YGZ) | 6 | 15.40 | 1.085 | 0.584 | 234.2 | 3.3 | 13.9 | 1.8 | 345.5 | 80.9 | 6.5 | 1.2 |

| | | | | | | | | | | | | | | | |
|---|---|---|---|---|---|---|---|---|---|---|---|---|---|---|---|
| YG9 | 121.3341 | 37.2711 | porphyritic granite(YGZ) | 6 | 24.40 | 1.205 | -0.197 | 302.8 | 18.9 | 5.8 | 3.4 | 39.5 | 18.8 | 5.4 | 3.2 |
| YG10 | 121.4306 | 37.2880 | porphyritic granite(YGZ) | 5 | 15.60 | 1.118 | 0.438 | 357.5 | 55.3 | 19.7 | 8.2 | 240.5 | 17.5 | 13 | 3 |
| YG11 | 121.4483 | 37.2759 | porphyritic granite(YGZ) | 5 | 13.70 | 1.16 | 0.042 | 270.7 | 40.7 | 16.5 | 2.4 | 25.6 | 26.1 | 7.5 | 4.5 |
| YG12 | 121.4194 | 37.3223 | porphyritic granite(YGZ) | 6 | 31.90 | 1.255 | 0.46 | 340 | 39.1 | 4.9 | 4.4 | 237.6 | 14.8 | 6.8 | 3.2 |

**Table 1.** The results of AMS measurements for Queshan, Kunyushan, Yuangezhuang and Sanfoshan plutons. Lat: latitude, Long: longitude, N: the number of cylinders measured in each site, Km: mean magnetic susceptibility, $P_J$: anisotropy degree, T: shape parameter, $K_1$ and $K_3$: magnetic lineation and pole of magnetic foliation, respectively, Inc: inclination, Dec: declination, $\alpha_{95max}$ and $\alpha_{95min}$: Jelinek's statistic confidence at 95% level (Jelinek, 1981) in degrees, KYS: Kunyushan pluton, QS: Queshan pluton, SFS: Sanfoshan pluton, YGZ: Yuangezhuang pluton.